UNIVERSITY OF CALIFORNIA
SANTA CRUZ

SEARCH FOR EXOTIC PHYSICS IN THE 2+ TOP-TAG, 2+ B-TAG CHANNELS OF THE FOUR TOP QUARK FINAL STATE IN 20.3 $\mathbf{fb}^{-1}$ OF PP COLLISIONS AT $\sqrt{s} = 8$ TeV WITH THE ATLAS DETECTOR

A dissertation submitted in partial satisfaction of the
requirements for the degree of

DOCTOR OF PHILOSOPHY

in

PHYSICS

by

Peter Michael Manning Jr.

March 2014

The Dissertation of Peter Michael Manning Jr.
is approved:

Professor Abraham Seiden, Chair

Professor Jason Nielsen

Professor Stefano Profumo

Dean Tyrus Miller
Vice Provost and Dean of Graduate Studies

Table of Contents

List of Figures

List of Tables

Abstract

Search for exotic physics in the 2+ top-tag, 2+ b-tag channels of the four top quark final state in 20.3 $\text{fb}^{-1}$of pp collisions at $\sqrt{s} = 8$ TeV with the ATLAS detector

by

Peter Michael Manning Jr.

We present a search for new exotic physics in pp collisions at $\sqrt{s} = 8$ TeV recorded by the ATLAS detector at the Large Hadron Collider (LHC) at CERN. Our search is focusing on the production of four top-quark final states. Specifically, we are looking for events with two or more top-quarks produced with very high transverse momentum, tagged using jet substructure variables. Events with at least two top-tagged jets are also required to have at least two b-tagged jets, with a further requirement that one of the b-tagged jets lie outside the conical radius of the top-tagged jets. Finally, we look in events that have a large amount of total transverse momentum (H_{T}) that is optimized for several potential new signal models (low-H_{T} and high-H_{T}). In a data sample of 20.3 fb^{-1} we measured an expected background of $13.04 \pm 3.150^{+3.925}_{-4.751}$ events in the low-H_{T} channel and measured an expected background of $5.024 \pm 1.918^{+1.753}_{-2.971}$ events in the high-H_{T} channel. We expect to set a limit on the Kaluza-Klein mass scale $\text{m}_{\text{KK}} > 1.06$ TeV at the 95% CL assuming no excess of or deficit of events are seen in the data.

To my unwaveringly supportive wife, my loving family, my friends new and old and my mentors. Life is a journey and all of you have contributed to this dissertation and in some way large or small, shaped who I have become.

Acknowledgments

This research was supported by grants from the NSF, DOE as well as The University of California Santa Cruz and the Santa Cruz Institute for Particle Physics.

This dissertation is an expression of many of the things that I have been involved in throughout the many years of graduate school, however it isn't a complete record of everything I have learned. The knowledge and wisdom I have gained through this process could never make it to print, as it would be impossible to describe something that is intangible. I have to thank my very supportive, motivational, wise and caring advisor, Abe Seiden, for believing in me even when I didn't believe in my self. You always had such clear vision of the future, even if I did not. Thank you for being so patient and for making my experience here an enjoyable one. I would like to thank Jason Nielsen for always having such a positive attitude and being such an integral part of my success in completing this analysis. And, Stefano Profumo, thank you for taking me under your wing early on and encouraging my theoretical mind to grow. The three of you made my graduate experience as complete as one could possibly want.

I would like to thank my loving, patient and unbelievably supportive wife. The last few months would not have been bearable without you, the last few years would not have been enjoyable without you, and I would not have as much to look forward to now that it is all done, without you by my side. I know it was very hard at times and it felt like it was never going to get better. Thank you for sticking with me and believing in me throughout.

Thank you to all of my friends and family in Santa Cruz, namely Vickie Nam and Marc Chow, for always being there when we needed you. You are truly amazing friends. Thanks to the Sones family for really becoming our family away from home. Thank you as well for helping me so much during my defense - you made it feel seamless and so much less difficult.

To my mom, dad, sister and brother and extended family, thank you for your support, understanding of my absence from your lives during the past many years and encouragement to persevere.

And finally, I need to thank Kayla and Lester, our wonderful dogs, for being the fluffiest supporters of all.

Part I

The Standard Model

Chapter 1

Introduction

The twentieth century was undeniably one of the most scientifically significant centuries to date. From the formulation of general relativity describing gravity as the result of curvature in space-time, to the discovery of the quantum mechanical behavior of elementary particles, the discovery of the top quark and in the past year, discovery of a new boson consistent with the Higgs, it may seem that our picture of the universe has never been so clear. On the contrary, all of the inventions and discoveries of the twentieth century have raised numerous additional questions about our physical universe. What is dark matter? Why is the top quark so massive compared to the other quarks? Are there only three spatial dimensions? With the completion of the Large Hadron Collider (LHC) and its successful proton-proton collision program coupled with the general purpose ATLAS (A Toroidal LHC Apparatus) particle detector, the answers to these questions and many others could become the most significant discoveries of this century.

1.1 Outline

This thesis is broken into four main parts. The first part will describe the relevant areas of the Standard Model and their limitations. These limitations motivate the search for the four top quark final state, the subject of this thesis, as an indicator of new physics. Several models with this signature will be described with significant emphasis placed on the Two Universal Extra Dimensions model and its implementation using FeynRules. The second part of this thesis will describe the LHC and the ATLAS detector, relevant sub-detectors, as well as the use of the trigger system. The third part will describe the Monte Carlo samples for both the four top quark signal as well as expected backgrounds. The final part is the Analysis section, which is comprised of a description of the event selection, background estimation, systematic uncertainties and finally results and discussion.

Chapter 2

The Standard Model

In order to understand the motivation for new physics in the top quark sector, we must first discuss some basic concepts surrounding the Standard Model. While entire books have been written on The Standard Model and its many intricacies, this chapter will only focus on two areas of interest. Namely, the physics of fermions and bosons at high energies.

2.1 Fermions

In the most general definition, fermions are elementary particles with half-integer spin. Particles of this type follow Fermi-Dirac statistics where no more than one particle can occupy a single energy state. Fermions compose twelve of the sixteen (now seventeen when we include the recently discovered Higgs like boson) known Standard Model elementary particles if we exclude counting the anti-particle partners.

There are two distinct classes of fermions; leptons and quarks. Leptons are

governed only by the electroweak force[1] . This group of fermions can be subdivided even further into charged leptons and the corresponding neutral leptons, neutrinos. The charged leptons contain integer charge and may participate in either left or right handed electroweak interactions. On the other hand, the neutrinos contain zero charge and based on experimental evidence that right-handed neutrinos do not exist, we can conclude that neutrinos are governed only by weak interactions because only left-handed leptons participate in weak interactions.

The other class of fermions, quarks, are fractionally charged. The up-type quarks contain $+2/3$ unit of charge, while the down types have $-1/3$ unit charge (anti-up has $-2/3$ and anti-down has $+1/3$). Quarks are distinct from leptons in that they not only participate in electroweak interactions (there are both left-handed and right-handed quarks of each type), but also in strong interactions.

There are three generations of both quarks and leptons. Visible matter as we know it is composed of elementary particles of the first generation. Namely, electrons, up-quarks and down-quarks. The quarks combine in sets of three to form baryons such as protons and neutrons (the proton is made up of two up quarks and a down quark while the neutron is made up of two down quarks and one up quark). The anti-particles of these "visible" matter constituents do not make up what we tend to call ordinary matter, however they are produced in abundance at particle accelerator experiments. Baryons are a subset of a larger category of particles called hadrons that also includes mesons, which are described below. The electron is generally bound to systems of

[1]Technically leptons are also influenced by the gravitational force, but this effect is so small on the single particle scale that we can neglect it.

baryons by the electromagnetic force making up what we call atoms. Since neutrinos are chargeless, effectively massless [26] and governed only by the weak force, they do not form any bound states with stable matter, which is why the electron-neutrino was not in the aforementioned list.

Particles of the second and third generations are produced either in high energy particle collisions, such as those from cosmic rays entering our atmosphere, or from particle collider experiments, but none exist as stable forms of matter. The second and third generation leptons are the muon and tau leptons, respectively, and their corresponding neutrinos. The second and third generation up (down) type quarks are the charm (strange) and top (bottom) quarks, respectively. Once produced, these rare fermions eventually decay back down to fermions of the first generation. Neutrinos are the exception to this rule, as they can oscillate between generations (flavors) and have not been observed to decay.

2.2 Bosons

Characterized primarily by their integer spin, $(0, 1, 2, ...)$, bosons follow Bose-Einstein statistics which allows multiple particles to occupy the same quantum state. This is in contrast to Fermi-Dirac statistics where only a single particle can occupy a quantum state. These particles are either elementary gauge bosons, or composite mesons. Both of these types of bosons are important for vastly different reasons.

In the language of quantum field theory, gauge bosons are quanta of the gauge

fields of a quantized gauge theory. Gauge refers to a choice of local transformations that form a Lie group under which the Lagrangian of the theory is invariant. If a force is felt between two particles, this is due to the exchange of a gauge boson from one particle to the other. The four known forces are gravitational, mediated possibly by the yet to be discovered graviton, weak, mediated by the charged $W^{\pm}$ and neutral Z bosons, electrodynamic, mediated by the photon and finally strong, mediated by the gluon. The associated guage groups for the electrodynamic, weak, and strong interactions are U(1), SU(2) and SU(3), respectively. Recently, a particle consistent with the Higgs boson was discovered at both the CMS and ATLAS experiments at CERN with a mass of close to 126 GeV [9]. While the Higgs is not a force carrier, the Standard Model predicts that it is responsible for electroweak symmetry breaking that results in the W, Z as well as fermions having mass.

Mesons represent any non-gauge boson that has integer spin and is composed of a quark and anti-quark. Examples include flavorless mesons such as neutral pions (π-mesons) that are composed of up and down quarks, flavored mesons such as charged and neutral kaons (K-mesons) that are composed of up- and down-type quarks of different flavors, as well as many other flavored and flavorless combinations. I noted earlier that gauge bosons and mesons are important for different reasons. Mesons are not messengers of any force, but they are the most abundantly produced particles in high energy particle collisions due to the hadronization of quarks, as described in the next section. These composite particles are also unstable and always decay eventually to either leptons or photons.

A graphical summary of the entire family of Standard Model particles is shown in Fig. 2.1.

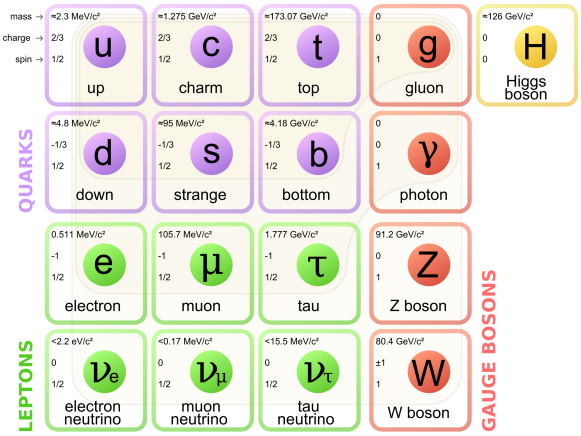

Figure 2.1: Graphic showing the three generations of fermions and quarks, the three gauge bosons, as well as the recently discovered Higgs boson as well as particle masses, spin and charge.

2.3 Color, Confinement and the Production of Jets

Quarks and gluons are unlike leptons, photons, as well as the electroweak gauge bosons in a very significant way. While the latter, more vanilla particles have been observed propagating through space freely[2], quarks and gluons have not. This section aims to explain this phenomena and its importance to this thesis.

The non-observation of free quarks (or any other particle with fractional charge), as well as restrictions placed on the symmetry of wave functions of observed baryons, led to the proposal that quarks carry an additional quantum number called color. The field of study describing these colored particles is referred to as quantum chromodynamics

[2]Either through direct observation of the observation of decay products

or QCD. Quarks then, carrying one of three colors, would transform under the SU(3) symmetry. Gluons also carry color, a property that allows them to be self-interacting. Analogously and as an aside, since the photon does not carry charge (the quanta of the electromagnetic interaction), it is not self-interacting. Due to the requirement that all wave functions resulting in physical states be singlets under SU(3) transformations, only two possible color-singlet states are possible. Namely, those of mesons and baryons. While this result is mathematically very convenient, it does little to explain the physical mechanism forcing all physically observable hadrons to be color-singlet states.

The *how* and *why* behind this result is due to two non-mutually exclusive concepts: asymptotic freedom and confinement. The former is a property of all non-Abelian gauge theories, such as guage theories transforming under the SU(3) symmetry, and therefore quarks are asymptotically free. But, what does this mean? Physically, this means that at very small distances partons can be thought of as nearly free particles. Let me explain why. One can parameterize the strong coupling $\alpha_S(Q^2)$ as,

$$\alpha_S(Q^2) = \frac{\alpha_S(\mu^2)}{1 + (\alpha_S(\mu^2)/12\pi)(11n_c - 2n_f)ln(Q^2/\mu^2)} \tag{2.1}$$

where Q^2 is the magnitude squared of the momentum transfer between patrons (i.e. quarks and gluons), n_c is the number of colors, n_f is the number of flavors, and μ is an arbitrary factorization scale, often chosen as a scale typical of the transition from long- and short distance (low- and high energy) physics [52] [57] (typically chosen as the mass of the Z-boson). As Q^2 becomes large, the coupling constant become asymptotically smaller, approaching zero. There are several ways of looking at this property, one of

which is described below.

First, consider color the "charge" of QCD. In quantum electrodynamics, as two opposite charges become closer, the stronger the interaction between the charges becomes due to the true charge being screened by the effects of vacuum polarization. The vacuum is an amazing medium. While it is *nothing* it has infinite energy to loan (as long as you give it back!), and acts as a dielectric medium. Therefore, the less *nothing* between particles, the less their charges are screened. Remember though, this only occurs at large Q^2. Now, consider the situation for quarks: when the distance between the quarks is very small. This results in $\alpha_S(Q^2)$ being small, and thus the effective color-charge is anti-screened. This largely has to do with the self-interacting nature of gluons (emission and absorption of virtual gluons between two partons). See [**?**, **?**] for more technical details about the dielectric effect of how the vacuum anti-screens the color charge. In the opposite regime with Q^2 small, α_S becomes very large. Due to this feature of the strong force, quarks are confined within hadrons, since it would require a very large amount of energy (increasing with distance between partons) to tear the quarks apart.

Both of these concepts are crucial to describing hadronic collisions. Asymptotic freedom is important because it allows us to treat colliding partons perturbatively in large Q^2 collisions. If this were not the case, we would be dealing with an N-body problem, which can become arbitrarily impossible to solve analytically or numerically. Confinement is important because it gives us a way to see the eventual fate of the partons in collisions as they create hadronic jets, which I will describe shortly. This

latter concept also explains why we only see color-singlet physical states; it leads to the hadronization, or conversion of partons into hadrons.

As partons move through the color field with high momenta, two things can happen. First, partons can be created out of the vacuum to form hadrons. Second, the partons can radiate gluons, leading to further hadronization. Consider as an example the process pp to $q\overline{q}$ via gluon fusion at a symmetrical pp collider, such as the Large Hadron Collider. As each quark flies in opposite directions, they will begin to hadronize, emmitting gluons, forming more hadrons, until there is a final state of hadrons that eventually decay to likely more hadrons as well as leptons. The physical result of this hadronization is a spray, or jet, of hadrons that can be detected using, for example, a calorimeter. Therefore, if we talk about seeing a b-quark or top-quark, as described in the next section, we are really talking about seeing the jet formed from the hadronization of that quark as it traverses the detector.

2.4 Top Quark Production and Decay

While the existence of the top quark was predicted many decades earlier [64], it was not discovered until 1995 at the Tevetron $p\overline{p}$ collider at Fermilab [15] [13]. The top quark is the heaviest known particle in the Standard Model with the most recent experimental value for its mass being $172.9 \pm 0.6 \pm 0.9$ GeV [78]. The reason the top quark is so much more massive than any other fermion is currently unknown[3] and is

[3]The next heaviest is the bottom quark, weighing in at 4.5 GeV [78], 40 times less than the top-quark mass

one of the motivating factors in searching for new physics in the top quark sector.

2.4.1 $t\bar{t}$ Production

In the Standard Model, top quarks can be produced in high energy particle collisions singly with other quarks via the weak interaction, in pairs from the strong interaction, triplets with a b-quark or quadruplets[4]. Experiments have observed single top production [58] [68] [60] and pair produced top-quarks but no evidence for three-top or four-top quark production has been found.

The predominant production mechanism for top-quark pairs ($t\bar{t}$) at the LHC is through gluon-gluon fusion, as shown in Figs. 2.2(a) and 2.2(b), but $t\bar{t}$ may also be produced through $q\overline{q}$ annihilation, as shown in Fig. 2.3.

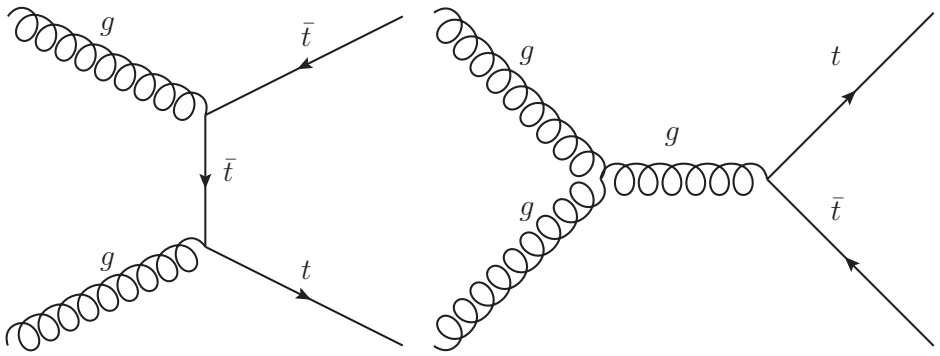

Figure 2.2: Top pair production via 2.2(a) the exchange of a top quark and 2.2(b) gluon fusion.

Once produced, the positively charged top-quarks decay almost immediately

[4]Theoretically it should be possible to produce any number of top quarks, but these are the most relevant to this thesis

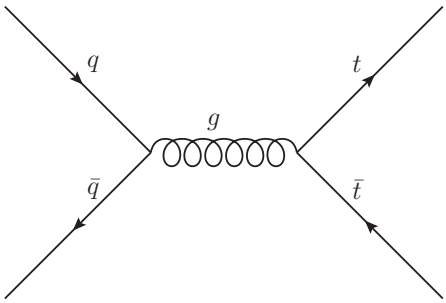

Figure 2.3: Top pair production from $q\overline{q}$ annihilation.

(within $3x10^{-25}$ seconds [31]) to a positively charged W-boson (W^+) and a b-quark close to 100% of the time. The anti-tops analogously decay to a W^- and anti-b ($\bar{b}$). While the measured width of the W-boson is $2.028 \pm 0.072GeV$ [30], this results in a very small lifetime close to that of the top-quark around $3x10^{-25}$ seconds, meaning the W also decays almost immediately. There are two types of observed decay modes of the W. The first is leptonic, where the W decays to any of the known charged leptons with nearly equal probability, and a neutrino with the same flavor as the lepton. The second decay mode is hadronic, where the W decays to a light quark (u, d, c, s, b) and another, different anti-quark. The top-quark decay as well as the two W-decay processes are shown in Figs. 2.4(a) and 2.4(b). Therefore in $t\bar{t}$ events, there are three categories of final states; fully hadronic, where both Ws decay hadronically; semi-leptonic, where one W decays leptonically and the other hadronically; and fully-leptonic, where both the W^+ from the t and W^- from the $\bar{t}$ decay leptonically. The branching fractions for the various decays of the W can be found in [78].

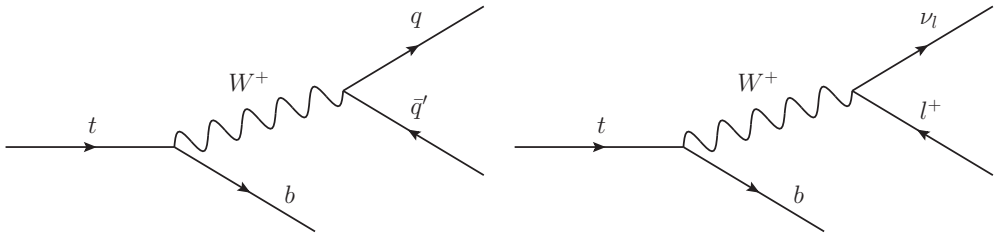

(a) (b)

Figure 2.4: Top-quark and subsequent W-decay in the 2.4(a) hadronic channel and 2.4(b) leptonic channel.

2.4.2 Four top quark production in the Standard Model

As mentioned earlier, there are Standard Model processes that can produce a four top quark final state, the topic of this thesis. While the cross section of this process is small ($0.73 \pm 0.45 fb$ at $\sqrt{s} = 7$ TeV and $1.3 \pm 0.80 fb$ at $\sqrt{s} = 8$ TeV [29]) , it will be important to understand the various channels of this final state. There are effectively five decay channels in the four top quark final state. Those being the completely hadronic, single lepton, two, three and four lepton, where these describe the decay channels of the Ws from each t-quark. The branching fractions into each of these channels is shown in table 2.1. The predicted number of standard model events for $5 fb^{-1}$ at $\sqrt{s} = 7$ TeV and $20 fb^{-1}$ at $\sqrt{s} = 8$ TeV are also shown in table 2.1.

Channel	0 Lepton	1 Lepton	2 Lepton	3 Lepton	4 Lepton	All
Br.Fraction (%)	20.87	40.04	28.79	9.196	1.102	100
Events at $\sqrt{s} = 7$ TeV	0.7618	1.462	1.051	0.3357	0.004022	3.650
Events at $\sqrt{s} = 8$ TeV	5.426	10.41	7.485	2.391	0.2865	26

Table 2.1: Branching fractions and theoretical event yields for the Standard Model four top final state at $\sqrt{s} = 7$ and $\sqrt{s} = 8$ TeV

2.5 Limitations of the Standard Model

While the Standard Model has been very successful, it is not without limitations in its power to describe what we have observed in nature. We describe several of these below.

At the cosmological scale, measurements of the motion of galaxies and the expansion of the universe suggests the existence of a very large abundance of matter that we cannot see (appropriately called dark matter). Being that dark matter has not been observed and does not seem to interact in a known way with ordinary matter, it does not fit into the current model. There are several theoretical physics models that extend the standard model in ways that predict the existence of dark matter in various forms. See [28] and [59] for an excellent review of dark matter theory and phenomenology.

On a potentially more philosophical level, the Standard Model also does not describe why there are exactly three generations of fermions. Additionally, the Standard Model does not take into account neutrino oscillations and their resulting non-zero masses.

More surprisingly, the Standard Model does not have any predictions for why there is such a huge difference in the strength of fundamental forces (namely the gravitational and weak forces), even at very large particle energies. This is the so-called hierarchy problem. While the gravitational force may seem large, wham considering the gravitational force between two elementary particles, the weak force is 10^{32} times

stronger than gravity. Additionally, the Standard Model does not account for any gravitational interactions (there is no standard quantum theory of gravity that has been proven correct).

Models involving supersymmetry as well as those containing extra dimensions account for this large discrepancy and motivate the search for new physics, the topic of this dissertation. We describe in more detail some of the models that we may be sensitive to at the ATLAS detector.

Part II

Beyond the Standard Model

Chapter 3

Two Universal Extra Dimensions on the Chiral Square

3.1 Introduction

In the Two Universal Extra Dimensions (2UED) model, all of the Standard Model fields are permitted to propagate in the six dimensional space-time. This model is similar to its predecessor, the Minimal Universal Extra Dimensions (MUED) or simply UED model in that the extra dimensions are flat and compactified on some manifold [22]. The key difference being that there are two extra dimensions in 2UED, while just one in MUED. There are several schema for compactifying the two extra dimensions [51] [76], but in the case of one of the models we will look at, the two extra dimensions are compactified on a chiral square with sides of length πR [49] [33]. The adjacent sides of the square are "identified," which requires the field content on the identified points to

be equivalent. In the next chapter we will look at an alternative 2UED model.

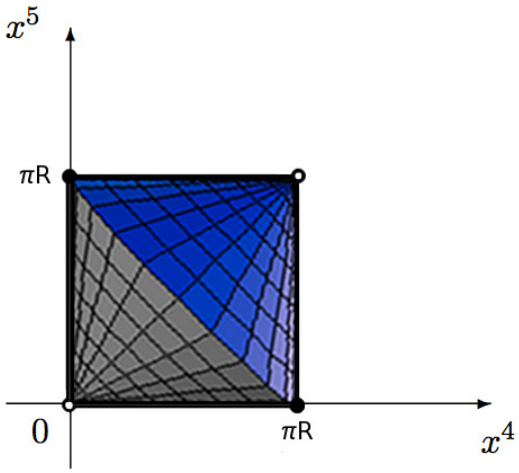

Figure 3.1: Representation of the chiral square. Identifying the sides is equivalent to requiring that $\mathcal{L}(x^\mu, y, 0) = \mathcal{L}(x^\mu, 0, y)$ and $\mathcal{L}(x^\mu, y, L) = \mathcal{L}(x^\mu, L, y)$, where $\mathcal{L}$ is the Lagrangian.

The chiral square has the topology of a sphere with two conical singularities at $(0, 0)$ and $(\pi R, \pi R)$ and the third at the identified points $(0, \pi R) \sim (\pi R, 0)$ as shown in 3.1. This scheme allows for the existence of chiral fermions [33], as there are in the Standard Model, as well as phenomenologically interesting features including the existence of a heavy, weakly interacting, stable particle (dark matter candidate) [37] [46], allowing only integer multiples of 3 fermion generations [50], and the production of a completely new set of heavy scalar particles [54].

The particle spectra of 2UED includes all of the Standard Model particles, their Kaluza-Klein excitations in either one or both of the compactified extra dimensions, as well as a set of real scalar fields in the adjoint representation of the 6D gauge fields. Upon compactification we recover the four dimensional gauge fields, but are left with

two extra components. One of these components, the aforementioned spinless adjoint to the gauge field, is invariant under 6D gauge transformations. The other, orthogonal excitation, shifts under such a transformation and corresponds to the Nambu-Goldstone boson eaten by the massive vector gauge field level by level. The 6D fermions have four components corresponding to the + or − 6D chiralities and the familiar L and R 4D chiralities. In order to insure global 6D anomaly cancellation and fermion mass generation, the chiralities of the weak-doublet quarks (leptons) are forced to be opposite those of the weak-singlet quarks (leptons) [50]. That is, for each generation of quarks there are the following fields: $\mathcal{Q}_+ = (\mathcal{U}_+, \mathcal{D}_+), \mathcal{U}_-, \mathcal{D}_-$, as well as the analogous fields for the leptons, including a − chirality neutrino field. Each of these 6D chiralities is composed of a combination of L and R handed components.

3.1.1 Kaluza-Klein Parity

Particles produced in this model must conserve Kaluza-Klein parity (P_{KK})in their decays. That is, a $(1,0)$ particle must decay to another $(1,0)$ particle and a standard model particle. Analogously, standard model particles can only pair produce KK particles due to this property. P_{KK} is a consequence of the imposed folding boundary conditions illustrated in Fig.3.1. Specifically, interactions in this theory must be invariant under Z_2 transformations of the form,

$$\Omega^{(j,k)}(x^\mu) \mapsto (-1)^{j+k}\Omega^{(j,k)}(x^\mu). \tag{3.1}$$

A consequence of this parity is the inherent stability of the lightest $(0,1)$ field, making it a viable dark matter candidate, as discussed in [86]. Since we don't usually think about interactions with just one particle unless describing single particle decay, consider a 2-body initial state and the analogous transformation,

$$\begin{aligned}\Omega_1^{(j,k)}(x^\mu)\Omega_2^{(i,l)}(x^\nu) &\mapsto (-1)^{j+k}(-1)^{i+l}\Omega_1^{(j,k)}(x^\mu)\Omega_2^{(i,l)}(x^\nu) \\ &\mapsto (-1)^{j+k+i+l}\Omega_1^{(j,k)}(x^\mu)\Omega_2^{(i,l)}(x^\nu). \end{aligned} \tag{3.2}$$

It should be clear that the only way for this state to be invariant under the Z_2 transformation is for $j+k+i+l$ to be even. Therefore, an initial state (or final state) with one $(0,0)$ and one $(0,1)$ field violates P_{KK}, while a state with a pair of $(0,1)$ fields does not. While P_{KK} must be conserved in this model, there is another related quantity, KK-number (N_{KK}), that does not necessarily need to be conserved. It is useful to think of incoming particles as containing negative N_{KK} and outgoing particles as carrying positive N_{KK}. For example, consider the following interaction,

$$q^{(0,0)}\overline{q}^{(0,0)} \to G_{H_1}^{(1,1)}G_{H_2}^{(1,1)} \tag{3.3}$$

where the $q^{(0,0)}$ is a standard model quark ($\overline{q}^{(0,0)}$ the anti-quark) and the resulting final state particles are the scalar $j=1, k=1$ gluon excitations. In the initial state, the N_{KK} is 0, while if we consider the $G_{H_1}^{(1,1)}$ as having N_{KK}, $n_{j_1}=1, n_{k_1}=1$ and $G_{H_2}^{(1,1)}$ as having N_{KK}, $n_{j_2}=-1, n_{k_2}=-1$, the final state N_{KK} is also $n_{j_1}+n_{k_1}+n_{j_2}+n_{k_2}=0$. N_{KK} is conserved during this process. All of the tree-level interactions conserve not only P_{KK}, but also N_{KK}. There is an exception to this rule. If the interaction is localized on either of the conical singularities, N_{KK} may be violated, while still preserving P_{KK}.

For example, the process $g^{(0,0)}g^{(0,0)} \rightarrow G_{\mu}^{1,1}$ conserves P_{KK} even, (two $(0,0)$ particles to one $(1,1)$ particle), but does not preserve N_{KK}. These N_{KK} violating Lagrangian terms are what allows for the decay of $G_{\mu}^{1,1}$ and $G_{H}^{1,1}$ directly to top quark pairs.

3.2 Four Top Quark Final State

There are six distinct production mechanism that result in a four top-quark final state. Of those six, there are two processes that we can call resonant four top production. Those being,

$$pp \rightarrow G_{H}^{11}G_{H}^{11} \tag{3.4}$$

$$pp \rightarrow G_{\mu}^{11}G_{\mu}^{11}. \tag{3.5}$$

Each of theG_{H}^{11} andG_{μ}^{11} can decay promptly to top quark pairs. The branching fraction of the G_{H}^{11} to $t\bar{t}$ is nearly 100%, as shown in the previous section, while the branching fraction ofG_{μ}^{11} directly to $t\bar{t}$ is less than 1%. Although the predominant decay mode of the G_{μ}^{11} is not $t\bar{t}$, nearly 75% (need to calculate the actual number, but it's close to this) of the G_{μ}^{11}s decay chains result in $t\bar{t}$ production. Such as the one shown in the figure below. The A_{H}^{11} and Z_{H}^{11} can also be pair produced, but the cross sections for pair producing these is $10^{-3}fb$ for $\sqrt{s} = 8$ TeV, so we don't consider those contributions.

The remaining four production mechanisms are,

$$pp \to G_H^{11} G_\mu^{11} \tag{3.6}$$

$$pp \to Q^{11} \bar{Q}^{11} \tag{3.7}$$

$$pp \to Q^{11} G_H^{11} \tag{3.8}$$

$$pp \to Q^{11} G_\mu^{11}, \tag{3.9}$$

where $Q^{11}$are the $(1,1)$ Kaluza-Klein quark excitations that include both the $+$ and $-$ chiralities and charges. The production cross sections for these processes for a range of $1/R$ at the center-of-mass energies $\sqrt{s} = 8$ TeV are shown in Table 3.1.

1/R [GeV]	500	600	700	800
$G_H^{11} G_H^{11}$	9.057	1.655	$3.429e^{-1}$	$7.461e^{-2}$
$G_\mu^{11} G_\mu^{11}$	28.36	3.902	$5.780e^{-1}$	$8.819e^{-2}$
$G_H^{11} G_\mu^{11}$	14.93	3.145	$7.021e^{-1}$	$1.582e^{-1}$
$Q^{11} \bar{Q}^{11}$	956.1	306.6	86.72	19.76
$Q^{11} G_H^{11}$	87.96	19.30	4.554	1.125
$Q^{11} G_\mu^{11}$	409.6	75.10	14.71	2.942
Total	1506.	409.7	107.6	24.14

Table 3.1: Production cross sections [fb]

3.3 Implementation in FeynRules

Significant work was done in implementing this model in the FeynRules Lagrangian to Monte Carlo software. This is described in the Appendix. Due to limitations

with respect to the current capabilities of the MadGraph matrix element generator, this model was not directly used in the analysis. However, since it was the original motivation for our search, we have still included it here.

Chapter 4

Two Universal Extra Dimensions on the Real Projective Plane

4.1 Introduction

As described in the previous chapter, In the Two Universal Extra Dimensions (2UED) model, all of the Standard Model fields are permitted to propagate in the six dimensional space-time. There are several schema for compactifying the two extra dimensions [51] [76] [49] [33], but in the case of this model, the two extra dimensions are compactified under the Real Projective Plane (RPP) geometry as discussed in detail in [36] [35]. Phenomenologically, this model as well as the 2UED compactified on a Chiral Square (CS) are interesting as they both contain a stable dark matter (DM) candidate, are compatible with current SM field content, as well as predict $3n$ number of fermion generations, where $n = 1, 2, 3....$ We will discuss some of the details of the

2UED-RPP model below and will use it as our benchmark signal process throughout the analysis.

Due to the particular nature of the RPP geometry, the radii of the extra dimensions are allowed to be different, as opposed to extra dimensions compactified on the CS, where the extra dimensions are forced to be the same due to symmetry considerations and restrictions of the chiral square orbifold. This results in the mass scale of the 2UED-RPP model being mostly degenerate at leading order for $R_5 \approx R_6$,

$$m_{l,k}^2 = \frac{l^2}{R_5^2} + \frac{k^2}{R_6^2}, \tag{4.1}$$

where l and k are the Kaluza-Klein (KK) excitation levels of the fifth and sixth dimensions of radius R_5 and R_6, respectively. Mechanisms that break this degeneracy include the Higgs VEV (resulting in non-zero standard model particle masses and a shift of m_0^2 to the above equation), loop corrections from bulk interactions, as well higher order operators that lie on singular points of the selected orbifold. The loop corrections give the largest shift in the masses of the Kaluza-Klein excitations.

For this analysis we are considering only the case where $R_5 \approx R_6$, resulting in a KK tree level mass of,

$$M_{KK} = \sqrt{\frac{l^2 + k^2}{R^2}}. \tag{4.2}$$

More specifically, we are interested in the $(1,1)$ tier that results in $M_{KK} = \sqrt{2}/R$. Limits have already been set excluding $M_{KK} < 900$ GeV [1], so our analysis is looking to either discover new physics in the $M_{KK} > 900$ GeV range or set an exclusion limit

greater than the current one. Given current cosmological constraints on the potential mass of a dark-matter candidate, the ideal range of this model lies between the current limit and around 1.2 TeV, close to where we hope to have sensitivity.

4.1.1 Four-top quark final state

In the $(1,1)$ tier of this model, there are several production mechanisms that result in our target final state. These processes are,

$$pp \rightarrow \quad G^{1,1}G^{1,1} \tag{4.3}$$

$$pp \rightarrow \quad q^{1,1}q^{1,1} \tag{4.4}$$

$$pp \rightarrow \quad q^{1,1}G^{1,1} \tag{4.5}$$

where $G^{1,1}$ is the level $(1,1)$ heavy gluon and $q^{1,1}$ is the level $(1,1)$ heavy quark (arising from the excitation of any of the 6 quark-flavors). Each of these processes eventually cascade decays down to 4 top-quarks as well as additional SM particles. An example process is shown in Fig. 4.1, reproduced from [1]. It should be noticed that there are quite a few additional SM particles also produced in the cascade decay (additional quarks and leptons). Production cross-sections for these processes at the LHC are given in **??**.

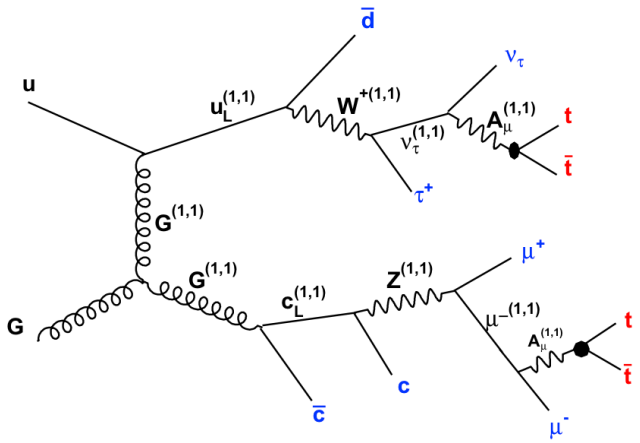

Figure 4.1: Example 2UED-RPP $pp \to q^{1,1}G^{1,1}$process that results in our target 4 top-quark final state.

Chapter 5

Scalar Gluons from Supersymmetry

Besides 2UED, several other beyond beyond Standard Model processes result in the four top final state. We describe one of those examples here. As described in [80], scalar gluons, or sgluons, occur in any supersymmetric model containing Dirac type gauginos. They are color octet scalars, carry SM type R charge [65] but no electroweak charge and are the scalar partners of the gluino. The fact that they carry type R charge allows them to interact directly with SM particles, resulting in direct single and pair production of this exotic particle. The sgluons decay predominantly into gluon pairs, $t\bar{t}$ pairs, as well as some combination of a top-quark and a light quark. Which one of these processes is dominant is dependent on the mass splitting between the squarks and gluinos. Expected production cross sections for several mass points in this model are shown on Table 10.1

Chapter 6

Contact Interactions

Another source of direct $t\bar{t}t\bar{t}$ production arises from 6-dimensional operators in composite top models, as described in [45]. In particular, a Lagrangian term that is suppressed by some scale Λ gives rise to their production,

$$\mathcal{L}_{t\bar{t}t\bar{t}} = \frac{1}{\Lambda}(\bar{t}_R\gamma^\mu t_R)(\bar{t}_R\gamma_\mu t_R), \tag{6.1}$$

where t_R are the right-handed Dirac spinors and γ_μ are the standard gamma matrices. Due to precision electro-weak measurements, it is predicted that any left-handed contributions would be highly suppressed.

Part III

Experimental Setup

Chapter 7

The Large Hadron Collider

[8] The Large Hadron Collider (LHC) is the world's largest particle accelerator. It is located across the French-Swiss border at CERN near Geneva, Switzerland in a tunnel that is on average 100 meters underground. At almost 27 kilometers in circumference, the machine is composed of a total of 1624 super-conducting dipole and quadrupole magnets, the former being shown in Fig. 7.1. The 1232 dipole magnets are responsible for keeping the particles on their circular path as well as accelerating them, while the 392 quadrupole magnets are used to focus the beams of particles. To become super-conducting, the magnets are cryogenically cooled down to a temperature less than 2 Kelvin using liquid helium. Once the magnets are cooled to their operating temperature, they sit at a nominal magnetic field of around 0.5 Tesla. Two beams of protons are injected into the LHC from the SPS in opposite directions, as shown in Fig. 7.2, each with an energy of 450 GeV. These beams are then accelerated to higher

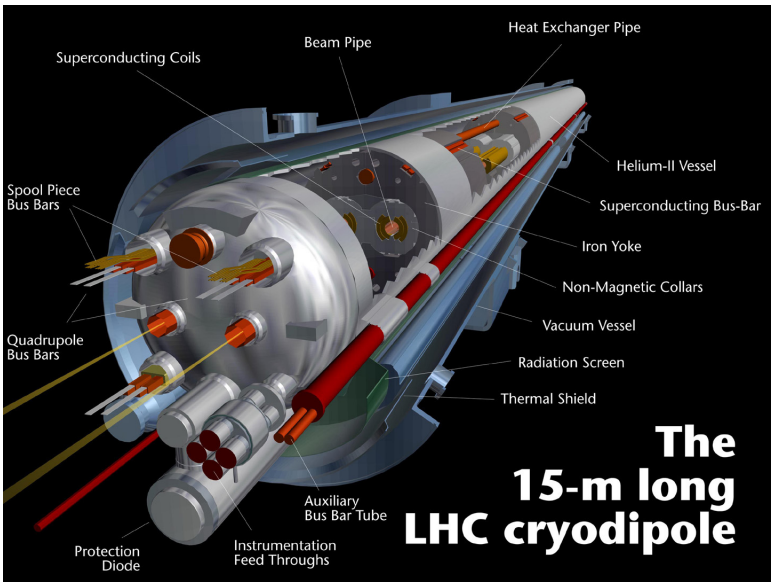

Figure 7.1: Cartoon rendition of one of the 15 meter LHC dipole magnets

and higher energies by increasing the magnetic field of the dipole magnets[1]. The LHC was originally designed to accelerate the protons in each beam to 7 TeV resulting in a center-of-mass energy of 14 TeV that required a magnetic field of 8.33 T, but due to the currently installed electrical connections between each dipole being unable to carry the required current for an 8.3 T field, the achieved energies were much less, yet still record breaking.

Along the LHC ring there are four particle detectors; ATLAS (A Toiroidal LHC ApparatuS), CMS (Compact Muon Solenoid), LHCb, and ALICE (A Large Ion Collider Experiment). The ATLAS detector will be described in detail in the next chapter.

[1]The momentum of the protons is directly proportional to the magnetic field, $p = qrB$, where r is the radius of the LHC, q is the charge and B is the magnitude of the magnetic field

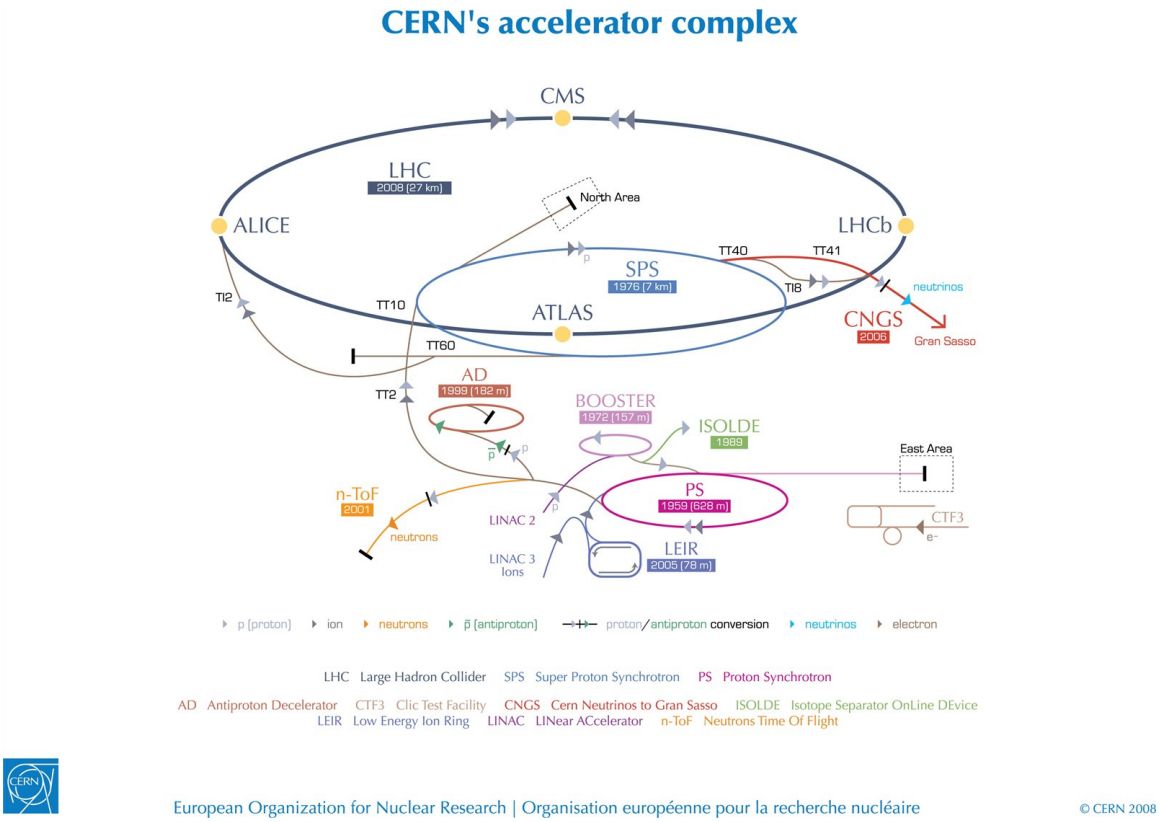

Figure 7.2: Graphic depicting all of the accelerators at CERN

7.1 Achieving high luminosity

While the center-of-mass energy of the collisions, $\sqrt{s}$, is of great importance, equally important is the instantaneous luminosity of the beam at the collision points. In general, the instantaneous luminosity is determined by the number of protons in a bunch per area per second. The larger the instantaneous luminosity the greater the probability of a proton-proton collision event. If we add up the instantaneous luminosity over time we are left with another very important measure, the total integrated luminosity. The LHC was designed to maximize both of these quantities in two key ways. Those being:

increase the number of protons / area via beam focusing and increase the number of bunches per fill. At full design capacity, the LHC should be able to accommodate 2808 bunches of around 10^{12} protons equally spaced $25ns$ in time around the accelerator ring. This configuration along with proper beam focusing and shaping would result in a design instantaneous luminosity of $\approx 10^{34} cm^{-2} s^{-1}$. A goal of the 2011 and 2012 running campaigns was to eventually achieve this milestone.

7.2 2011 Run

The 2011 run was the beginning of the true high luminosity physics campaign at the LHC. Each beam was accelerated to an energy of 3.5 TeV by increasing the magnetic field from 0.5 T to 4.15 T, resulting in a center-of-mass energy, $\sqrt{s}$, of 7 TeV. The first run resulting in collisions came from just three colliding bunches with a max instantaneous luminosity of $1.24 \cdot 10^{30} cm^{-2} s^{-1}$. The number of colliding bunches was gradually increased with a bunch spacing of $75ns$ resulting in a record breaking $\mathcal{L}_{inst}^{max} = 3.65 \cdot 10^{33} cm^{-2} s^{-1}$ near the end of the 2011 campaign. The $\mathcal{L}_{inst}^{max}$ for all of 2011 is shown in Fig. 7.3.

7.3 2012 Run

The 2012 run was originally going to be a direct continuation of 2011, but it was decided to not only increase $\sqrt{s}$ to 8 TeV (achieved by increasing the magnetic field to 4.47 T), but to also reduce the spacing between each bunch of protons to $50ns$. This

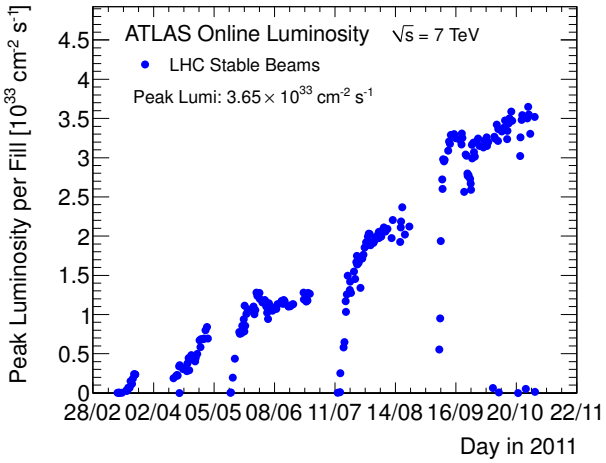

Figure 7.3: Maximum stable beam luminosity by day for 2011as measured by the ATLAS experiment

decision was made to maximize the instantaneous luminosity as well as the probability of producing rare collision products, such as a Higgs like particle or other exotic states. The overall $\mathcal{L}_{inst}^{max}$ for this year was achieved on August 24th by colliding 1368 bunches, resulting in $\mathcal{L}_{inst}^{max} = 7.73 \cdot 10^{33} cm^{-2} s^{-1}$. The $\mathcal{L}_{inst}^{max}$ for all of 2012 is shown in Fig. 7.4

7.4 Luminosity Summary

The delivered integrated luminosity as a function of month in each year for the 3 years of operation is shown in Fig. 7.5. The total integrated luminosity by ATLAS in the ready[2] state as well as the stable[3] state for each year as well as the uncertainty on the latter are given in table 7.1

[2]Luminosity delivered while the ATLAS ready flag was True, indicating that the warmstart has completed and ATLAS is ready to record data.

[3]Luminosity recorded in ATLAS after accounting for the L1 trigger live fraction.

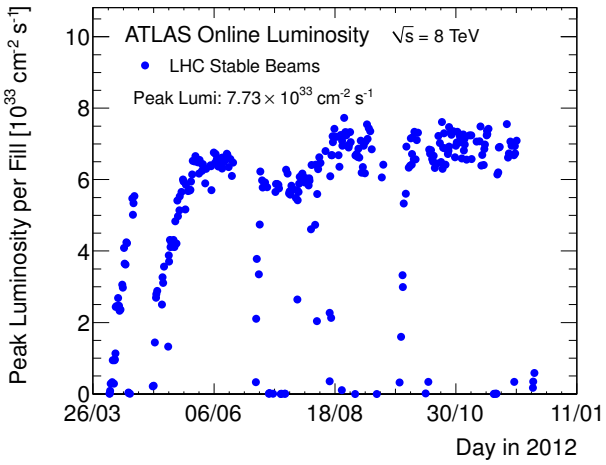

Figure 7.4: Maximum stable beam luminosity by day for 2012 as measured by the ATLAS experiment

Year	$\sqrt{s}$ [TeV]	ATLAS Ready	ATLAS Stable	Uncertainty
2010	7	46.72 pb^{-1}	45.03 pb^{-1}	3.4%
2011	7	5.467 fb^{-1}	5.252 fb^{-1}	1.8%
2012	8	22.826 fb^{-1}	21.742 fb^{-1}	3.6%

Table 7.1: Total integrated luminosity as measures at the ATLAS detector for the 7 and 8 TeV runs

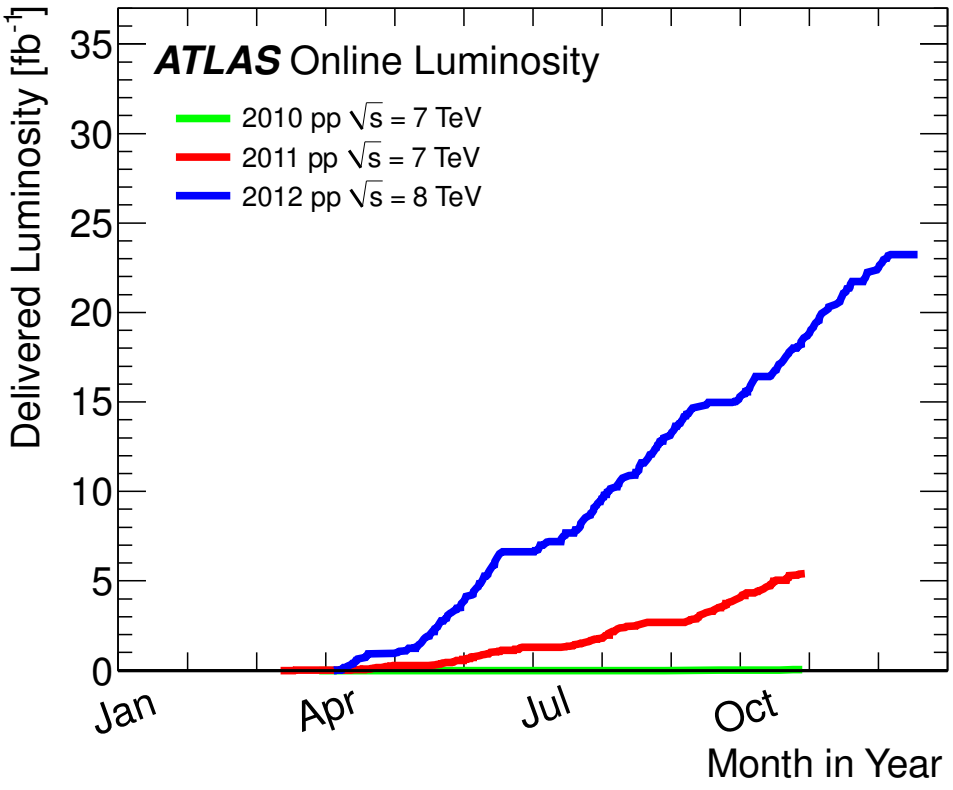

Figure 7.5: Total integrated luminosity of the LHC as measured by the ATLAS experiment in 2010 (green), 2011 (red) and 2012 (blue) as a function of month in that year.

Chapter 8

The ATLAS Detector

The ATLAS detector, shown in Fig. 8.1, is a general purpose particle detector 44 meters in length, 25 meters tall that is hermetic in azimuth[1]. It is composed of an inner tracking detector that is surrounded by a super-conducting solenoidal magnet that provides a 2 T magnetic field, a central and forward calorimeter, a set of toroid magnets that provide an 8 T field, and a muon spectrometer. Each of these components will be described in more detail in the following sections, with particular attention paid to systems that are more relevant to this thesis.

[1]When describing directions with respect to the collision point, ATLAS uses a right handed coordinate system with the z-axis coinciding with the beam pipe axis, the x-axis pointing to the center of the LHC, and the y-axis pointing upward. The azimuthal angle ϕ is in the x-y plane, while the polar angle θ is in the y-z plane. Another angular measure, the pseudo-rapidity η, is defined as $\eta = -ln[tan(\theta/2)]$. The pseudo-rapidity provides a more natural measure of the polar angle since ATLAS is cylindrical, as opposed to spherical.

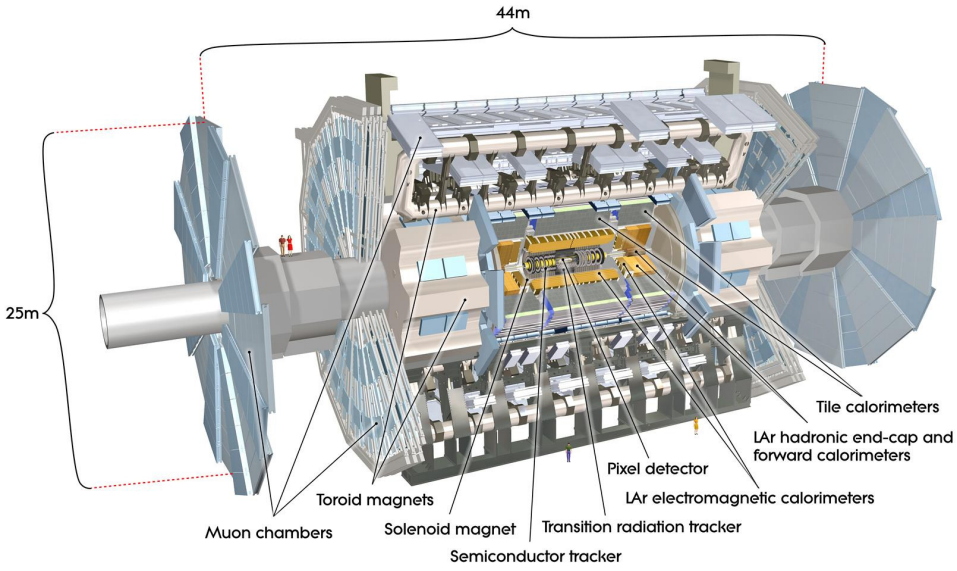

Figure 8.1: Cartoon of the ATLAS detector

8.1 Inner Tracker

The main purpose of the inner tracker is to measure the position and momentum of charged particles. This information is crucially important when trying to identify jets that originated from the decay of b-hadrons. The inner tracker, shown in Fig. 8.2(a), is composed of barrel and forward silicon pixel detectors, barrel and forward semi-conductor tracker, and finally a transition radiation detector system.

8.1.1 Pixel System

The pixel system, as shown in Fig. 8.3(a), is a silicon based detector and is the inner most detector with respect to the beam pipe and offers coverage up to $|\eta| = 2.5$. It is composed of 80 million silicon pixels 50 x 400 μm^2 in size spread across three

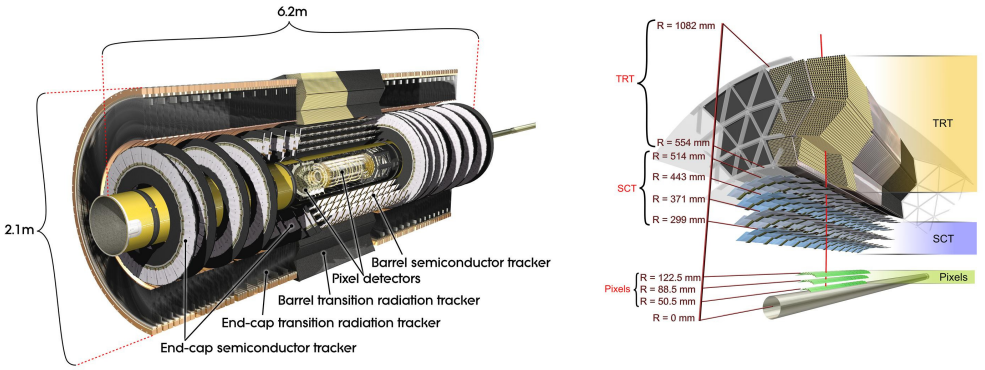

(a) (b)

Figure 8.2: 3D rendition of the Inner Tracking system 8.2(a) and 8.2(b) exploded view of the inner tracker barrel

barrel layers and three disks per end-cap. Silicon based detectors work by collecting the charges released due to traversing charged particles in the depleted volume of the diode. There are 1744 modules in the entire system. An exploded view of one of the barrel modules is shown in Fig. 8.3(b).

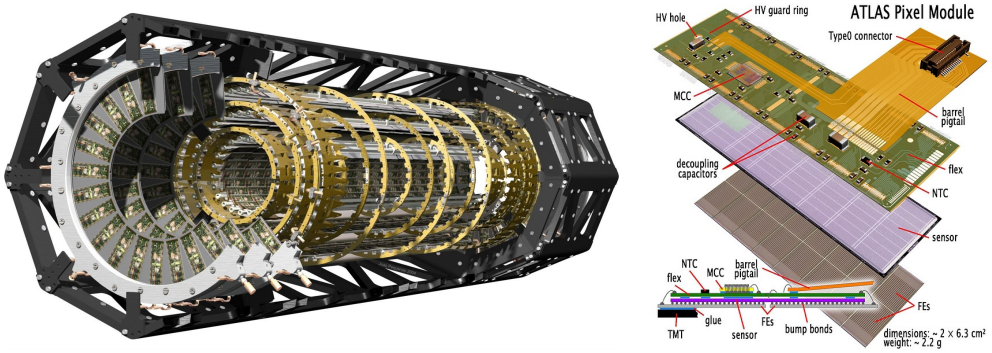

(a) (b)

Figure 8.3: 3D rendition of the pixel detector 8.3(a) and 8.3(b) exploded view of a pixel module.

8.1.2 Semi-Conductor Tracker

The semi-conductor tracker (SCT) is what could be considered the middle component of the inner tracking detector and, similar to the pixels, covers up to $|\eta| = 2.5$. The SCT is composed of six-million silicon micro-strips arranged in four barrel layers and nine disks per end-cap. Each strip is $80\mu m$ x $12cm$ and there are 2 layers per module, attached anti-parallel at a 40 $mrad$ stereo angle to allow for a second coordinate measurement per module. A schematic of a barrel module is shown in Fig. 8.4. The SCT, in combination with the pixel detector, has the ability to measure the momentum, impact parameter and vertex origin of charged particles.

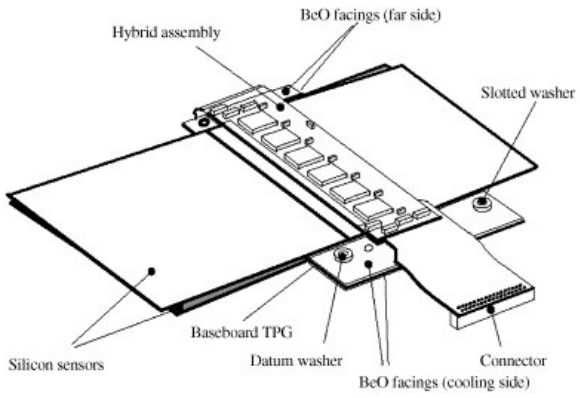

Figure 8.4: ATLAS SCT Barrel Module

8.1.3 Transition Radiation Tracker

The transition radiation tracker (TRT) is the outermost detector of the inner tracking detector. The TRT is composed of around 300,000 straw-tubes (commonly referred to as drift tubes) that act both as trackers (each TRT straw hit acts as a space

point measurement) and transition radiation detectors (radiators between the straws produce detectable X-rays when high energy electrons pass through them, allowing for efficient electron identification). There are 50,000 straws in the barrel region that are each $144cm$ long and 125,000 straws $39cm$ long in each of the end-caps. The straw tubes are each $4mm$ in diameter with a $0.03mm$ diameter gold plated tungsten wire in the middle. The tubes are filled with a $70/27/3\%$ mixture of $Xe - CO_2 - O_2$ that results in efficient transition radiation absorption, high electron drift velocities and sufficient aging resistance [14].

8.2 Calorimeter System

A calorimeter is a type of particle detector that measures an incident particle or jet's position and energy by completely absorbing their energy. In general, a calorimeter is composed of a dense absorbing material that causes incident radiation to shower and some active material that produces some measurable output proportional to the incident particle or jet energy. In homogeneous calorimeters, the absorber and active material are the same. More commonly, however, the two materials are different. There are two types of calorimeters, categorized by the ratio of their response to electromagnetic versus hadronic showers (commonly referred to as e/h). Those being, not surprisingly, electromagnetic and hadronic calorimeters. The former absorbs energy from electromagnetic particles such as the electron and photon, while the latter absorbs energy from particles that interact via the strong nuclear force. The ATLAS calorimeter

contains both of these types in the form of the liquid argon (LAr) and scintillating tile calorimeters. Both of these are located outside of the 2 T solenoidal magnet as shown in Fig. 8.5.

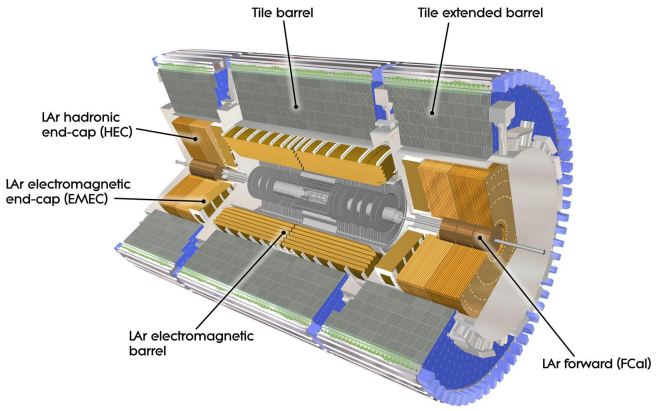

Figure 8.5: 3D rendering of the ATLAS calorimeters

8.2.1 Liquid Argon Calorimeter

A liquid argon calorimeter is a class of ionizing calorimeters. The concept is that radiation incident on the absorbing material begins to shower. This shower then passes through the active detector medium, in this case liquid argon, resulting in the liberation of electrons that are collected on readout electrodes. There are four different LAr calorimeters in the ATLAS detector: electromagnetic barrel (EMB), electromagnet end-cap (EMEC), hadronic end-cap (HEC) and forward (FCal).

The EMB has a very unique accordion design in order to ensure there are no azimuthal gaps, as seen in Fig. 8.6(a). The absorbers are made of stainless steel clad lead

and are separated by a honeycomb material that maintains the LAr gap. The EMEC is of similar design to the EMB, with the same accordion absorber-active shape, but are instead stacked into a cylindrical end-cap wheel as opposed to a barrel. See Fig. 8.6(b). Both the EMB and EMEC sit in cryostats that keep the LAr at a temperature near 90 Kelvin.

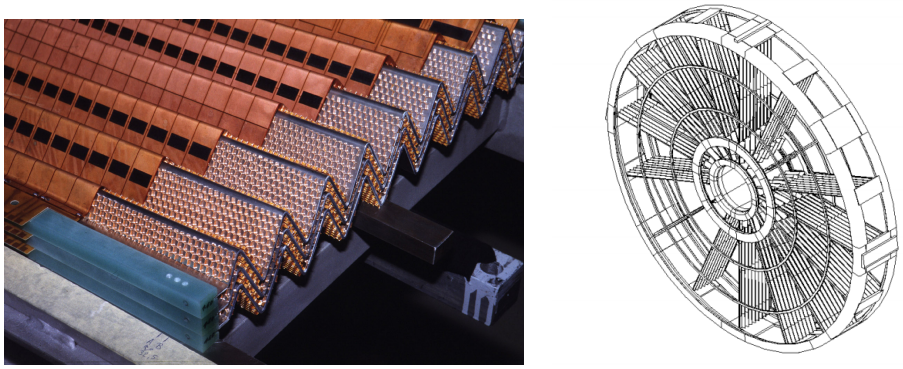

(a) (b)

Figure 8.6: Picture of an EMB accordion module 8.6(a) and 8.6(b) graphic of the EMEC with a few accordion sheets

The HEC is composed of four wheels, two per end-cap, and is situated directly behind the EMEC. Due to the large number of interaction lengths necessary to contain and absorb jets from the high energy collisions, copper, instead of lead, was chosen as the absorber material. The HEC and EMEC sit in the same cryostat in each end-cap.

The FCal has a completely different design from the other LAr calorimeters. It is composed of many cylindrical layers with a matrix of absorber tubes. There are three separate FCal regions per end-cap. FCal 1, closest to the interaction point, is composed of copper electrodes and copper absorbers and is an EM calorimeter. FCal 2

and 3 are composed of tungsten electrodes and tungsten absorbers. In all three regions, the absorber tubes are filled with electrode rods wrapped with thin quartz fiber, as shown in Fig. 8.7, resulting in a very small LAr gap ($269\mu m$, $376\mu m$, and $508\mu m$ for FCal 1, 2 and 3, respectively). There are a total of 61368 electrodes and 3524 readout channels. The FCal also has a large brass plug after FCal 3 that is in place to reduce hadronic punch through to the muon spectrometers.

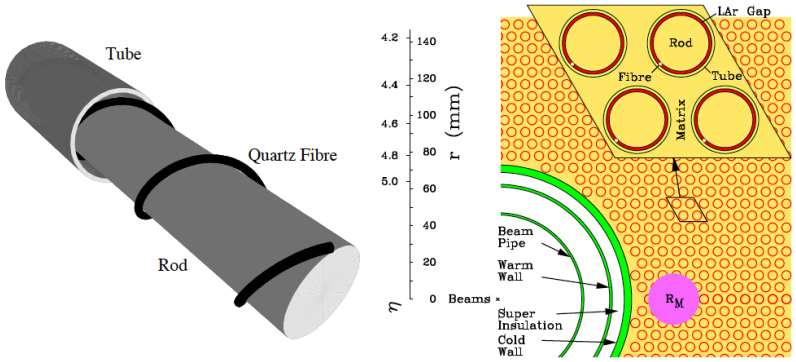

Figure 8.7: Diagram of an exposed rod, showing the spiral quartz fiber (left), as well as the front face of the FCal 1 module, showing the matrix of absorbers and electrodes.

8.2.2 Tile Calorimeter

A scintillator is a device that emits a small burst of light when a charged particle passes through it. When coupled to a photomultiplier, these light pulses can be converted to an electrical signal that is proportional in some way to the incident radiation. The ATLAS tile calorimeter (TileCal) is a hadronic calorimeter composed of tiles of scintillating plastic (polystyrene) supported by a steel absorbing structure. The TileCal is composed of around 500,000 tiles organized into wedges, as seen in

Fig. 8.8 [21]. The barrel, which is outside of the EMB calorimeter, contains 64 wedges and the extended barrel that lies outside the LAr end-cap cryostats, contains 64 wedges per side.

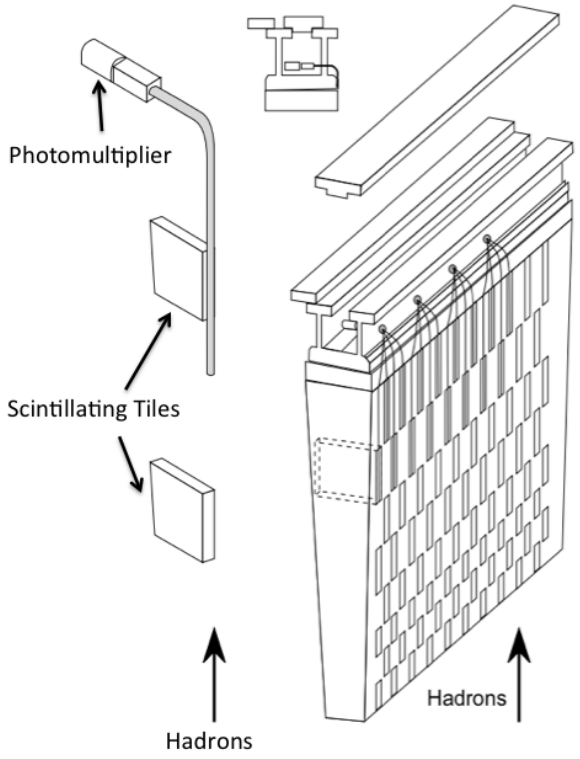

Figure 8.8: Concept of an ATLAS Tile Calorimeter wedge

8.3 Muon Spectrometer

The ATLAS muon spectrometer is used to identify muons and measure their momenta and direction by utilizing a combination of trigger chambers and precision measurement chambers. The thin gap chambers (TGC) and resistive plate chambers (TGC) provide the triggering capabilities while the monitored drift tubes (MDT) and

the cathode strip chambers (CSC) provide the precision momentum measurements. These sub-detectors are described in more detail below. The entire spectrometer is contained within a toroidal magnetic field. The ATLAS magnet system is described in more detail in Section 8.4. The four subsystems are shown in a 3D view in Fig 8.9 as well as a 2D cross-sectional view of a single quadrant in Fig. 8.10.

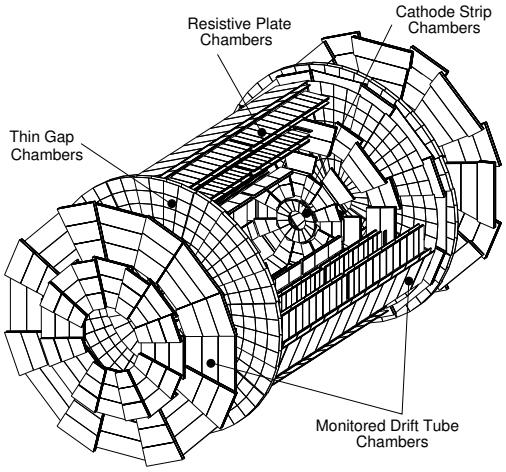

Figure 8.9: Three dimensional view of the ATLAS muon spectrometer system.

8.3.1 Monitored Drift Tubes

The MDTs are a type of gaseous ionization detector. They are cylindrical proportional drift tubes composed of an anode wire in the center of a 30mm cathode tube that is filled with a non-flammable 91%/4%/5% mixture of Ar, N_2 and CH_4 held at 3 bar absolute pressure. When a charged particle passes through the volume of the

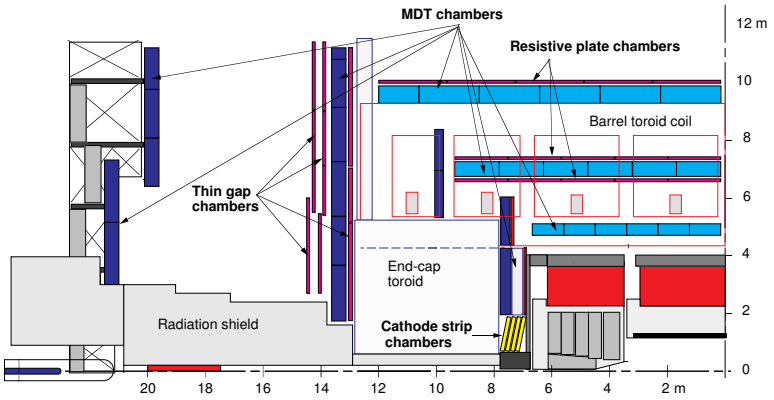

Figure 8.10: Two dimensional cross-section of one quadrant of the ATLAS muon spectrometer system.

drift tube, it ionizes the gas, resulting in a number of free electrons. The freed electrons are then accelerated towards the anode wire due to the applied electric field (resulting from an applied potential of 3.27 kV). While the freed electrons are accelerating, they ionize more of the gas, resulting in additional free electrons. This process is called a multiplication avalanche, but is also commonly called a Townsend avalanche. Fig. 8.11 illustrates this concept. The number of electron-ion pairs in the avalanche is directly proportional to the initial number of freed electrons (which is dependent on the energy of the incident particles), hence the term, proportional chamber.

In ATLAS, the MDTs provide pseudo-rapidity coverage up to $|\eta| < 2.7$ and cover a physical area of almost 5500 m^2. In addition to providing precision muon coordinate measurements, the chambers have a monitoring system to track any internal deformation that may occur. A single MDT tube schematic is shown in Fig. 8.12(a) while a schematic of a single MDT module consisting of at least 6 and at most 8 parallel layers of tubes is shown in Fig. 8.12(b). Overall, there are 1194 chambers installed.

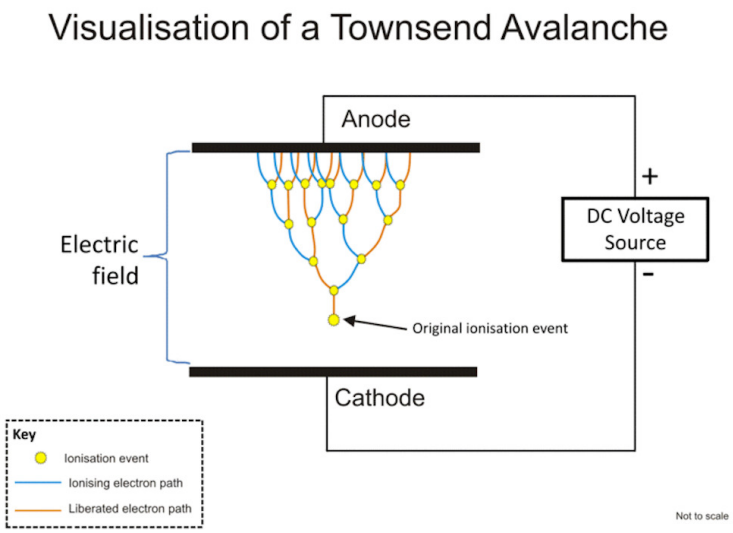

Figure 8.11: Graphic illustrating how a charged particle passing through a gaseous detector with an applied electric field results in a multiplication, or Townsend avalanche of ionized electrons.

8.3.2 Cathode Strip Chambers

The CSCs are multi-wire proportional chambers and are composed of a plane of anode wires in between two cathode plates, as shown in Fig. 8.13. For ATLAS, s=d=2.54mm and W=5.6mm. They provide forward precision muon measurements between $2.0 < |\eta| < 2.7$. The CSCs are a necessary addition to the MDTs due to the high counting rates expected in the forward regions where the MDTs are no longer suitable. The small gas volume as well as the lack of hydrogen in the gas mixture of 30 Ar/50 CO_2/20 CF_4 results in very low neutron and γ sensitivity ($< 10^{-4}$ and ≈ 0.01, respectively). Additionally, they are held at a relatively low voltage, 2.6kV, lowering the possibility of electric breakdown due to high particle flux. The CSCs provide the minimal required spatial resolution of 80 μ m. This spatial measurement is made by

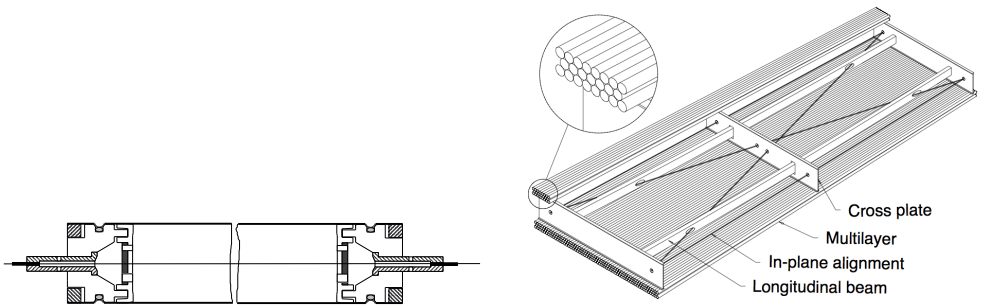

(a) (b)

Figure 8.12: Schematics of an MDT tube (a) and one of the 6-layer MDT modules (b).

measuring the charge on the cathode strips induced by the negative charge avalanche on the anode wire, as illustrated in Fig. 8.14. The TDR called for 32 four-layer

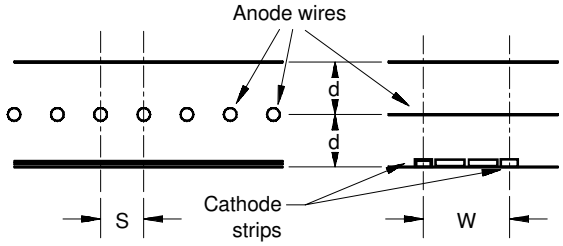

Figure 8.13: Schematic cross section of the CSC

chambers to be installed for Run 1. However, due to many factors, there were only 16 installed (8 per side of the interaction point). Fig. 8.15(b) illustrates how the CSCs are mounted at an 11.59° angle to reduce the number of inclined tracks, a source of resolution degradation. They are mounted on a rigid aluminum structure called the Small Wheel.

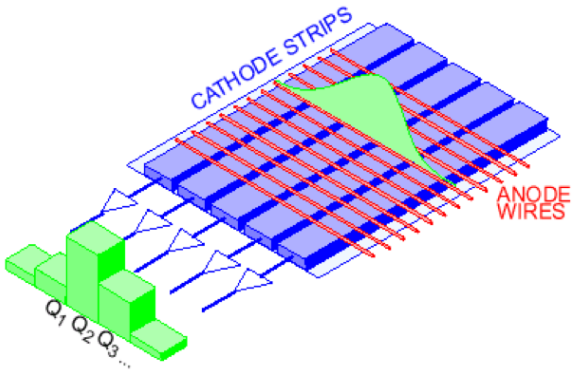

Figure 8.14: Illustration of how the induced charge on the adjacent cathode strips is read out to determine the muon's position.

8.3.2.1 Personal contributions to the CSCs

During the six months before beginning graduate studies at the University of California Santa Cruz, I was a technician working on installing services for the CSCs on the small wheel. I designed and implemented the routing scheme for the water, gas, optical as well the low and high voltage services. Additionally, I installed and commissioned the chamber thermal sensors.

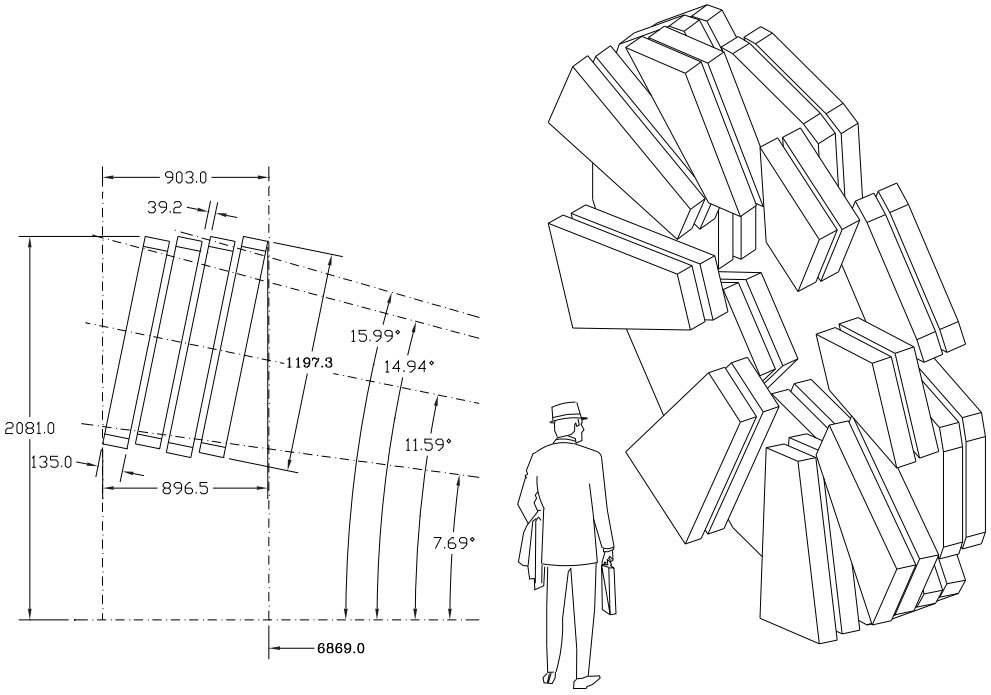

(a) (b)

Figure 8.15: Figure (a) illustrating the inclination of the CSCs and (b) the physical arrangement of the CSC as they would be mounted on the small wheel.

8.3.3 Resistive Plate Chambers

The RPCs provide muon triggering capabilities for the barrel region of the ATLAS detector, covering $0 < |\eta| < 1.0$. These detectors are a type of gaseous parallel-plate detectors, so there are no wires within the gaseous volume. They are composed of two parallel resistive plates made of Bakelite separated from one another by insulating spacers. A uniform electric field on the order of a few kV / mm produces the multiplication avalanche. A 97%/3% mixture of tetraflouroethane ($C_2H_2F_4$) and iso-C_4H_{10} was used. A cross sectional schematic is shown in Fig. 8.16.

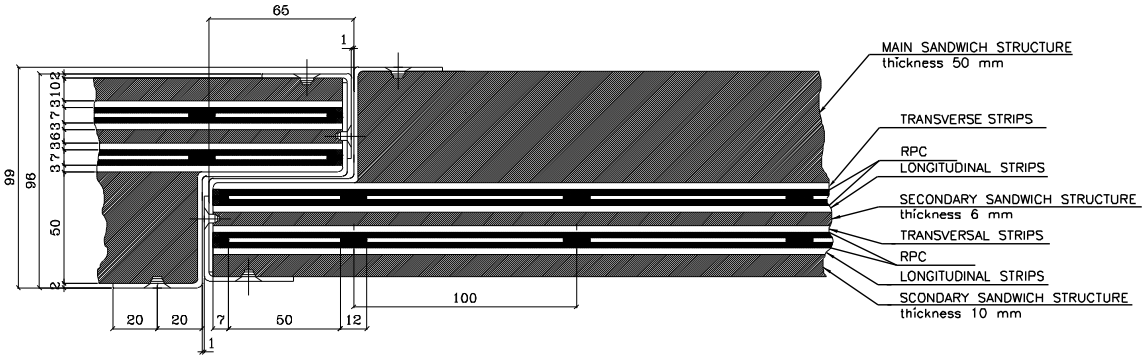

Figure 8.16: Cross-sectional schematic of an RPC chamber.

There are three barrel trigger stations, each made up of two detector layers. The inner two layers are located about 7 meters from the beam axis, 50cm apart. These two layers provide the low p_T trigger ($p_T < 6$ GeV). The outer layer, located outside the barrel toroid magnet 10 meters from the beam line provides high p_T ($p_T > 20$ GeV) triggering capabilities. Four out of the three inner trigger detectors must fire to pass the low p_T logic, while just one out of the two outer detector layers must trigger to pass

the high p_{T} trigger logic.

8.3.4 Thin Gap Chambers

The TGCs provide forward muon triggering coverage past that of the RPCs, out to $1.0 < |\eta| < 2.4$. Additionally, they are able to measure the azimuthal coordinate of particles to complement the bending coordinate of the MDTs. They are structurally similar to the multi-wire proportional chambers that we described earlier, however they operate in saturated mode and have a different anode-to-anode and cathode-to-anode distance (recall that these distances are the same in the case of the CSCs). The TGCs use a highly quenching gas composed of a 55/45 percent mixture of CO_2 and n-pentane (n-C_5H_12). A cross sectional schematic of the TGCs is shown in Fig. 8.17.

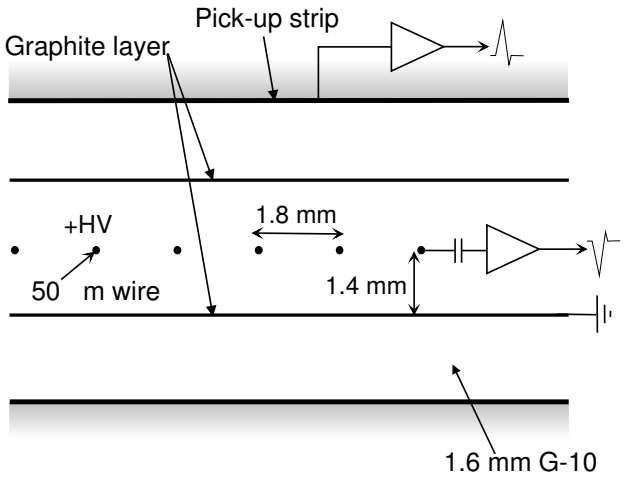

Figure 8.17: Cross-sectional schematic of an TGC chamber.

Thera are 7 layers of TGC chambers for each end-cap, composed of one triplet structure and two double structures. The triplet structure is located closer to the beam

line while the two doublets are located at a $z \approx 14m$. Similar to the RPC trigger logic, two of the three inner triplet detectors must fire to signal the low-p_{T} trigger, while if 3 out-of-4 of the four detectors fire in combination with the 2-out-f-3, the signal passes the high-p_{T} trigger logic. The triplet and double layers are shown, not to scale, in Fig. 8.18.

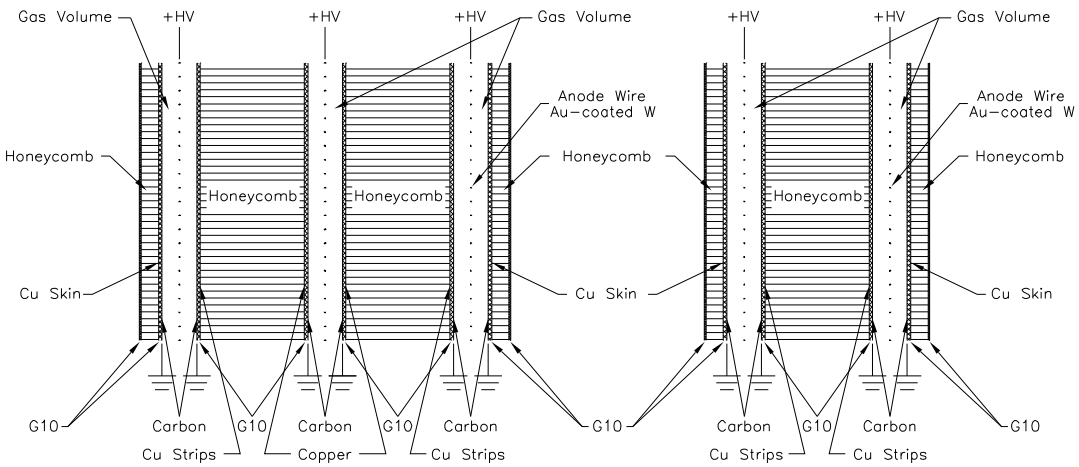

Figure 8.18: Cross-sectional schematic of the triple and double TGC structures.

8.4 Magnet Systems

Two superconducting magnet systems ATLAS, namely the central solenoid and toroidal magnets, provide the bending force on charged particles required for precision momentum measurements of these particles.

8.4.1 Solenoid

The central solenoidal magnet system provides a two Tesla field for the inner tracking detectors described earlier. The solenoidal field has axial symmetry, however it is not symmetric with respect to the beam axis. In order to minimize the amount of materials used, the solenoid is situated within the LAr cryostat. The return yoke of the magnetic field is provided by the iron material in the barrel and extended barrel tile calorimeter systems described in Section 8.2.2. The superconducting strands within each cable are 1.2mm in diameter and composed of NbTi/Cu. These strands are arranged in a 2x6 configuration and are supported by indirectly cooled aluminum stabilizing material. The overall size of each superconducting cable is 2.2x7.4mm^2. Each cable is then coated with a polymide film for electrical insulation from the support structure.

8.4.2 Barrel Toroid

Located outside of the ATLAS calorimeters, the barrel toroid system provides a peak magnetic field of around four Tesla. It provides the magnetic field necessary for bending the path of charged particles that escape the calorimeters and are detected in the central muon spectrometers, namely muons. The air toroid system is composed of eight "racetrack" coils aligned radially in a torus configuration that is axially symmetric. The superconducting strands are composed of the same material as those in the solenoidal magnet system in slightly different proportions with a similar diameter of 1.3mm. There are 38 strands per superconducting cable. Overall, there are 120 turns of the superconducting cable per coil, resulting in a total length of close to 56km for

the entire system. Each of these coils are contained within their own cryostats and are cooled using liquid Helium to a temperature close to 4 Kelvin.

8.4.3 Endcap Toroids

The end cap toroids provide a forward magnetic field responsible for the bending force needed in the precision measurement of muons. The peak magnetic field is slightly above four Tesla. Similar to the solenoidal toroid magnets, the superconducting elements are arranged in a 8 racetrack like structures per side and cooled to close to zero Kelvin using cryostats, as shown in Fig. 8.19.

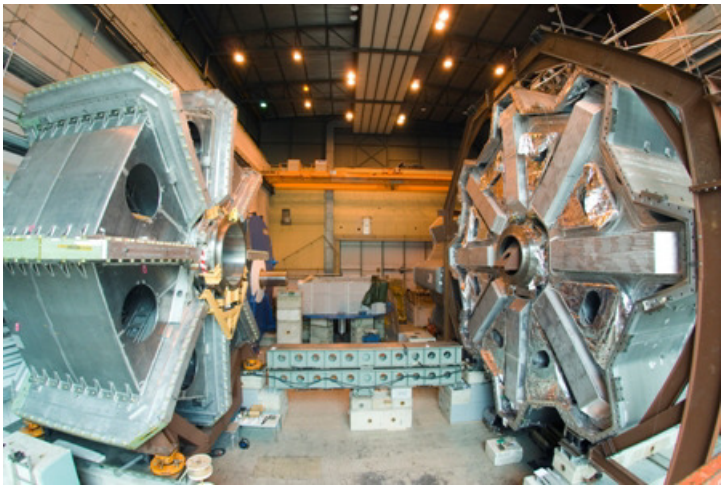

Figure 8.19: Both of the End-cap toroids. The magnet on the left is exposed and has not been installed in its cryostat, while the one on the right is partially installed.

8.5 Trigger

The ATLAS trigger system is composed of both hardware and software triggers that decide whether or not an event will be written to disk. While it would be ideal to

save every single event, hard drive storage and processing power limitations require a reduction in the number of events written to disk from 1 GHz to less than 100 KHz. The Level 1 (L1) trigger is completely hardware based and relies on raw information from calorimeters (for the identification of photons, jets, electrons, etc.) as well as trigger chambers (the RPC and TGC) for decisions about muons. The L1Calo system builds trigger towers by first summing over the EM and hadronic calorimeters cells. This information is then digitized and categorized based on the amount of hadronic vs. EM energy. Ultimately, the result is a count of jet like objects that have transverse energy above a set threshold. The L1Muon system works very similarly in that hits are looked for on the TGC and RPC stations. Depending on the number of hits as well as the number of coincidental hits between each station, the muons are categorized as either high p_{T} or low p_{T} in up to 16 regions of interest (ROI) in $p_{\mathrm{T}}, \eta, \phi$. The information from the L1Calo and L1Muon triggers is then used to build regions of interest that are sent to the Level 2 trigger system that uses the entire detector. Finally, the event filter (EF) incorporates alignment and calibration and processes the events offline (not in real time).

Part IV

Datasets from Collisions and Monte Carlo Simulations

Chapter 9

Data

The data were collected from the ATLAS detector at the LHC located at CERN in 2012. Since this analysis is looking for jets with very large p_{T} as well as events with a large amount of total transverse momentum, the data collected was triggered on an H_{T} trigger, where the H_{T} is the scalar sum of all of the transverse energy in an event:

- `EF_j170_a4tchad_ht700`

Additional high p_{T} fat-jet as well as multi-jet triggers were investigated; however the H_{T} trigger was the most efficient with respect to the four-top signals.

The collected data correspond to a total of 20.3 fb^{-1} integrated luminosity were collected during the 2012 running campaign using the above unprescaled triggers as shown in Table 9.1. The uncertainty on the integrated luminosity is $\pm 2.8\%$. It is derived, following the same methodology as that detailed in Ref. [70], from a preliminary calibration of the luminosity scale derived from beam-separation scans performed in November 2012. The trigger efficiency turn-on curves are shown as a function of H_{T} in

Fig. 9.1 for events with $H_{\mathrm{T}} > 500$ GeV [1]. The turn-on curve is shown on top of the H_{T} distributions for a range of 2UED-RPP and Sgluon signals.

Period	Delivered Lumi.	Trigger Chain	L1 Seed	L2 Chain
A3-L3	20.344 fb^{-1}	EF_j170_a4tchad_ht700	L1_J75	L2_j165_c4cchad

Table 9.1: Total integrated luminosity pre-scale corrected in 2012 for the selected triggers. This trigger is unprescaled (less than 1% prescale)

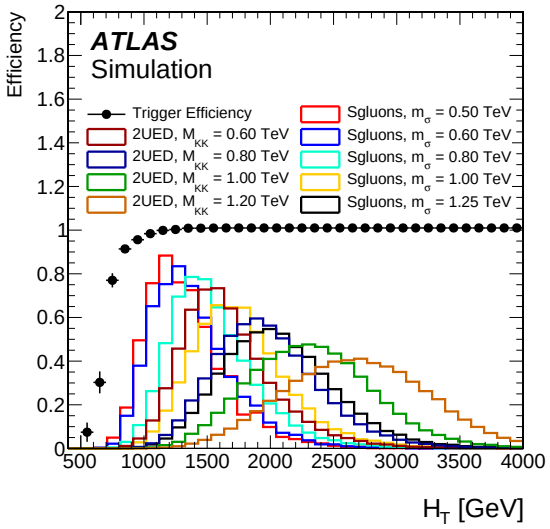

Figure 9.1: Trigger efficiency as a function of H_{T} for the `EF_j170_a4tchad_ht700` trigger.The points are the efficiency curve while the solid lines are the H_{T} and p_{T} distributions, before trigger requirements are applied. The H_{T} distribution is normalized to unity.

[1] The definition of H_{T} is described in Section 11

Chapter 10

Monte Carlo Samples

10.1 Signal

In this section we describe the generation, simulation and reconstruction of the signal Monte Carlo events used in this analysis. The models are described in Part II and the information below is summarized in Table 10.2, while the production cross sections and expected number of events before selection are described in Table 10.1.

The 2UED-RPP signal samples are generated using MadGraph 5 [20]. The Kaluza-Klein particles generated are then decayed to the level of the top-(anti-) top quark states with BRIDGE [75], a branching fraction calculator / decay program. The resulting events are stored in the LHEF [18] event format. Parton showering of the resulting decay products is then handled by Pythia8 [88]. Events are then simulated using the full GEANT4 [16] detector simulation. The scale gluon events are generated using Pythia 6 [89], where the scaler gluons are completely decayed down to top quarks

and anti-top quarks. Parton showers are also handled by Pythia 6. Events are simulated using the ATLAS fast detector simulation, ATLFastII [85] [69]. Events from both the composite top-quark contact interactions as well as predicted Standard Model events were generated using MadGraph5, showered with Pythia8 and simulated using the GEANT4 ATLAS simulation software. All samples were reconstructed with the most recent recommended Athena software release.

10.2 Background

In this section we describe the background Monte Carlos programs used for both event selection optimization and background estimation. We expect our largest backgrounds to be $t\bar{t}$ and QCD di-jet events. However, we also check the contributions from single-top as well as $t\bar{t} + X$, where X is W+jets, Z+jets and WW. The details below are also summarized in Table 10.3.

10.2.1 $t\bar{t}$

Our baseline $t\bar{t}$ Monte Carlo samples are generated using Powheg [79], Sherpa [27] and MC@NLO [53] matrix element generators, all using the CTEQ10 PDF set [67]. The Powheg events are showered using Pythia8. The Sherpa events are generated with up to four additional partons in the final state, giving us a prediction of the $t\bar{t}$ plus heavy flavor contribution. The Sherpa generator handles not only the matrix element generation, but also the showering. Our only next-to-leading order events generated from MC@NLO are showered using Herwig++. We compare these three generators

Model	Cross-section [fb]	K-factor	Number of events for 20.34 fb^{-1}
2UED-RPP			
m_{KK} = 600 GeV	1284.5	1.0	26120
m_{KK} = 800 GeV	113.89	1.0	2317
m_{KK} = 1000 GeV	11.719	1.0	238.4
m_{KK} = 1050 GeV	6.6800	1.0	135.9
m_{KK} = 1100 GeV	3.8100	1.0	77.50
m_{KK} = 1150 GeV	2.1500	1.0	43.73
m_{KK} = 1200 GeV	1.2215	1.0	24.85
m_{KK} = 1250 GeV	0.6800	1.0	13.83
m_{KK} = 1300 GeV	0.38	1.0	7.729
m_{KK} = 1350 GeV	0.21	1.0	4.271
Scalar Gluons			
m_{σ} = 350 GeV	8267.2	1.7946	301770
m_{σ} = 400 GeV	3529.9	1.8563	133279
m_{σ} = 500 GeV	780.21	1.9826	31462.8
m_{σ} = 600 GeV	207.09	2.1062	8871.76
m_{σ} = 800 GeV	20.211	2.3735	975.726
m_{σ} = 1000 GeV	2.5464	2.7127	140.500
m_{σ} = 1250 GeV	0.23293	3.1859	15.0941
Contact	42.238	1.0	859.1
Standard Model	1.3	1.0	26.44

Table 10.1: Signal cross sections for several 2UED-RPP and scalar gluon mass points as well as for contact interactions and for comparison, the SM four-top cross section. The predicted number of events assuming an integrated luminosity of 20.34 fb^{-1} is also shown. All models assume a 100% branching fraction to four top-quarks plus potentially other final state particles (leptons and jets). A k-factor of 1.0 indicates a leading order prediction and that we do not know the NLO k-factor value.

Model	PDF	Event Generator	Showering	Simulation	No. of Events
2UED-RPP					
$m_{KK} = 600$ GeV	MSTW 2008 LO	MadGraph 5	Pythia8	GEANT4	190000
$m_{KK} = 800$ GeV	MSTW 2008 LO	MadGraph 5	Pythia8	GEANT4	190000
$m_{KK} = 1000$ GeV	MSTW 2008 LO	MadGraph 5	Pythia8	GEANT4	150000
$m_{KK} = 1050$ GeV	MSTW 2008 LO	MadGraph 5	Pythia8	GEANT4	150000
$m_{KK} = 1100$ GeV	MSTW 2008 LO	MadGraph 5	Pythia8	GEANT4	150000
$m_{KK} = 1150$ GeV	MSTW 2008 LO	MadGraph 5	Pythia8	GEANT4	150000
$m_{KK} = 1200$ GeV	MSTW 2008 LO	MadGraph 5	Pythia8	GEANT4	150000
$m_{KK} = 1250$ GeV	MSTW 2008 LO	MadGraph 5	Pythia8	GEANT4	150000
$m_{KK} = 1300$ GeV	MSTW 2008 LO	MadGraph 5	Pythia8	GEANT4	150000
$m_{KK} = 1350$ GeV	MSTW 2008 LO	MadGraph 5	Pythia8	GEANT4	150000
Scalar Gluons					
$m_{\sigma} = 350$ GeV	CTEQ6L1	Pythia 6	Pythia 6	ATLFast II	350000
$m_{\sigma} = 400$ GeV	CTEQ6L1	Pythia 6	Pythia 6	ATLFast II	250000
$m_{\sigma} = 500$ GeV	CTEQ6L1	Pythia 6	Pythia 6	ATLFast II	100000
$m_{\sigma} = 600$ GeV	CTEQ6L1	Pythia 6	Pythia 6	ATLFast II	50000
$m_{\sigma} = 800$ GeV	CTEQ6L1	Pythia 6	Pythia 6	ATLFast II	50000
$m_{\sigma} = 1000$ GeV	CTEQ6L1	Pythia 6	Pythia 6	ATLFast II	50000
$m_{\sigma} = 1250$ GeV	CTEQ6L1	Pythia 6	Pythia 6	ATLFast II	50000
Contact	MSTW 2008 LO	Madgraph 5	Pythia 8	GEANT4	190000
Standard Model	MSTW 2008 LO	Madgraph 5	Pythia 8	GEANT4	200000

Table 10.2: Four top-quark final state signal Monte Carlo samples.

at every step of the analysis chain; however we are following the recommendation of the Top Working Group and will use the Powheg+Pythia8 events for our baseline $t\bar{t}$ background prediction.

10.2.2 QCD di-jet

Two sets of weighted Monte Carlo samples were used to model the QCD di-jet background. The first was generated with Pythia8 using the AU2 underlying event tune [2] and the CTEQ10 PDF set. The events were also showered using Pythia8. This set of MC events is generated in slices of leading jet p_{T} and labeled JZxW where the x lies in the range of 0-7 corresponding to the Anti-k_t R=0.6 Truth Jet p_{T} ranges 0-20, 20-80, 80-200, 200-500, 500-1000, 1000-1500, 1500-2000 and 2000+ GeV. Events in these samples are weighted appropriately such that when combined, the leading jet p_{T} distribution is smooth and falling. The second sample used has events generated with Herwig++ using the EE3 underlying event tune [55] as well as the CTEQ6L PDF set [84]. The events are also showered using Herwig++. This set of MC events is also generated in slices of leading jet p_{T} and labeled JZxW where the x lies in the range of 0-7. These samples are used in the initial validation of various kinematic shapes in control regions as well as to validate our background estimation method. However, these samples are not used for final background event count or shape predictions. Due to the selection in this analysis, we are only using the JZxW samples with truth jet $p_{\mathrm{T}} > 200$ GeV.

10.2.3 Single top

The single-top baseline samples are used to show the potential contribution of single top-quark production events in loose selection control regions. The t-channel single-top events are produced with the AcerMC [62] generator using the CTEQ6L1 LO PDF set. Showering is handled with Pythia 6 with the P2011C underlying event tune [90]. The s- and Wt-channels are generated with the Powheg generator using the CT10 NLO PDF set. Showering is again handled using Pythia 6 with the P2011C underlying event tune. These events are used in the loose selection control regions to show potential contributions, however they are not used for final background estimates. Any residual hadronic contributions from single top will be estimated as part of the data driven background estimation.

10.2.4 $t\bar{t} + X$

As with the single-top samples, we will use these samples to show potential contributions from $t\bar{t} + X$, where X represents W, Z, WW, W+jets and Z+jets. All of these events are generated with Madgraph using the CTEQ6L1 LO PDF set. The parton shower and hadronization are handled with Pythia 6 using the AUET2B underlying event tune. These events are shown in validation distributions for reference, however they are not included in any numerical or shape driven background estimation.

Model	Run No.	PDF	Event Generator	Showering	No. of Events
$t\bar{t}$					
Powheg	1170[49,50]	CT10	Powheg	Pythia8	24993661
Sherpa	11780[0,9]	CT10	Sherpa	Sherpa	23175238
MC@NLO	10520[0,4]	CT10	MC@NLO	Herwig++	16197093
QCD di-jet					
Herwig JZxW	15911[3-7]	CTEQ6L1	Herwig++	Herwig++	1.4M / sample
Pythia JZxW	14791[3-7]	CT10	Pythia8	Pythia8	3-6M / sample
Single top					
AcerMC t-channel	110101	CTEQ6L1	AcerMC	Pythia8	8997672
Powheg s-channel	110119	CT10	Powheg	Pythia8	1199895
Powheg Wt-channel	110140	CT10	Powheg	Pythia8	999692
$t\bar{t} + X$					
$t\bar{t} + W$	119353	CTEQ6L1	MadGraph	Pythia6	400000
$t\bar{t} + W$j	119354	CTEQ6L1	MadGraph	Pythia6	400000
$t\bar{t} + Z$	119355	CTEQ6L1	MadGraph	Pythia6	400000
$t\bar{t} + W$j	119356	CTEQ6L1	MadGraph	Pythia6	400000
$t\bar{t} + WW$	119583	CTEQ6L1	MadGraph	Pythia6	10000
$t\bar{t} + W$j Excl	174830	CTEQ6L1	MadGraph	Pythia6	400000
$t\bar{t} + W$jj Excl	174831	CTEQ6L1	MadGraph	Pythia6	400000
$t\bar{t} + Z$j Excl	174832	CTEQ6L1	MadGraph	Pythia6	400000
$t\bar{t} + Z$jj Excl	174833	CTEQ6L1	MadGraph	Pythia6	400000

Table 10.3: Background Monte Carlo samples used in this analysis

Part V

Event Selection and Results

Chapter 11

Object Identification and Event Selection

11.1 Object Selection

Two types of jets are utilized in this analysis. Those are jets reconstructed using the anti-k_t algorithm with conical distance parameter $R = 0.4$ in $\eta - \phi$ space and those reconstructed using the anti-k_t algorithm with $R = 1.0$, the latter of which are commonly called fat-jets. Both types of jets were seeded via clusters calibrated using the local cluster weighting calibration (LCW) [25]. The LCW calibration weights differently contributions to the clusters arising from electromagnetic or hadronic energy deposits. Corrections are applied to both the standard and fat-jets that correct the energy and transverse momentum back to the true physics scale, or, Jet Energy Scale (JES) [10]. These corrections are derived using Monte Carlo simulations as well as in-situ data

driven techniques.

11.1.1 Anti-k_t LCW $R = 0.4$ Jet Selection

In addition to applying a JES correction, a correction is also applied to take into consideration in-time and out-of-time pile-up effects [40]. This correction is dependent on the number of reconstructed vertices as well as the average number of interactions per beam bunch crossing

After the JES and pile-up, jets must have a $p_{\mathrm{T}} > 50$ GeV. Since this p_{T} cut is so high, we do not require that un b-tagged jets pass any jet vertex fraction criteria.

11.1.2 Anti-k_t LCW $R = 1.0$ Trimmed Fat-Jet Selection

Due to their wide angle, fat-jets are particularly susceptible to energy contributions originating from pile-up interactions as well as other soft-energy sources.. The fat-jets in this analysis are first run through a trimming algorithm. This algorithm takes advantage of the fact that contamination from pile-up, multiple parton interactions (MPI), and initial-state radiation (ISR) in the reconstructed jet is often much softer than the outgoing partons associated with the hard-scatter and their final-state radiation (FSR). First, sub-jets of size $R = 0.3$ are formed using the inclusive k_t reconstruction algorithm. Any i^{th} sub-jet with $p_T^i / p_T^{\mathrm{jet}} < 0.05$ is removed from the fat-jet [66].

After the trimming procedure, the remaining fat-jets undergo a jet-mass calibration [11] [7] [6] Following the jet-mass calibration, only fat-jets with $p_{\mathrm{T}} > 350$ GeV are considered as part of the analysis.

Any selected fat jets are used as input to our top-tagging selection criteria that are described in the next section.

11.1.3 Top-tagging criteria

As top quarks become more boosted, the decay products become more collimated. As a general rule of thumb, the opening angle of a particle's decay products is $\Delta R \approx 2m^{\text{jet}}/p_T^{\text{jet}}$. Thus, if our top-quarks have $p_T > 350$ GeV, the opening angle of the W and b quark should be roughly 1.0 [39]. This was the motivation behind both the use of $R = 1.0$ jets as well as the 350 GeV p_{T} cut. To take advantage of the fact that our signal contains four potentially high p_{T} top-quarks, we apply a top-tagging algorithm based on several jet-substructure variables.

Backgrounds to our signal process are composed primarily of two standard model processes: high mass QCD di-jet and $t\bar{t}$ events. Fat-jets originating from QCD di-jet events do not have the same sub-structure as fat-jets originating from the decay of boosted top-quarks. Three substructure variables, namely the k_T splitting scale $\sqrt{d_{12}}$ and N-subjettiness fractions τ_{32} and τ_{21}, take advantage of this fact. These quantities are described below.

- $\sqrt{d_{12}}$: the k_T splitting scale looks at the two hardest k_T sub-jets. d_{12} is then computed by multiplying the minimum p_{T} of the two sub jets by the ΔR[1] between them. QCD events have a splitting scale that is peaked around 15 GeV and rapidly falling. $t\bar{t}$ events, however, have a splitting scale centered around half the top mass,

[1] $\Delta R = \sqrt{\Delta\phi^2 + \Delta\eta^2}$

as shown in Fig. 11.1(a) [34].

$$\sqrt{d_{12}} = \min(p_{T,j1}, p_{T,j2})\ \Delta R_{j1,j2} \tag{11.1}$$

- N-subjettiness: This novel jet-shape, denoted commonly as τ_N where j is 1,2,3 ... N, effectively counts the number of sub-jets in an event. Boosted QCD jets generally originate from single partons, while boosted jets from W boson decay should in principle be composed of two hard sub-jets. Naturally, boosted jets originating from a top quark decay should contain three sub-jets; two from the hadronic W and one from the b-quark. τ_N measures to what degree one of these fat-jets can be considered a jet composed of N sub-jets. As described in [92] [**?**], the ratio of τ_2 to τ_1 (denoted as τ_{21}) and the ratio of τ_3 to τ_2 (denoted as τ_{32}) are actually more powerful quantities. We use both τ_{32} and τ_{21} in this analysis to discriminate between boosted QCD jets and jets originating from boosted top quarks. S A comparison of each of the quantities between QCD di-jet, $t\bar{t}$ and our benchmark signal events is shown in Fig. 11.1. The equation describing τ_N is shown below in general form and for our case where $R = 1.0$ and for $N = 1, ..., 3$

where k represents the k^{th} constituent of the fat-jet.

$$\tau_N = \frac{1}{d_0} \sum_k p_{T,k} \ \min(\Delta R_{1,k}, \Delta R_{2,k}, ..., \Delta R_{N,k}), \tag{11.2}$$

$$d_0 = \sum_k p_{T,k} \ R = p_{T,jet} \ , \text{ for R=1.0}, \tag{11.3}$$

$$\tau_1 = \frac{1}{p_{T,jet}} \sum_k p_{T,k} \ \min(\Delta R_{1,k}), \tag{11.4}$$

$$\tau_2 = \frac{1}{p_{T,jet}} \sum_k p_{T,k} \ \min(\Delta R_{1,k}, \Delta R_{2,k}), \tag{11.5}$$

$$\tau_3 = \frac{1}{p_{T,jet}} \sum_k p_{T,k} \ \min(\Delta R_{1,k}, \Delta R_{2,k}, \Delta R_{3,k}). \tag{11.6}$$

To optimize this tagger, each of these variables are used sequentially. That is, we first cut on the fat-jet p_{T} and then look at the $\sqrt{d_{12}}$ distributions for the QCD di-jet background and our signal (the 2UED-RPP $\mathrm{m}_{KK} = 1$ TeV point benchmark, labeled as S), as shown in Fig. 11.1(a). Given a particular cut value of $\sqrt{d_{12}}$, the remaining number of signal events S and background events B calculated. We then find the $\sqrt{d_{12}}$ cut value that optimizes the log-likelihood ratio, $\sqrt{2((S+B)\log(1+S/B)-S)}$ [41]. Finally, after cutting on both the fat-jet p_{T} and $\sqrt{d_{12}}$, we repeat the above procedure for τ_{32}, shown in Fig. 11.1(b), as well as τ_{21}, shown in Fig. 11.1(c). Below are the values we found to be optimal for this search. Any fat-jet passing these cuts is considered tagged as a top-jet.

- $\sqrt{d_{12}} > 60$ GeV
- $\tau_{32} < 0.775$ GeV
- $\tau_{21} > 0.45$ GeV

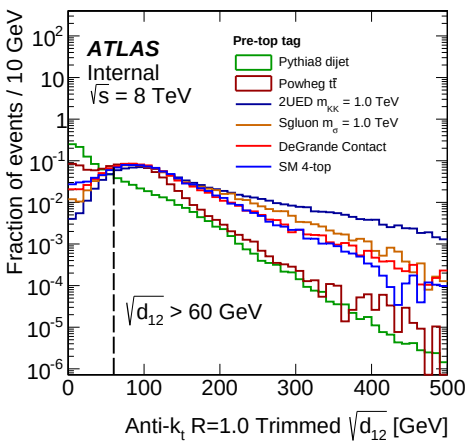

(a)

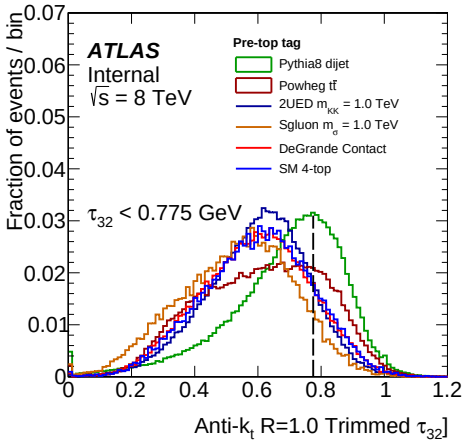

(b)

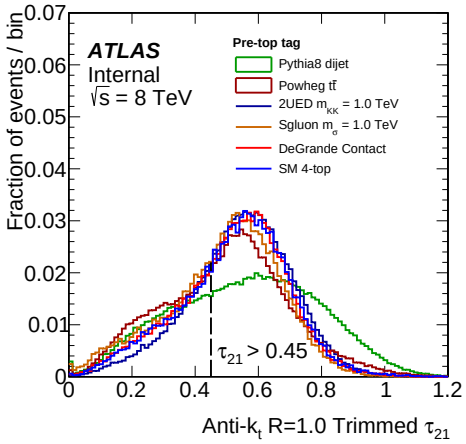

(c)

Figure 11.1: 11.1(a): The k_T splitting-scale $\sqrt{d_{12}}$ after applying the $p_{\mathrm{T}} > 350$ GeV cut. 11.1(b): τ_{32} after applying the $\sqrt{d_{12}} > 60$ GeV cut. 11.1(c): τ_{21} after applying the $\tau_{32} < 0.775$ cut. In each plot, the black dashed line shows the location of the cut to be applied. Histograms are normalized to unity.

With these values, the top-tagging efficiency as a function of p_{T} is found to peak around 50%, as shown in Fig. 11.2 for our target new physics model. This efficiency is defined by matching a top tagged jet to a truth top-quark within $\Delta R = 1.0$. For reference, the $p_{\mathrm{T,top}}^{\mathrm{truth}}$ distributions of of several other new physics models is shown as well. The small bump in the Contact Interaction curve is due to our pre-selection requiring at least two fat-jets with $p_{\mathrm{T}} > 325$ GeV.

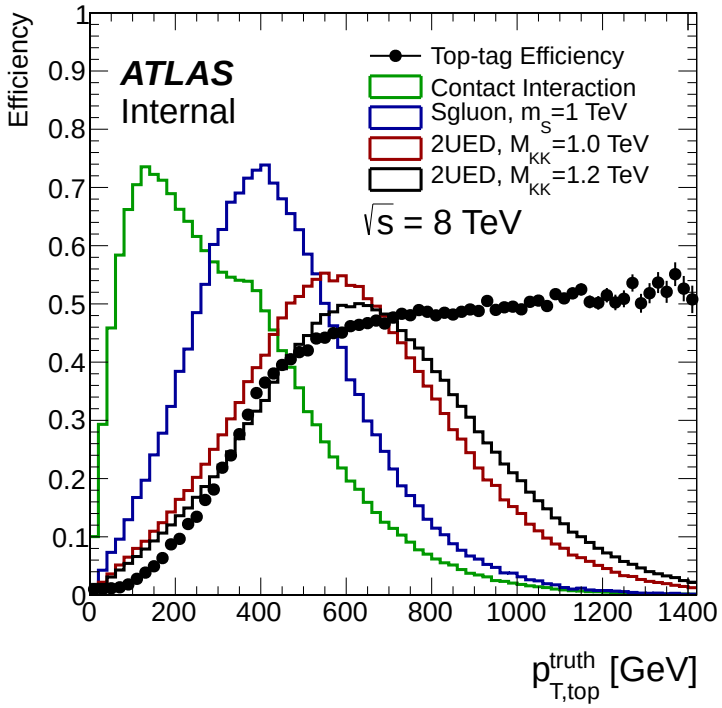

Figure 11.2: Top-tagging efficiency as a function of the truth matched top p_{T}. The $p_{\mathrm{T,top}}^{\mathrm{truth}}$ for several signal samples is also shown for reference. The efficiency is measured from two 2UED ($\mathrm{m}_{KK} = 1.0, 1.2$ GeV) samples by matching tagged fat-jets to truth level top-quarks partons within a ΔR of 1.0.

11.1.4 Top-like fat-jet tagging criteria

In order to show that our background estimation method will work in the signal regions, we require very signal-like control regions to test the method. That is, events in this region look very kinematically similar to those in our signal region. Additionally, the fractional number of $t\bar{t}$ events in this region compared to the data is approximately the same as it is in our two top-tagged regions. To do this, we define a top-like fat-jet (TLFJ). These jets pass the p_{T} requirement as well as the $\sqrt{d_{12}}$ and τ_{32} requirements but fail the τ_{21} requirement. Using these top-like fat-jets, we can test our background estimation methods in regions containing one top-tagged jet and at least one top-like fat-jet to validate the method for use in the two top-tagged regions.

11.1.5 B-tagging criteria

Jets are given a b-tag weight calculated from a combination of machine learning algorithms, combined into a single weight that is labeled MV1. The MV1 b-tagging algorithm is based on a neural network using the output weights of the JetFitter+IP3D, IP3D and SV1 algorithms as input as described in [4]. For our analysis of the signal sample with two or more top-tagged jets, a jet is b-tagged if it has an MV1 weight of at least 0.7892 and lies within $|\eta| < 2.5$ and has a $p_{\mathrm{T}} > 30$ GeV. Charm, tau and light quark rejection factors for each the 70% and 80% working points are given in Table 11.1.

To reduce the possibility of selecting a pile-up jet, if a jet has $p_{\mathrm{T}} < 50$ GeV, we require the Jet Vertex Fraction (JVF) [40] of this jet to be at least 0.5.

Working point	Charm RF	Tau RF	Light Quark RF
70%	4.97	13.24	136.66
80%	3.08	5.49	25.18

Table 11.1: Charm, tau and light quark rejection factors for the 70% and 80% efficiency working points of the MV1 tagging algorithm.

11.1.6 Muon selection criteria

We decided to use muons in the analysis for their contribution to the H_{T}, however we do not require them. Muons are pre-selected based on the following selection criteria as defined by the Muon Combined Performance group.

Tight if any of the following are satisfied

- MuidCombined[2] muon
- MuGirl[3] muon with extended track and (at least two MDT+CSC stations or fewer than six MDT+CSC holes on track)
- MuidStandalone[4] at $|\eta| > 2.5$ and has at least three MDT+CSC stations

For this analysis, we require muons to pass the abode described Tight criteria. We also require the $p_T > 25$ GeV and for the muon to be contained within the psuedorapidity range $|\eta| < 2.5$. Additionally, there is a set of detector hit requirements,

[2]MuidCombined algorithm combines an inner detector track with a muon spectrometer track using a global refit of the two tracks

[3]The MuGirl algorithm performs a search for segments and tracks in the muon spectrometer using an inner detector track as seed.

[4]Moore starts from hit information in the muon spectrometer and produces standalone segments and tracks. MuidStandalone extrapolates the Moore track to vertex and uses a vertex constraint to determine the track parameters at the vertex. MuidStandalone makes Standalone Muons expressed at the vertex

defined below.

- `!expectBLayerHit` or `numberOfBLayerHits > 0` [5]
- Number of pixel hits+number of crossed dead pixel sensors > 0
- Number of SCT hits+number of crossed dead SCT sensors > 4
- Number of pixel holes + number of SCT holes < 3
- A successful TRT extension where expected as defined:
  - Let n_{TRT}^{hits} denote the number of TRT hits on the muon track, $n_{TRT}^{outliers}$ the number of TRT outliers on the muon track, and $n = n_{TRT}^{hits} + n_{TRT}^{outliers}$
  - Case 1: $0.1 < |\eta| < 1.9$. Require $n > 5$ and $n_{TRT}^{outliers} < 0.9n$
  - Case 2: $|\eta| \leq 0.1$ or $|\eta| \geq 1.9$. If $n > 5$, then require $n_{TRT}^{outliers} < 0.9n$.

Finally, we require that the muon be isolated as per the mini-isolation requirement $MI_{10} < 0.05$, as well as lie outside a $\Delta R \leq 0.4$ of any selected small R jets. Any muons passing all of these criteria are included in the H_{T} calculation. Figure 11.3 shows the number of selected muons as well as muon p_{T} in the pre-top-tag region as defined in a later section for several background MC samples as well as two signal samples.

[5] Requires a pixel b-layer hit on the muon EXCEPT where the extrapolated muon track passed an un-instrumented or dead area of the b-layer

11.2 Event Pre-selection

11.2.1 Data Quality

To ensure quality object reconstruction through the 2012 data, we only consider events are only considered if they are contained in a pre-defined Good Runs List (GRL) as provided by the Good Runs List Generator. The GRL used for this analysis is,

- data12_8TeV.periodAllYear_DetStatus-v61-pro14-02_DQDefects-00-01-00 _PHYS_StandardGRL_All_Good.xml

In addition to the GRL requirement, events are rejected if they were flagged as containing any Tile Calorimeter detector failures (`tileError==2`), are incomplete for any reason (`(coreFlags&0x40000) != 0`), or contain any Liquid Argon (LAr) noise bursts (`larError>1`).

11.2.2 Non-collision background rejection and vertex selection

Each pre-selected event is required to contain at least one good vertex, where a good vertex is defined as having at least 5 associated tracks with $p_{\mathrm{T}} > 400$ MeV each. Additionally, each vertex candidate is required to be of type `PriVtx` or of type `PileUp`. The candidate vertex with the highest scalar sum of track p_{T}^2 is considered the primary vertex of the event. The number of vertices passing these requirements are used as an input to several event level corrections as the number of primary vertices (N_{PV}).

11.2.3 Jet and missing transverse energy event quality

In some events, reconstructed jets are not the result of actual energy deposits in the calorimeters. That is, fake jets are the result of electronic calorimeter spikes. To protect against this, events are vetoed if they contain any jet with $p_{\mathrm{T}} > 20$ GeV after the calibration described below that is flagged as LooseBadMinus that is described in detail in [5].

11.3 Discriminating Variable Definitions

11.3.1 H_{T}

H_{T} is defined as the scalar sum of the transverse momentum of the selected anti-k_t R=0.4 b-tagged and un-tagged jets. This quantity is used as the final cut in our analysis. Sample distributions are shown in Fig. 11.4. Electrons are not included in this sum because their energy is already included in our selected jets.

$$H_{\mathrm{T}} = \sum p_{T,jet}^{sel} + \sum p_{T,b-jet}^{sel} + \sum p_{T,\mu}^{sel} \tag{11.7}$$

11.3.2 Isolation of b-tagged jets

A b-tagged jet is defined as isolated if the ΔR between it and the closest top-tagged or top-like fat jet is greater than 1.0. In boosted $t\bar{t}$ events, we might expect any b-tagged jet to be contained within the top-tagged jet or in this case, either the top-tagged jet or any other fat-jet that did not pass the top-tagging criteria that originated

from a top-quark decay. Our signal, however, has at least four b-hadrons in the final state, all of which come from decaying tops. Therefore, there is a greater probability to find an isolated b-tagged jet in signal events than in SM events, as shown in Fig. 11.5. We will use the notation $IsoB$ for events that contain at least one isolated b-tagged jet, while for events that do not contain any isolated b-tagged jets we will use the notation $NoIsoB$.

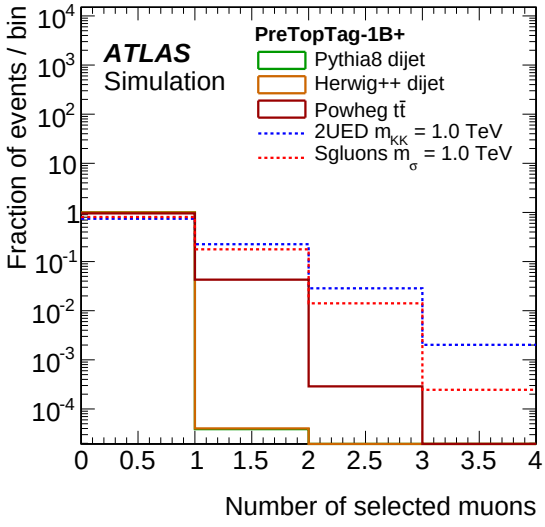

(a)

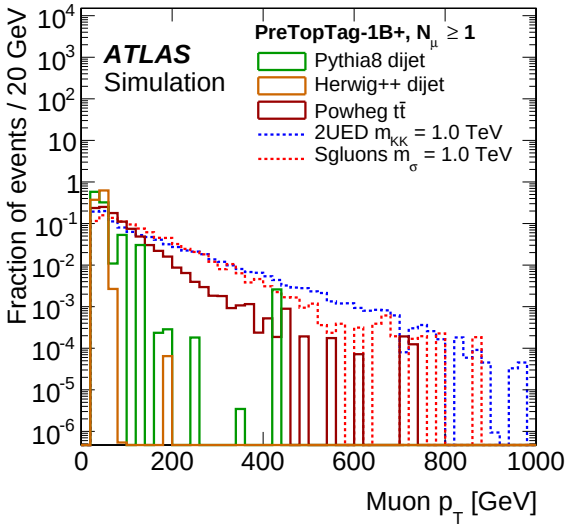

(b)

Figure 11.3: Distribution of the number of selected muons in 11.3(a) using the above criteria as well as the p_{T} of the leading selected muons 11.3(b) in events containing at least one muon for di-jet, $t\bar{t}$ as well as two signal samples. Both sets of distributions are normalized to unity.

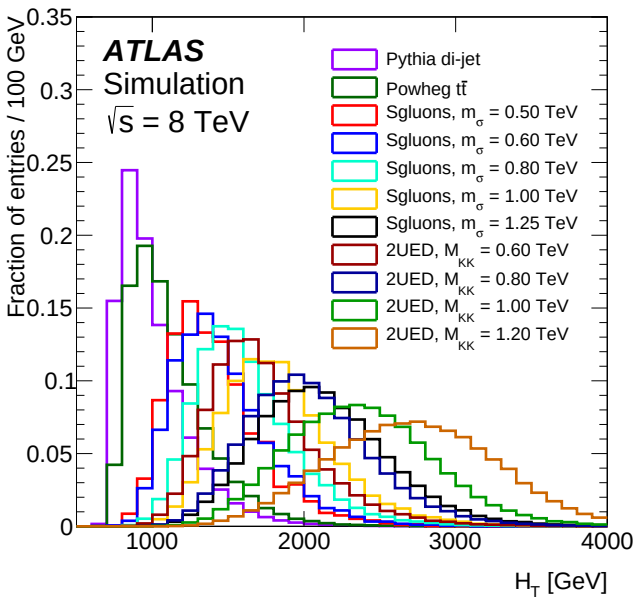

Figure 11.4: H_{T} distributions for Pythia di-jet and $t\bar{t}$ background MC as well as 2UED-RPP and scalar gluon signal. All distributions are normalized to unity.

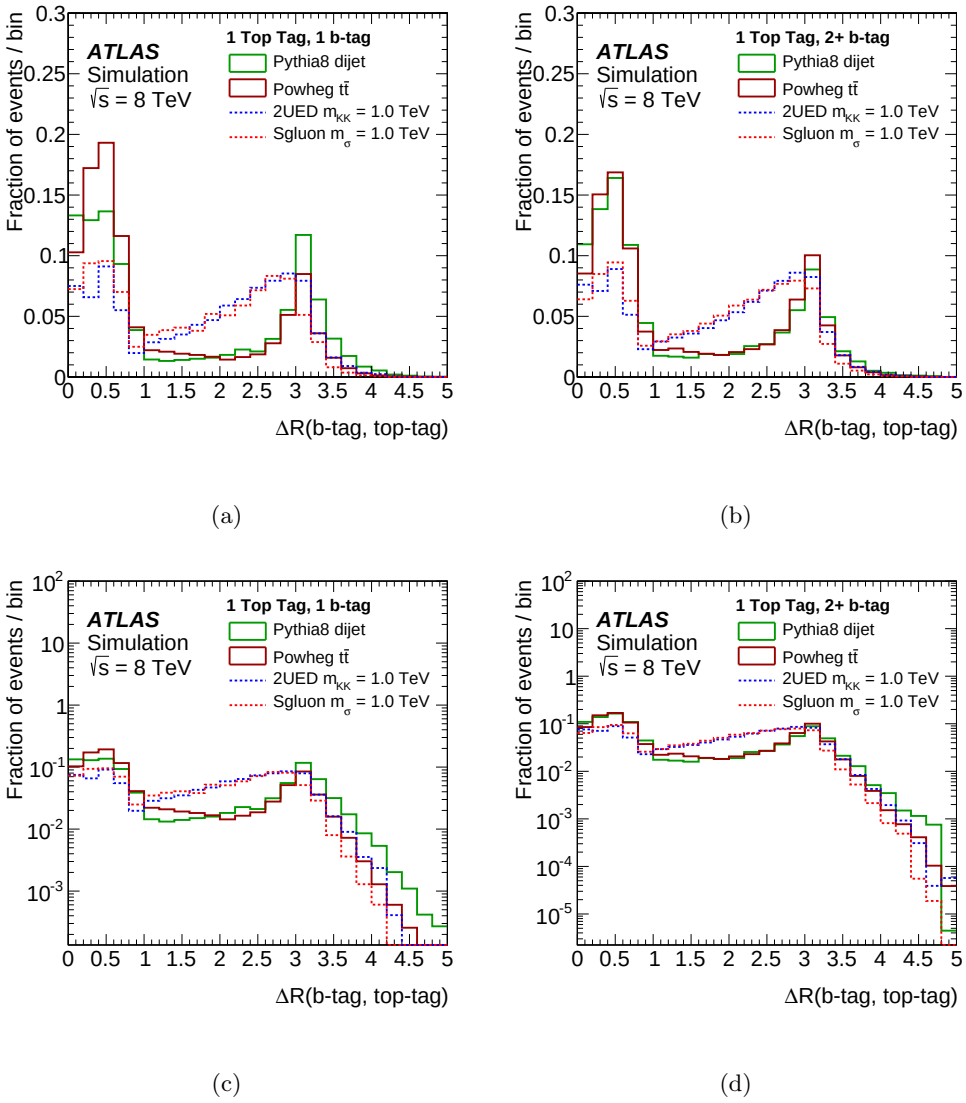

Figure 11.5: Distributions of the distance ΔR between a b-tagged jet and the nearest top-tagged jet in events with exactly one top-tagged jet. Figs. 11.5(a) and 11.5(c) show the distributions for events with exactly one b-tagged jet, where Figs. 11.5(b) and 11.5(d) show the distributions for events with at least two b-tagged jets. Di-jet and, $t\bar{t}$ as well as two signal MC points are shown. All distributions normalized to unity for shape comparison.

Chapter 12

Background Estimation

We expect our largest backgrounds in this analysis to be from top-pair production as well as high mass di-jet QCD events. We will show in subsequent sections that the $t\bar{t}$ MC provides a reliable prediction using a top-enriched control region. Additionally, we will show that while the QCD di-jet MC provides a reliable prediction of kinematic shapes of key distributions, the prediction for the absolute number of data events is not reliably reproduced. For this reason, we have chosen to use a combination of the $t\bar{t}$ MC along with the ABCD background estimation method that is described below.

12.1 ABCD Background Estimation Method

In the absence of reliable Monte Carlo predictions for any or all backgrounds, it is necessary to use a data driven method for estimating the Standard Model contribution to background events in the signal region. The ABCD method relies on the premise that

there exists two uncorrelated variables in the analysis. Essentially, the plane defined by those two variables can be split into four quadrants, namely A, B, C and D, as shown in Figure 12.1. For this analysis, the two uncorrelated variables used are the H_{T} and the number of b-tagged jets in the event. While H_{T} is a continuous variable, the number of b-tagged jets is separated into two bins: exactly one b-tagged jet and two or more b-tagged jets.

These two variables were chosen to isolate our signal in region D where there are at least two b-tagged jets in events with very large H_{T}. The number of events in region D can be predicted using the number of events in regions A, B and C, assuming that there is little correlation between H_{T} and the number of b-tagged jets. That is, in events with exactly one b-tagged jet, there is no a-priori physics reason why there would be more H_{T} than in events with at least two b-tagged jets.

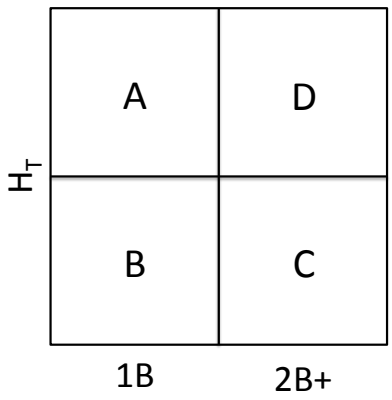

Figure 12.1: Graphical depiction of the four regions used in the ABCD method.

Under the assumption of little to no correlation between the H_{T} and the num-

ber of b-tagged jets and the assumption that regions A, B and C are background dominated regions (non-signal like), we can estimate the number of background events expected in region D. The fraction of events N_A/N_B should be roughly equal to the fraction of events N_D/N_C. Using this, we can estimate that,

$$N_D \approx \frac{N_A N_C}{N_B}. \tag{12.1}$$

Since we intend to use a combination of this method as well as Monte Carlo predictions for the $t\bar{t}$ background, we must first subtract out the $t\bar{t}$ contributions from regions A, B and C to estimate the portion of the background not modeled by the $t\bar{t}$ Monte Carlo (we chose to call it the multi-jet background). This modified prediction is shown below. The resulting prediction for the number of background events in region D is then $N_D^{multi-jet} + N_D^{t\bar{t}}$.

$$N_D^{multi-jet} \approx \frac{(N_A^{data} - N_A^{t\bar{t}})(N_C^{data} - N_C^{t\bar{t}})}{(N_B^{data} - N_B^{t\bar{t}})}. \tag{12.2}$$

In addition to using the ABCD method for predicting the number of background events in the signal regions, we will combine it with what is termed the "template" method for predicting the shape of important distributions in the signal region. The template method also relies on the assumption that for some distribution X that there is little to no correlation between X and the number of b-tagged jets. That is, the shape of distribution X in events with exactly one b-tagged jet is approximately the

same as the shape of X in events with at least two b-tagged jets. This assumption is valid for an events H_{T} as well as top-jet and top-like-jet kinematics (p_{T}, η, ϕ and mass).

Once we have a template distribution for the multi-jet background taken from the one b-tagged events (taken from the distribution resulting from the difference between data and the $t\bar{t}$ MC distributions), we need to scale it to the number of predicted events in the 2+ b-tagged bin. This scale factor is obtained by first calculating $N_D^{multi-jet}$ and then adding it to $(N_C^{data} - N_C^{t\bar{t}})$. The template distribution is then scaled such that the integral of the distribution is equivalent to $N_D^{multi-jet} + (N_C^{data} - N_C^{t\bar{t}})$.

Chapter 13

Control and Signal Region Definitions

This section defines the various control regions that are used for analysis validation as well as background estimation and our signal region. In particular, we describe the pre-selection, $t\bar{t}$ validation, ABCD validation as well as background estimation control regions. Table 13.1 summarize the signal and control regions.

13.1 Two+ top-tag Signal Region

Our first signal region requires at least two top-tagged fat jets, at least two b-tagged jets and at least one of those b-tagged jets must be isolated from all of the top-tagged jets. Additionally, since 4-top signal events contain very large H_{T}, we require $H_{\mathrm{T}} \geq 2.00$ TeV for the low H_{T} region and $H_{\mathrm{T}} \geq 2.25$ TeV for the high H_{T} region to suppress any additional backgrounds. The two H_{T} regions were chosen to potentially gain sensitivity to signal points with both low mass (e.g scalar gluon and Contact Interactions) and high mass initial states (e.g high mass 2UED-RPP). The selection

Region	Number of top-tagged jets	Number of b-tagged jets	Number of Iso. b-tagged jets	H_{T}
Pre-top-tag	N/A	1+	N/A	Inclusive
$CR-1T+TLFJ$	1	$1,2+$	$0,1+$	Inclusive
$CR-2T-1B^{NoIsoB}_{H_{\mathrm{T}}^{+}}$ (A)	≥ 2	1	0	≥ 2.00 (2.25) TeV
$CR-2T-1B^{NoIsoB}_{H_{\mathrm{T}}^{-}}$ (B)	≥ 2	1	0	< 2.00 (2.25) TeV
$CR-2T-2B+^{NoIsoB}_{H_{\mathrm{T}}^{-}}$ (C)	≥ 2	2+	0	< 2.00 (2.25) TeV
$CR-2T-2B+^{NoIsoB}_{H_{\mathrm{T}}^{+}}$ (D)	≥ 2	2+	0	≥ 2.00 (2.25) TeV
$CR-2T-1B^{IsoB}_{H_{\mathrm{T}}^{+}}$ (A)	≥ 2	1	1+	≥ 2.00 (2.25) TeV
$CR-2T-1B^{IsoB}_{H_{\mathrm{T}}^{-}}$ (B)	≥ 2	1	1+	< 2.00 (2.25) TeV
$CR-2T-2B+^{IsoB}_{H_{\mathrm{T}}^{-}}$ (C)	≥ 2	2+	1+	< 2.00 (2.25) TeV
$SR-2T-2B+^{IsoB}_{H_{\mathrm{T}}^{+}}$ (D)	≥ 2	2+	1+	≥ 2.00 (2.25) TeV

Table 13.1: Definition of all of the signal and control regions for the two-top tagged signal region.

criteria for this region is listed below.

- ≥ 2 top-tagged jets
- ≥ 2 calibrated, b-tagged anti-k_T R=0.4 jets tagged using the 70% efficiency working point.
- ≥ 1 isolated b-tagged jets
- $H_{\mathrm{T}} \geq 2.00$ for the lowH_{T} region and $H_{\mathrm{T}} \geq 2.25$ TeV for the high-H_{T} region.

This region is labeled D, corresponding to the ABCD background estimation method described in Section 12. With this in mind, we will now discuss the various control regions.

13.2 Control Regions for estimating background in the signal region

The control regions responsible for estimating the background contributions in region D are,

A: Exactly one b-tagged jet, isolated from the top-tagged fat-jets.

$H_{\mathrm{T}} \geq 2.00$ (2.25) TeV.

B: Exactly one b-tagged jet, isolated from the top-tagged fat-jets.

$H_{\mathrm{T}} < 2.00$ (2.25) TeV.

C: At least two b-tagged jets, one of which must be isolated from the top-tagged fat-jets.

$H_{\mathrm{T}} < 2.00$ (2.25) TeV.

These are labeled A,B and C corresponding to the ABCD background estimation method described in Section 12.

13.3 Pre-top-tag control region

In order to make sure that our pre-selection, object corrections as well as substructure tagging variables are understood, we define a pre-top-tag control region where we can compare data to Monte Carlo predictions. The selection criteria are:

- ≥ 2 calibrated fat-jets with $p_{\mathrm{T}} > 350$ GeV

- ≥ 1 calibrated, b-tagged anti-k_T R=0.4 jets tagged using the 70% efficiency working point.

The goal of looking in this CR is to understand the background contributions from both QCD di-jet events and $t\bar{t}$ as well as to validate our pre-selection criteria. Since we do not expect the QCD MC to have perfect scale factors, we scale the QCD MC to the difference between the number of data events and the number of simulated $t\bar{t}$ events for several $t\bar{t}$ MC samples. More concretely,

$$f_{scale}^{QCD} = \frac{n^{data} - n^{t\bar{t}}}{n^{QCD}}. \tag{13.1}$$

Scale factors for the various combinations of $t\bar{t}$ + QCD di-jet MC are shown on each validation plot. The four most important quantities to look at in this region are the fat-jet p_{T} as well as the three sub-structure variables used for top-tagging. These are shown in Figures 13.2 (a)-(c) and Figures 13.4 (a)-(c) comparing predictions using the Pythia 8 di-jet and Powheg $t\bar{t}$ MC and similarly in Figures 13.6 (a)-(c) and Figures 13.8 (a)-(c)using Herwig++ di-jet and Powheg $t\bar{t}$. In addition to the di-jet and $t\bar{t}$ distributions, several other backgrounds are shown. The leading and sub-leading fat-jet distributions are shown. Additional validation plots are available in the appendix.

Overall, there is good agreement between the shapes of the di-jet distributions and the data. Pythia8 describes the substructure variables τ_{32} and τ_{21} more accurately than Herwig++, while Herwig++ describes $\sqrt{d_{12}}$ more accurately than Pythia8. After subtracting the $t\bar{t}$ MC, the Pythia8 MC had an average scale factor of around 0.84,

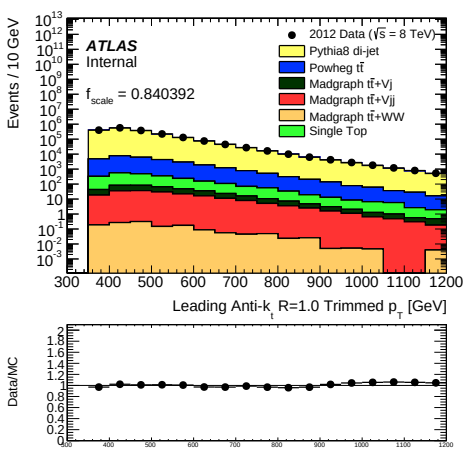

(a)

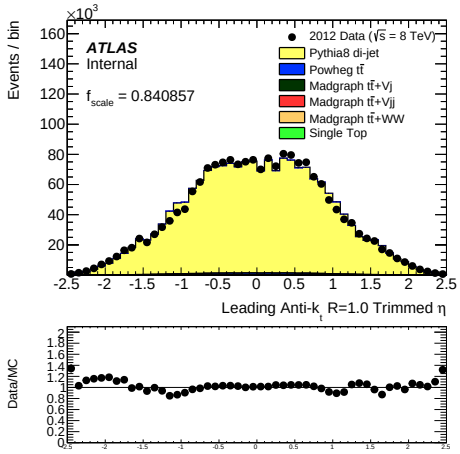

(b)

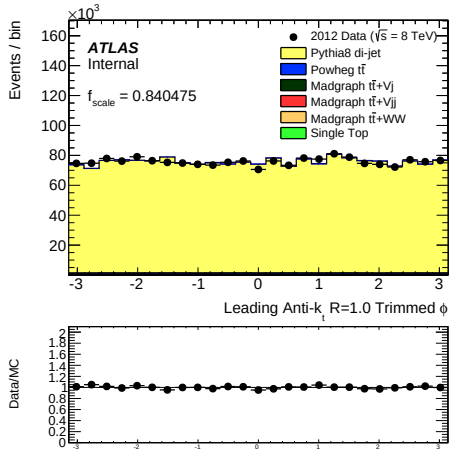

(c)

Figure 13.1: MC and data distributions of the leading fat-jet p_{T}, η, ϕ in the Pre-top-tag control region. The Pythia 8 QCD di-jet distributions are scaled to the difference between data and the Powheg $t\bar{t}$ MC (the scale factor is shown on the plot). Additional backgrounds are shown for reference but not subtracted.

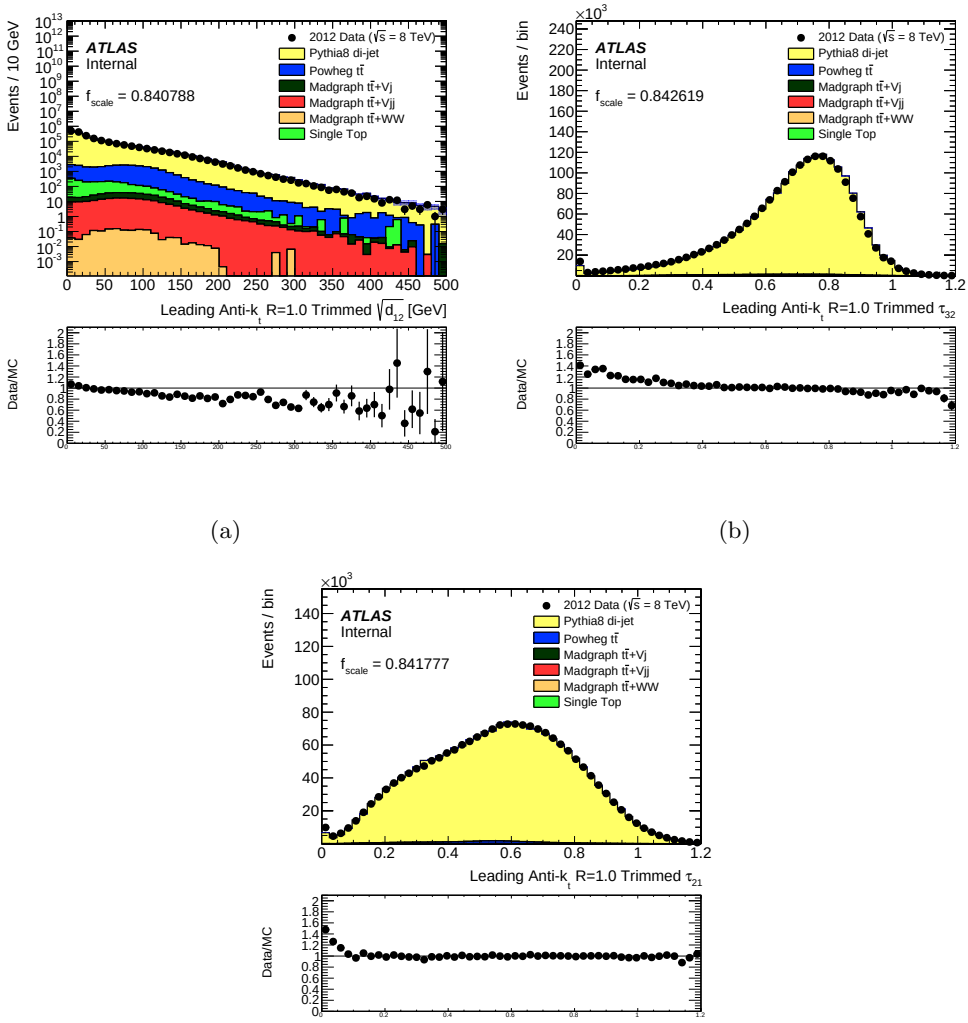

Figure 13.2: MC and data distributions of the leading fat-jet $\sqrt{d_{12}}$, τ_{32} and τ_{21} in the Pre-top-tag control region. The Pythia 8 QCD di-jet distributions are scaled to the difference between data and the Powheg $t\bar{t}$ MC (the scale factor is shown on the plot). Additional backgrounds are shown for reference but not subtracted.

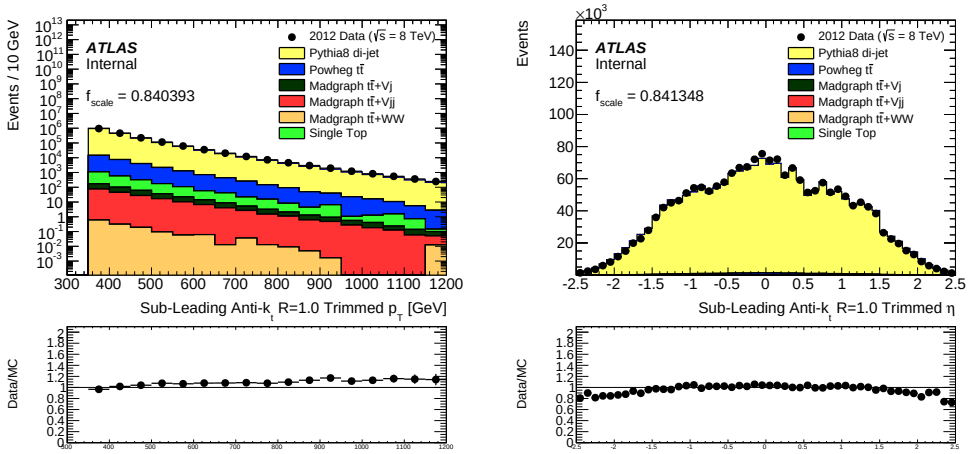

(a)

(b)

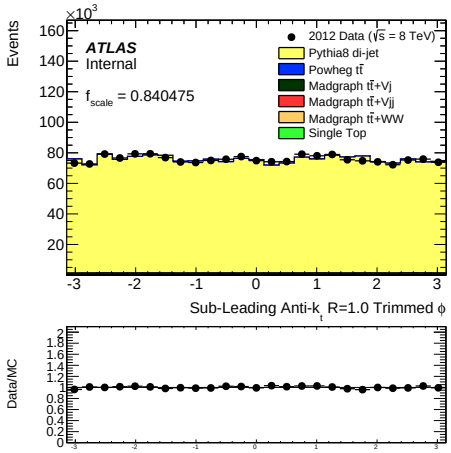

(c)

Figure 13.3: MC and data distributions of the sub-leading fat-jet p_{T}, η, ϕ in the Pre-top-tag control region.The Pythia 8 QCD di-jet distributions are scaled to the difference between data and the Powheg $t\bar{t}$ MC (the scale factor is shown on the plot). Additional backgrounds are shown for reference but not subtracted.

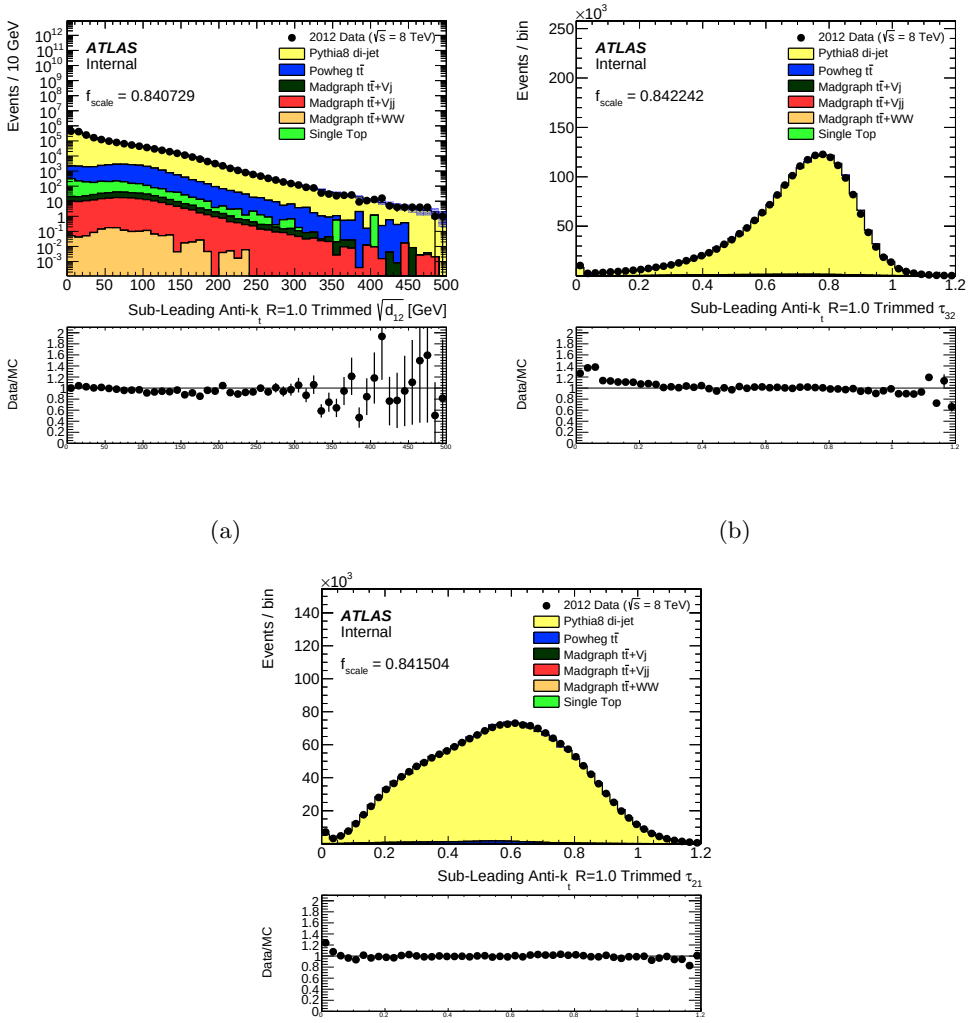

Figure 13.4: MC and data distributions of the sub-leading fat-jet $\sqrt{d_{12}}$, τ_{32} and τ_{21} in the Pre-top-tag control region.The Pythia 8 QCD di-jet distributions are scaled to the difference between data and the Powheg $t\bar{t}$ MC (the scale factor is shown on the plot). Additional backgrounds are shown for reference but not subtracted.

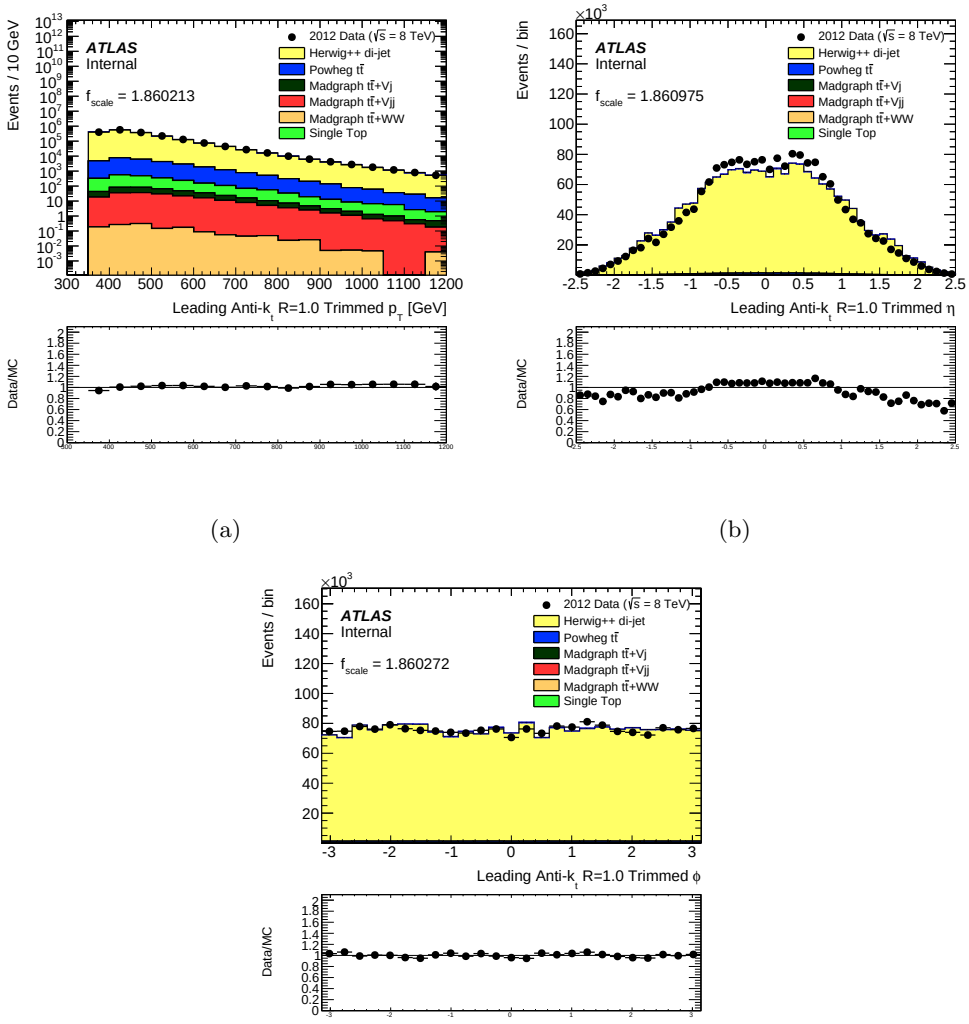

(a) (b)

(c)

Figure 13.5: MC and data distributions of the leading fat-jet p_{T}, η, ϕ in the Pre-top-tag control region. The Herwig++ QCD di-jet distributions are scaled to the difference between data and the Powheg $t\bar{t}$ MC (the scale factor is shown on the plot). Additional backgrounds are shown for reference but not subtracted.

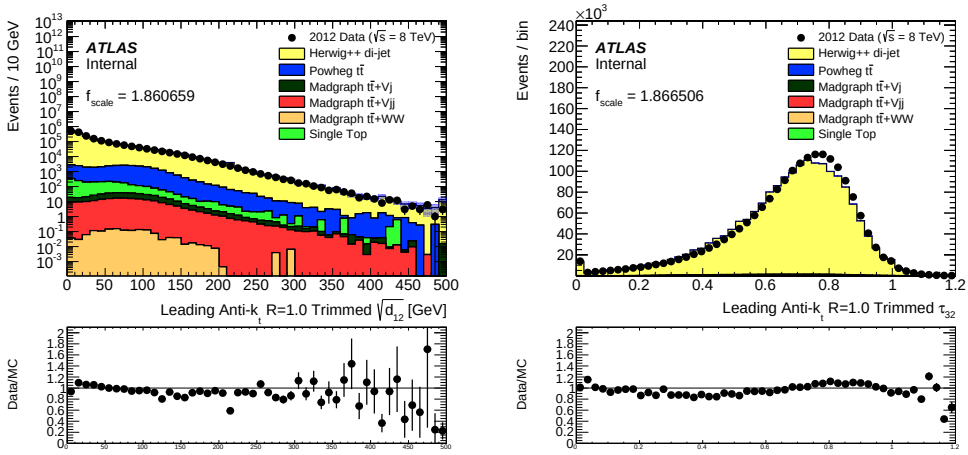

(a) (b)

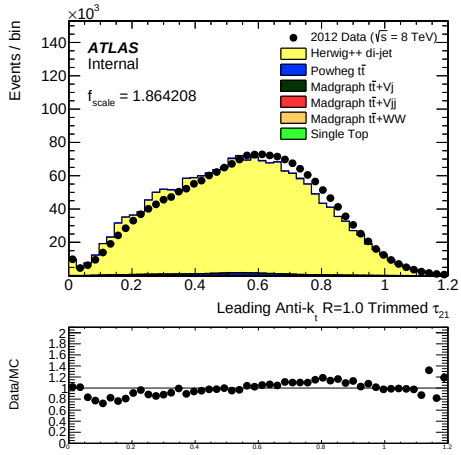

(c)

Figure 13.6: MC and data distributions of the leading fat-jet $\sqrt{d_{12}}$, τ_{32} and τ_{21} in the Pre-top-tag control region. The Herwig++ QCD di-jet distributions are scaled to the difference between data and the Powheg $t\bar{t}$ MC (the scale factor is shown on the plot). Additional backgrounds are shown for reference but not subtracted.

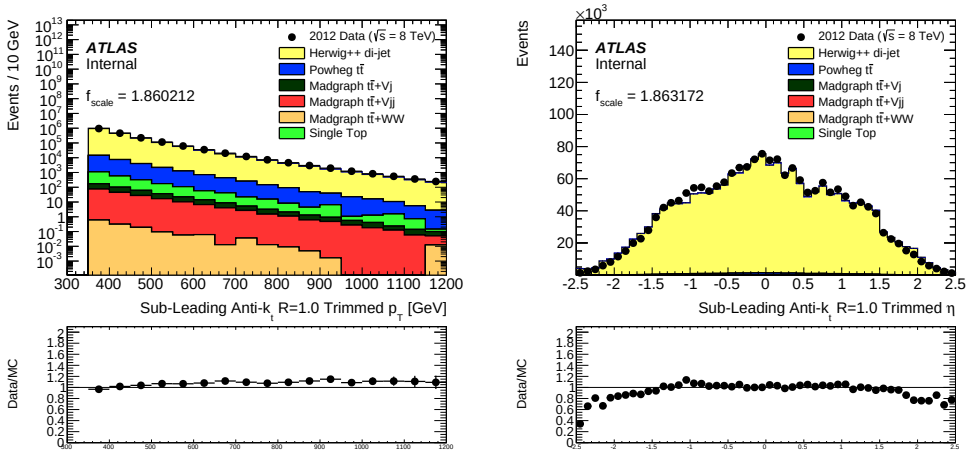

(a) (b)

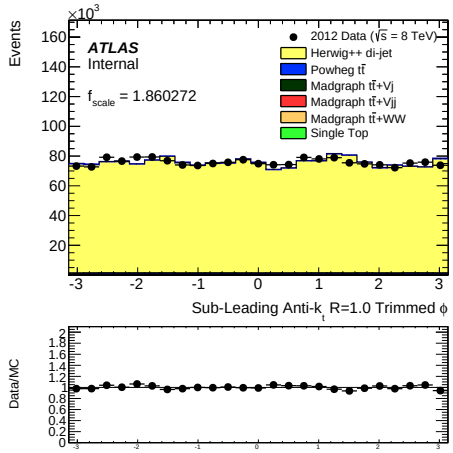

(c)

Figure 13.7: MC and data distributions of the sub-leading fat-jet p_{T}, η, ϕ in the Pre-top-tag control region.The Herwig++ QCD di-jet distributions are scaled to the difference between data and the Powheg $t\bar{t}$ MC (the scale factor is shown on the plot). Additional backgrounds are shown for reference but not subtracted.

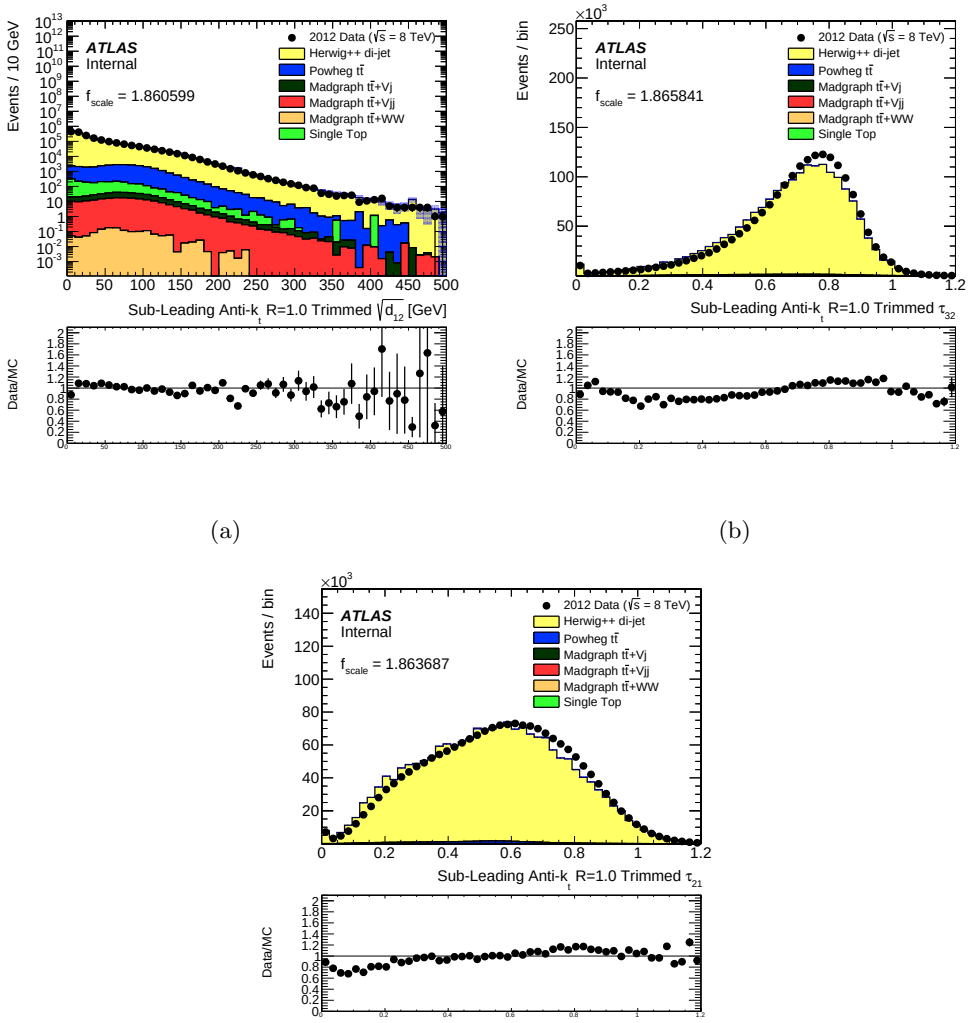

Figure 13.8: MC and data distributions of the sub-leading fat-jet $\sqrt{d_{12}}$, τ_{32} and τ_{21} in the Pre-top-tag control region.The Herwig++ QCD di-jet distributions are scaled to the difference between data and the Powheg $t\bar{t}$ MC (the scale factor is shown on the plot). Additional backgrounds are shown for reference but not subtracted.

while the Herwig++ had to be scaled by a factor of about 1.86. For this reason, we have decided to not use the QCD di-jet MC for anything more than to show understanding of important kinematic shapes.

Other quantities of interest in this region include the H_{T}, number of b-tagged jets, the number of un-b-tagged jets, as well as the number of selected muons, as shown in Figs. 13.9 (a)-(d) with comparisons between Pythia8 di-jet and Powheg $t\bar{t}$ and in Figs. 13.10 with comparisons between Herwig++ di-jet and Powheg $t\bar{t}$. We see relatively good agreement between data and MC for the H_{T} distribution after ≈ 1.0 TeV for both Pythia8 and Herwig++ . This is likely due to a difference in trigger efficiencies between data and MC. After that point, there is agreement within 20%.

There is very good agreement in the number of b-tagged jet between data and MC for Pythia8, as shown in Fig 13.10(b), however there is very poor agreement in the number of un-b-tagged jets, as shown in Fig. 13.10(c). For the Herwig++ samples, we see less agreement in the number of b-tagged jets while we see an improvement in the number of un-b-tagged jets. These disagreements could also account for the relatively large disagreement in the H_{T} distribution for $H_{\mathrm{T}} < 1$ TeV. If Pythia8 or Herwig++ contain a harder shower spectrum than the data, this could account for the larger number of low p_{T} jets.

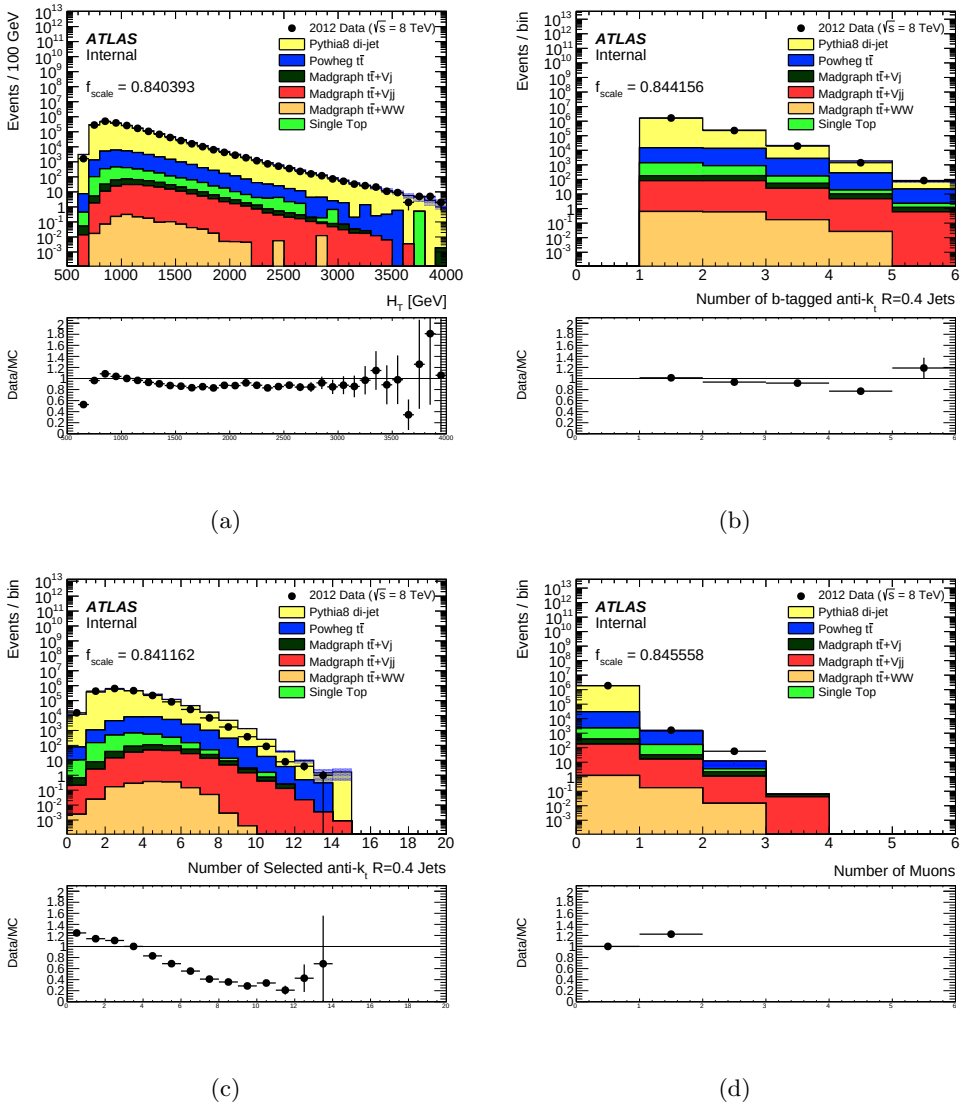

Figure 13.9: Data and MC distributions of the H_{T} in 13.10(a), the number of selected b-tagged jets in 13.10(b), the number of selected un-b-tagged jets in 13.10(c) and finally the number of selected muons in 13.10(d). Pythia8 di-jet and Powheg $t\bar{t}$ are used in making these plots. The QCD di-jet distributions are scaled to the difference between data and the $t\bar{t}$ MC (the scale factor is shown on the plot). Additional backgrounds are shown for reference but not subtracted.

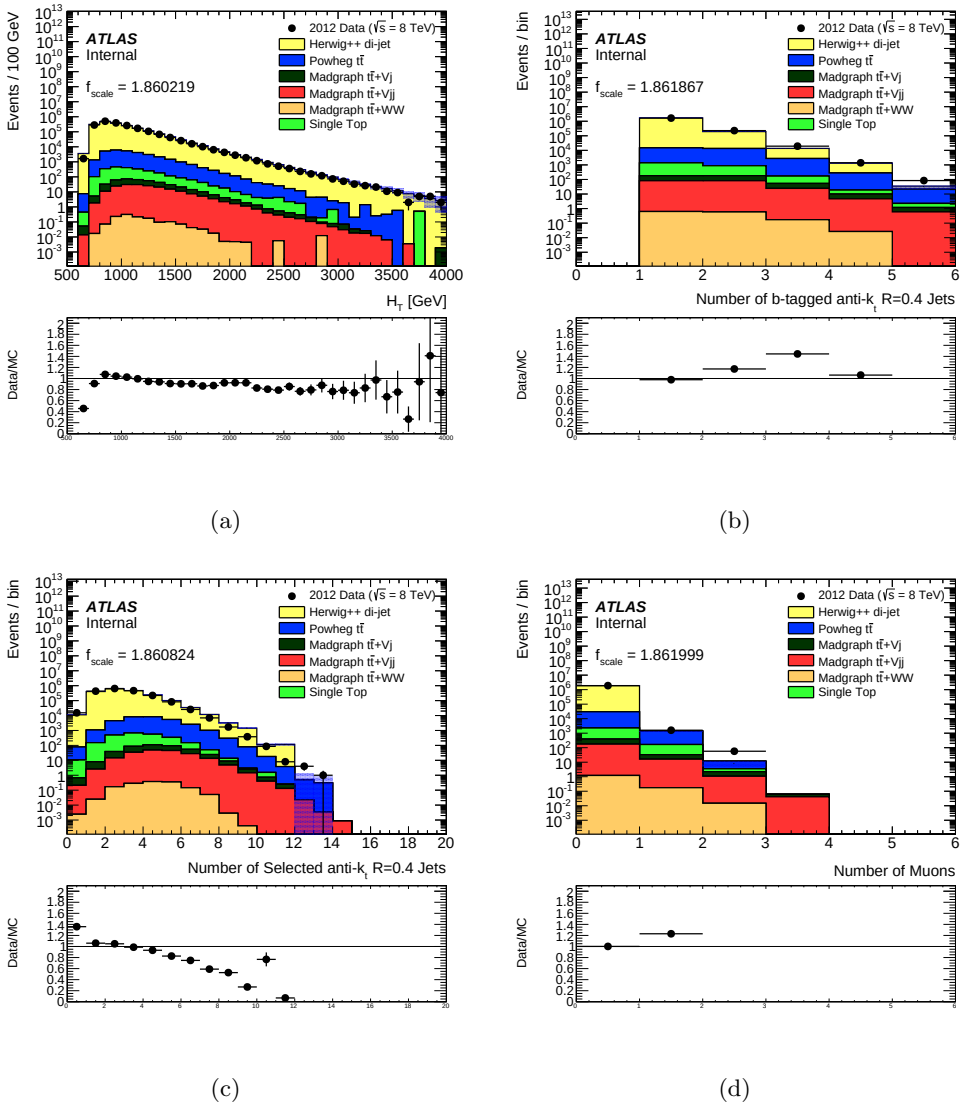

Figure 13.10: Data and MC distributions of the H_{T} in 13.10(a), the number of selected b-tagged jets in 13.10(b), the number of selected un-b-tagged jets in 13.10(c) and finally the number of selected muons in 13.10(d). Herwig++ di-jet and Powheg $t\bar{t}$ are used in making these plots. The QCD di-jet distributions are scaled to the difference between data and the $t\bar{t}$ MC (the scale factor is shown on the plot). Additional backgrounds are shown for reference but not subtracted.

13.4 One top-tag control region

??

This control region contains at most one top-tagged fat-jet and exactly one top-like fat-jet as defined in Section 11.1.4 as well as at least one b-tagged jet. We separate this region into two categories. The first being analogous to our isolated b-tagged signal region, where at least one of the b-tagged jets is isolated from both the top-tagged jet as well as the top-like fat-jet. The second region is orthogonal and does not contain any isolated b-tagged jets. Our signal region is not a subset of this region, therefore we can look all of the events in the data, inclusive in H_{T}, and validate our background prediction method. Additionally, this region is important because it gives us our first opportunity to introduce and study a new object that is crucial to our final selection; the isolated, or, non-overlapping, b-tagged jet that was defined in Section 11.3.2.

- 1 top-tagged jet
- $\geq$ 1 top-like fat jet
- $\geq$ 1 calibrated, b-tagged jets
- $\geq$ 1 isolated b-tagged jets (isolated from the top-tagged jet as well as the top-like fat jet).
- Inclusive in H_{T}

Since Pythia8 described the data more closely than Herwig++, from this point we will use the Pythia8 di-jet plus Powheg $t\bar{t}$ combination for validation in this region.

Additionally, we will demonstrate our data-driven background estimation method using only the $t\bar{t}$ MC and the data.

There is very good agreement between the data and MC in the top-jet p_{T} as shown in Fig. 13.11(a). However, there seems to be quite a bit of random disagreement in the top-jet η, ϕ and jet mass. It appears that this disagreement is just an artifact of being in a very particular region of kinematic phase space. There does seem to be general agreement between the shapes modulo some of the random bins. Analogous kinematic distributions are shown for the top-like fat-jet in Fig. 13.12.

What is more important to notice is the increased contribution from the $t\bar{t}$ background, which is about 20% (increased from 1.5% in the PreTopTag control region). If we numerically compare number of $t\bar{t}$ events to the number of events in data that contain exactly one b-tagged jet in this region, the $t\bar{t}$ accounts for 9.3% of the events. This is very comparable to the 2T-IsoB-1B region, where the $t\bar{t}$ accounts for 9.8% of the events as compared to data.

The H_{T} distribution in this control region is shown in Fig. **??** and Fig. **??** for events containing exactly one b-tagged jet and at least two b-tagged jets, respectively. There is relatively good agreement between the MC and the data with the exception of a couple of bins that are due to the QCD di-jet MC.

We would also like to use this region to begin to validate the ABCD+Template background estimation method. The first assertion that we need to verify is that there is little to no correlation between the number of b-tagged jets and the H_{T} in the data. There are two methods that we can use to verify this assertion. By looking at a two-

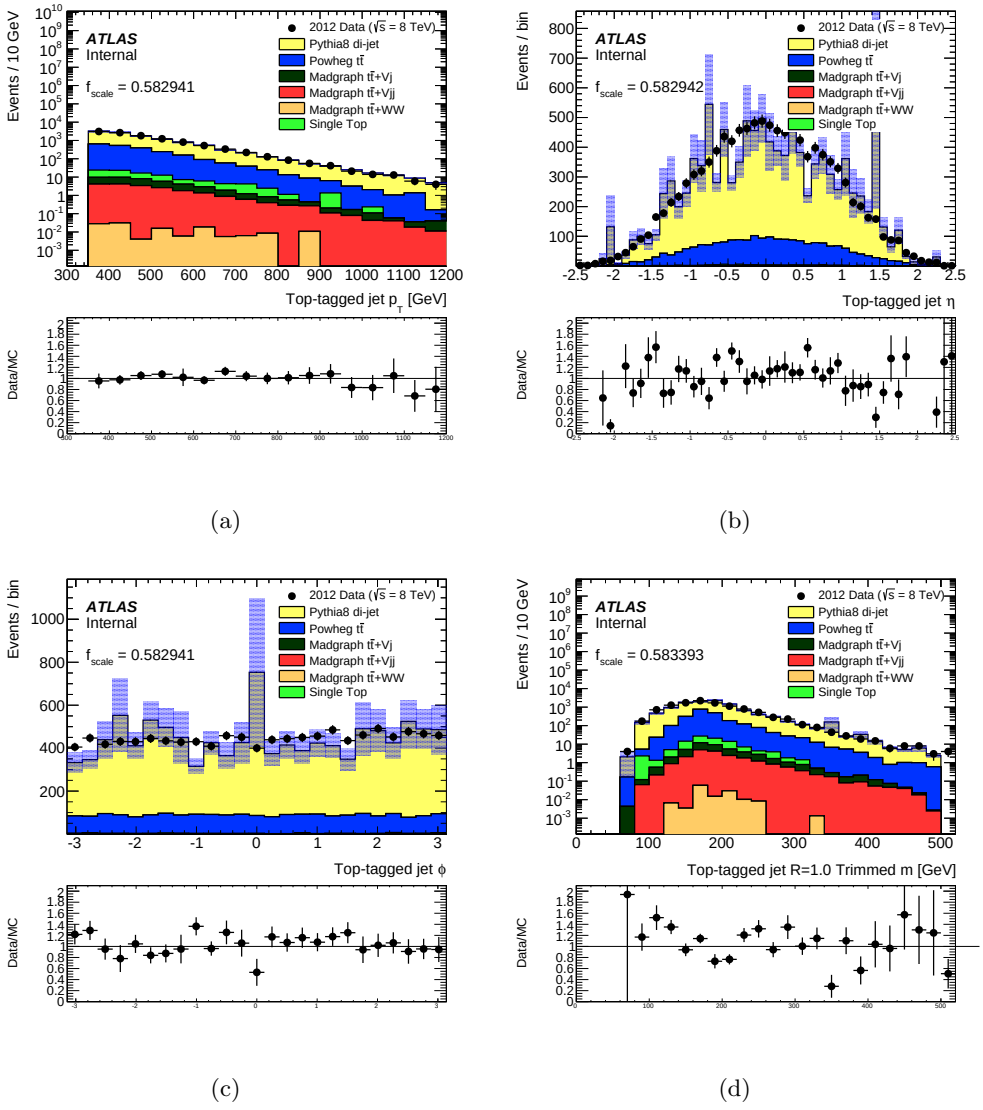

Figure 13.11: MC and data distributions of the top-tagged jet p_{T}, η, ϕ, and mass in the 1T-TLFJ control region. The Pythia8 QCD di-jet distributions are scaled to the difference between data and the Powheg $t\bar{t}$ MC (the scale factor is shown on the plot). Additional backgrounds are shown for comparison but not subtracted from the data.

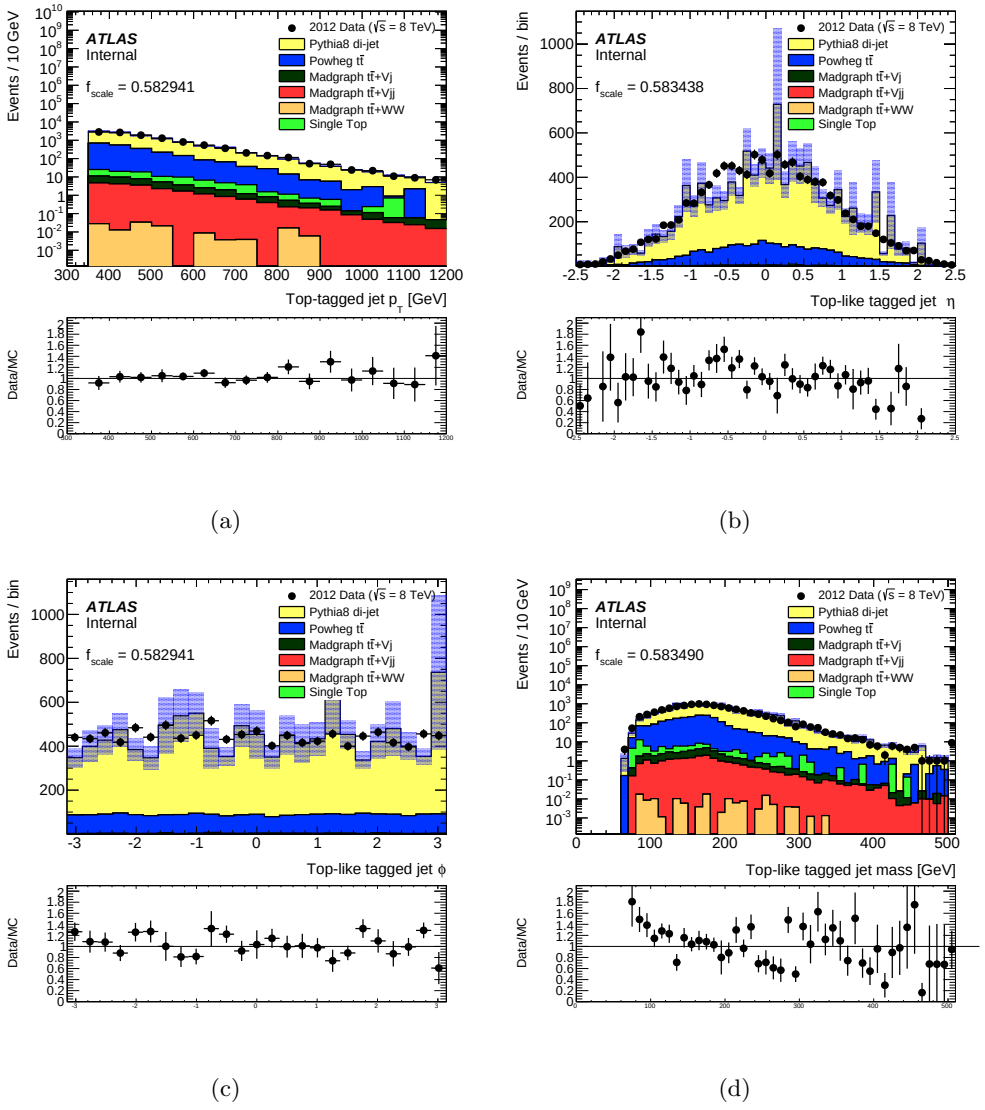

Figure 13.12: MC and data distributions of the top-like fat-jet p_{T}, η, ϕ, and mass in the 1T-TLFJ control region. The Pythia8 QCD di-jet distributions are scaled to the difference between data and the Powheg $t\bar{t}$ MC (the scale factor is shown on the plot). Additional backgrounds are shown for comparison but not subtracted from the data.

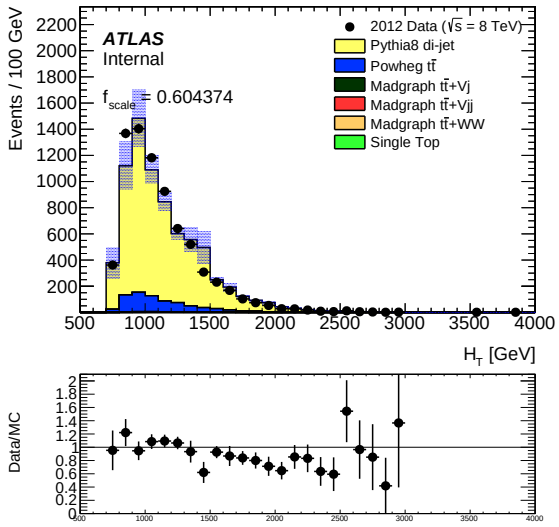

(a)

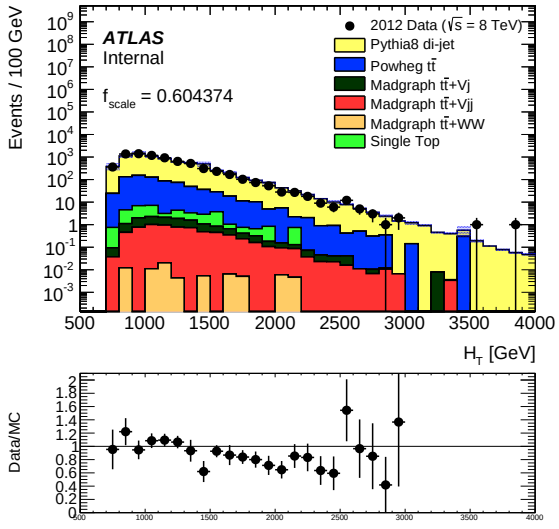

(b)

Figure 13.13: MC and data distributions of the H_{T} in events containing exactly one b-tagged jet in the 1T-TLFJ control region. The Pythia8 QCD di-jet distributions are scaled to the difference between data and the Powheg $t\bar{t}$ MC (the scale factor is shown on the plot). Additional backgrounds are shown for comparison but not subtracted from the data.

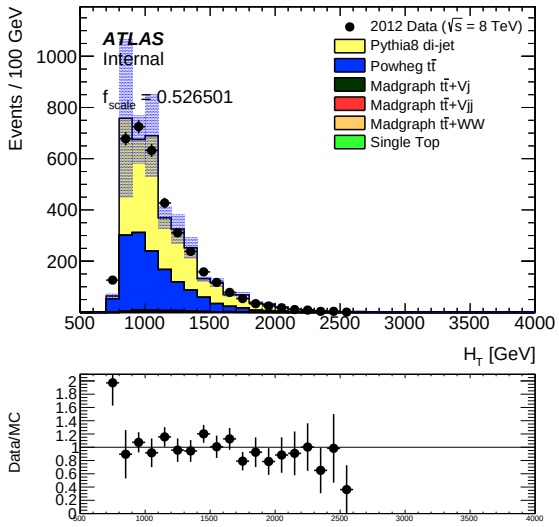

(a)

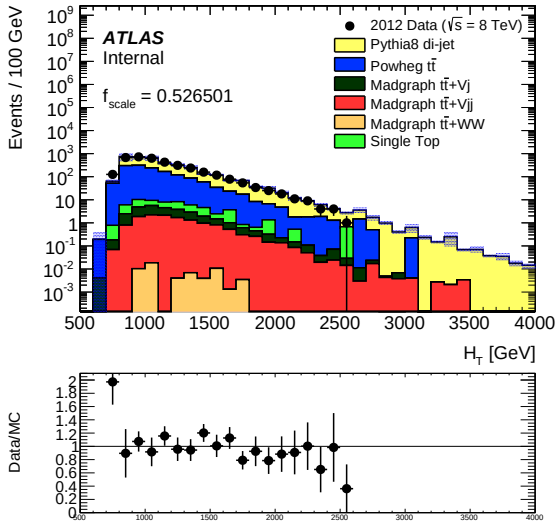

(b)

Figure 13.14: MC and data distributions of the H_{T} in events containing at least two b-tagged jets in the 1T-TLFJ control region. The Pythia8 QCD di-jet distributions are scaled to the difference between data and the Powheg $t\bar{t}$ MC (the scale factor is shown on the plot). Additional backgrounds are shown for comparison but not subtracted from the data.

dimensional histogram of the number of b-tagged jets and the H_{T} we can calculate the Pearson correlation coefficient (commonly called $\rho_{X,Y}$), which is defined formally as the covariance of the two variables of interest divided by the standard deviation of each variable. For this control region, the correlation coefficient is -0.0000123, indicating that there is no correlation between the two variables in this region. The second method we can use is by looking at a profile projection of the two-dimensional histogram and fitting a first degree polynomial to the resulting distribution. The resulting slope of the distribution is -0.193 ± 4.34 GeV/b-tagged jet, which is constant with zero. These numbers are summarized in Table 13.2 for the data as well as the Powheg $t\bar{t}$ and Pythia8 di-jet MC. There are slight opposite correlations in the MC, however since the data is a mixture of these background contributions, the correlations effectively cancel.

	$\rho_{N(b),H_{\mathrm{T}}}$	Profile Fit Slope [GeV/b-jet]	Fit χ^2
Powheg $t\bar{t}$	-0.0588	-21.1 ± 8.25	9.52
Pythia8 di-jet	0.0185	9.12 ± 4.85	40.9
Data	-0.0000123	-0.193 ± 4.35	2.90
Data-$t\bar{t}$	0.035497	19.17 ± 5.864	0.5106

Table 13.2: Correlation factor, profile fit slope and profile fit χ^2 between the H_{T} and the number of b-tagged jets in the 1T+TLFJ control region for data, Powheg $t\bar{t}$ and Pythia8 di-jet.

Table 13.6 shows the low H_{T} (2.0 TeV) while Table 13.4 shows the high H_{T} (2.25 TeV) event yields in this control region for the data, Powheg $t\bar{t}$ as well as the predicted multi-jet background. The measured number of data events for the low H_{T} selection is 72 ± 8.49 (stat), while the total predicted number of events form the Powheg

$t\bar{t}$ and multi-jet background is 66.1, well within the statistical uncertainty of the actual number of data events. For the high H_{T} selection, the total number of data events is 29 ± 5.38 with the total predicted number of background events using the data-driven is 32.4 which is also well within the statistical uncertainty.

	1T-FIsoB Control and Signal Regions			
MC Sample	A	B	C	D
Data	113 ± 10.63	7339 ± 85.67	3603 ± 60.02	47 ± 6.856
Powheg $t\bar{t}$	13.62 ± 2.068	757.4 ± 15.51	1426 ± 19.17	14.25 ± 1.981
Multi-jet	99.38 ± 12.7	6582 ± 101.2	2177 ± 79.2	32.87 ± 4.395
Total	113 ± 10.63	7339 ± 85.67	3603 ± 60.02	47.11 ± 4.821

Table 13.3: Data and backgrounds MC yields as well as the multi-jet prediction in the low H_{T} 1T-FIsoB regions. Only statistical uncertainties are shown.

	2T-FIsoB Control and Signal Regions			
MC Sample	A	B	C	D
Data	44 ± 6.633	7408 ± 86.07	3640 ± 60.33	10 ± 3.162
Powheg $t\bar{t}$	5.773 ± 1.356	765.2 ± 15.59	1434 ± 19.23	6.525 ± 1.39
Multi-jet	38.23 ± 7.989	6643 ± 101.7	2206 ± 79.56	12.69 ± 2.699
Total	44 ± 6.633	7408 ± 86.07	3640 ± 60.33	19.22 ± 3.036

Table 13.4: Data and backgrounds MC yields as well as the multi-jet prediction in the high H_{T} 2T-FIsoB regions. Only statistical uncertainties are shown.

Numerically, the ABCD method works well in this control region. Figure 13.16 demonstrates our ABCD+Template background estimation method for the H_{T} distribution in this control region. There is very good agreement between the total

	Control Region - 1T+TLFJ			
MC Sample	A	B	C	D
Powheg $t\bar{t}$	15.846	678.64	1586.9	22.038
Pythia8 di-jet	318.3	10422	4097.5	138.2
Total	334.2	11100.6	5684.4	160.2
Total Predicted	334.2	11100.6	5684.4	147.1

Table 13.5: Data and backgrounds MC yields as well as the multi-jet prediction in the 1T+TLFJ control region for the low H_{T} selection.

	Signal Region - 2T-IsoB			
MC Sample	A	B	C	D
Powheg $t\bar{t}$	0.87108	49.862	206.17	1.7417
Pythia8 di-jet	15.19	1202	584	9.85
Total	16.06	1251.8	790.2	11.6
Total Predicted	16.06	1251.8	790.2	9.12

Table 13.6: Data and backgrounds MC yields as well as the multi-jet prediction in the 1T+TLFJ control region for the low H_{T} selection.

resulting distribution and data. The single-top and $t\bar{t}+V$ backgrounds are also shown but not used in the final estimation. Contributions from those processes as well as any other multi-jet backgrounds. For comparison, one of our benchmark 2UED-RPP signal points with $\mathrm{m}_{KK} = 1.0$ GeV is also shown as the red-dashed line.

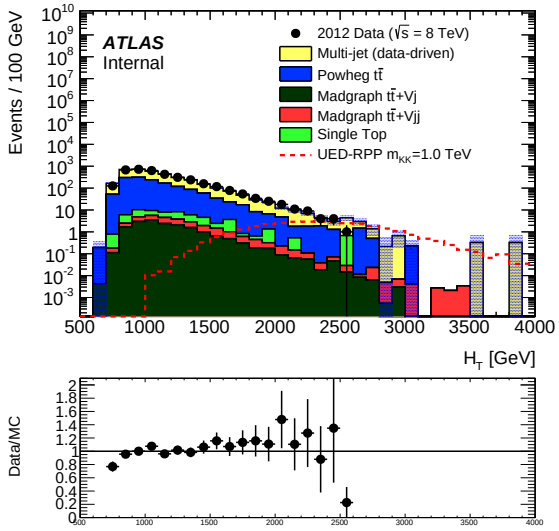

(a)

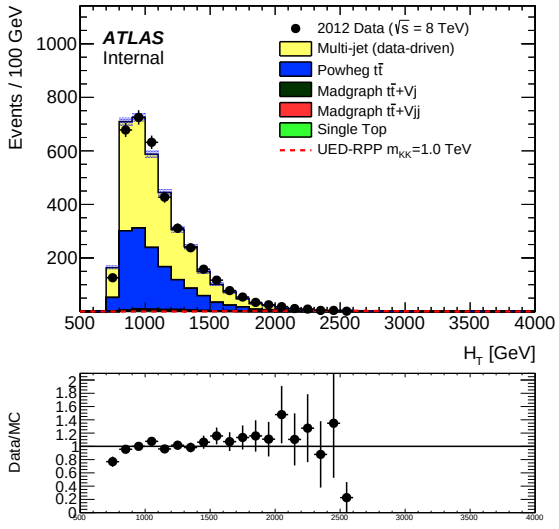

(b)

Figure 13.15: MC and data distributions of the H_{T}. The multi-jet distribution is taken from events containing exactly one b-tagged jet and scaled to the predicted number of events with at least two b-tagged jets. Additional backgrounds are shown for comparison but not subtracted from the data. The 2UED-RPP $\mathrm{m}_{KK} = 1.0$ TeV signal distribution is also shown.

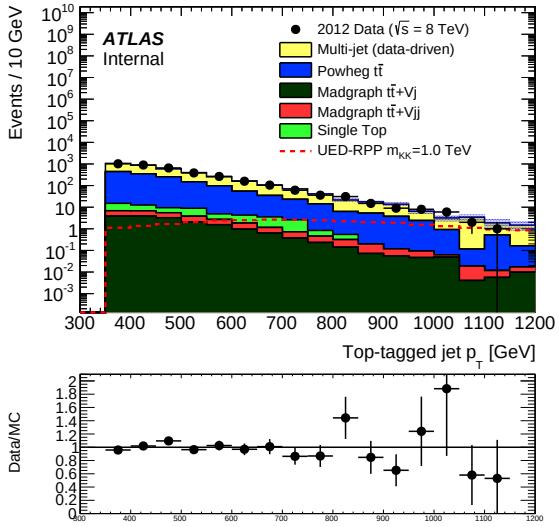

(a)

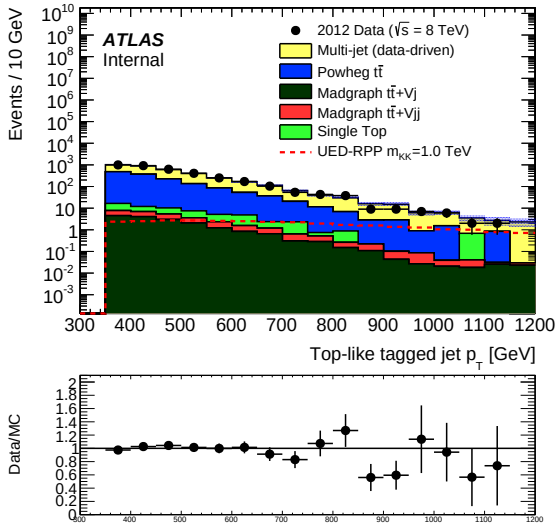

(b)

Figure 13.16: MC and data distributions of the top- and toplike- jet p_{T}. The multi-jet distribution is taken from events containing exactly one b-tagged jet and scaled to the predicted number of events with at least two b-tagged jets. Additional backgrounds are shown for comparison but not subtracted from the data. The 2UED-RPP $\mathrm{m}_{KK} = 1.0$ TeV signal distribution is also shown.

13.5 Two top-tag NoIsoB Control Region

The purpose of this region is twofold. It gives us an opportunity to test the ABCD method in a region that is composed of an ad-mixture of QCD di-jet and $t\bar{t}$ events. Additionally, events that contain at least 2 b-tagged jets are very enriched in $t\bar{t}$ events, thus giving us a way to validate our $t\bar{t}$ predictions and distribution shapes in this boosted regime. Selection criteria for this region are summarized below.

- ≥ 2 top-tagged jets
- ≥ 1 calibrated, b-tagged jets
- Exactly zero isolated b-tagged jets (all b-tagged jets lie within the $\eta - \phi$ plane of the top-tagged jets).
- Inclusive in H_{T}

Our validation plots for this region will again use only the Powheg $t\bar{t}$ and the Pythia8 di-jet MC samples. Other distributions are shown just for relative potential contributions that will be handled when we demonstrate our data-driven background estimation. We will separate these plots into events that contain exactly one b-tagged jet and those containing at least two b-tagged jets. The former events contain around 21% $t\bar{t}$ while the latter contain around 73% $t\bar{t}$.

For events containing exactly one b-tagged jet, we see in Fig. 13.17(a) relatively good agreement in the leading top-jet p_{T}. However, similar to the breakdown in agreement in the 1T-TLFJ control region for the η, ϕ and jet-mass distributions, the

di-jet MC appears to have particular bins that contain very large weights, resulting in data/MC overall disagreement.

The H_{T} and a new quantity, the di-top invariant mass, are shown in Fig. 13.19. There is good agreement between data and MC in the H_{T} for $H_{\mathrm{T}} > 1$ TeV, while there is relatively good agreement from the di-top invariant mass if we take into account that the di-jet MC is starting to not perform as well in this region of phase space. We will see when we have a more enriched $t\bar{t}$ sample coming from events containing at least two b-tagged jets that the data/MC agreement improves.

Figures 13.20(a)-13.20(d) show the top-jet kinematic distributions for the leading top-tagged jet in events containing at least two b-tagged jets. Similarly, Figures 13.21(a) - 13.21(a) show the same distributions for the sub-leading top-tagged jet. One can see right away that the predominant background at this point in the selection is indeed the $t\bar{t}$. To within statistical uncertainty, there is good agreement between data and MC for all of the kinematic variable for the majority of the ranges. In particular, we see very good agreement in the H_{T} and di-top invariant mass distributions (shown in Fig. 13.22) as well as the leading and sub-leading top-jet p_{T} distributions.

Analogous to the 1T-TLFJ region, we want to ultimately use this region to validate the ABCD+Template background estimation method. Table 13.7 shows the correlation coefficients for the data, $t\bar{t}$ and di-jet MC as well as the profile fit slope and the corresponding χ^2 for that fit. The correlation coefficients for the data and $t\bar{t}$ are consistent with very low, however non-zero correlation. This is reflected in the slope of the profile fit. What this indicates is that in this region, the efficiency for b-

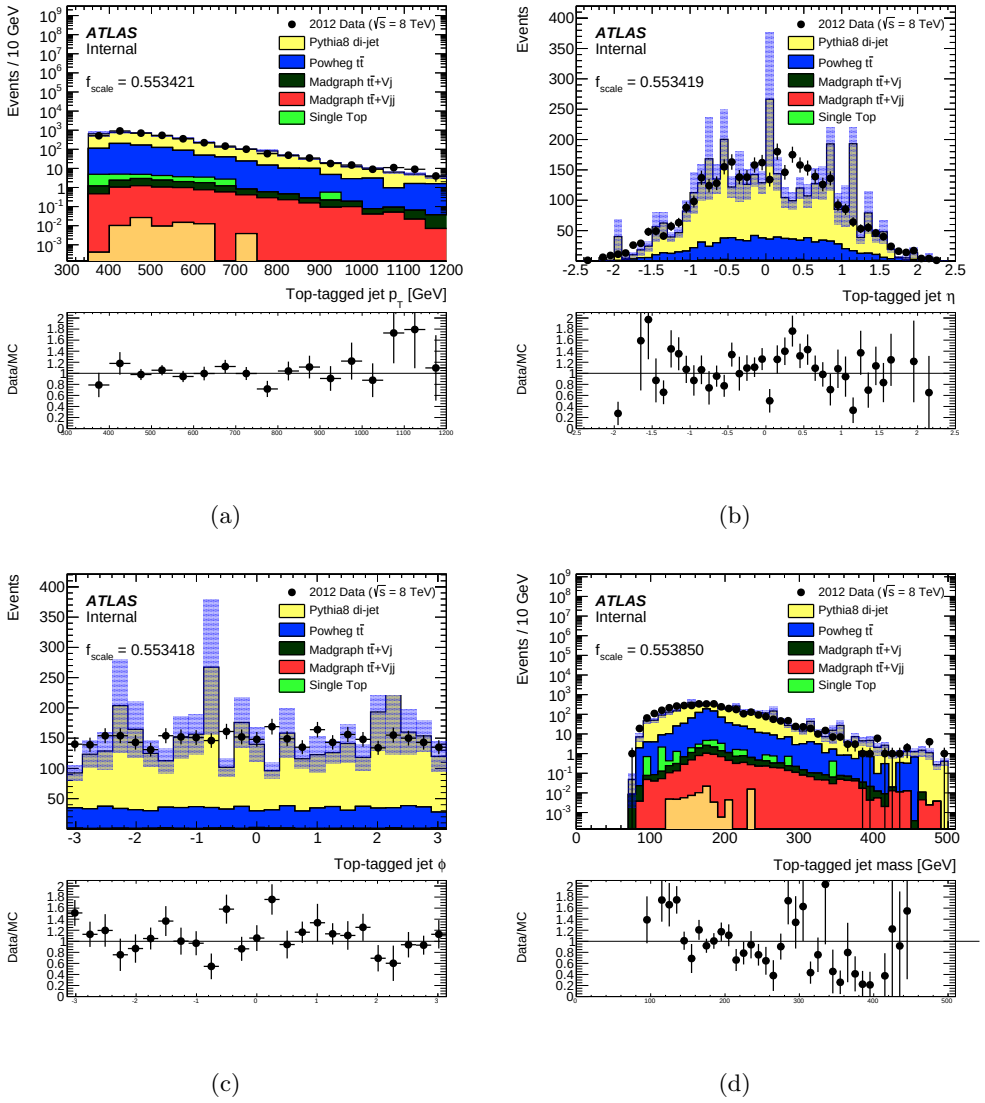

Figure 13.17: MC and data distributions of the leading top-tagged fat-jet p_{T}, η, ϕ, and mass in the 2T-NoIsoB control region in events with exactly one b-tagged jet. The Pythia8 QCD di-jet distributions are scaled to the difference between data and the Powheg $t\bar{t}$ MC (the scale factor is shown on the plot). Additional backgrounds are shown for comparison but not subtracted from the data. The shaded blue represents the total statistical uncertainty.

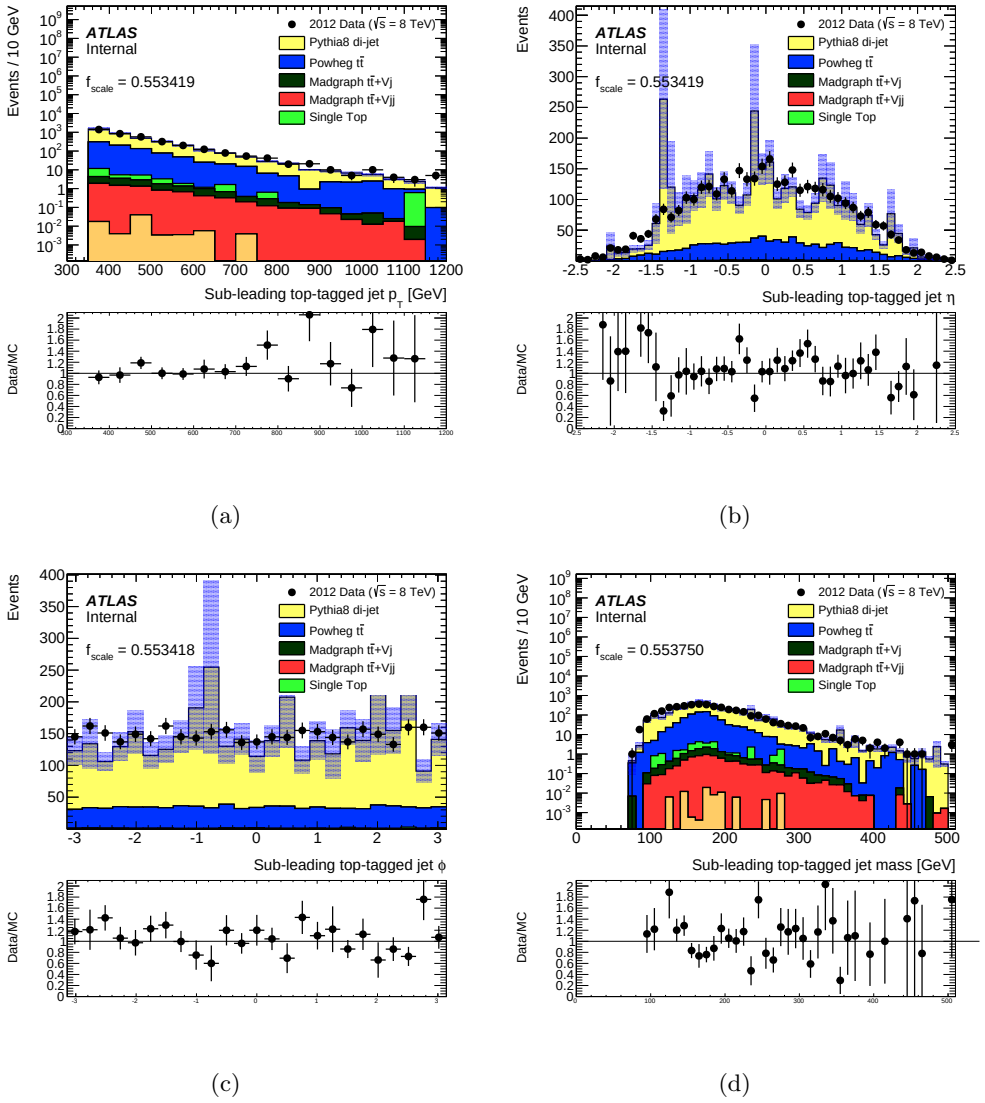

Figure 13.18: MC and data distributions of the sub-leading top-tagged fat-jet p_{T}, η, ϕ, and mass in the 2T-NoIsoB control region in events with exactly one b-tagged jet. The Pythia8 QCD di-jet distributions are scaled to the difference between data and the Powheg $t\bar{t}$ MC (the scale factor is shown on the plot). Additional backgrounds are shown for comparison but not subtracted from the data. The shaded blue represents the total statistical uncertainty.

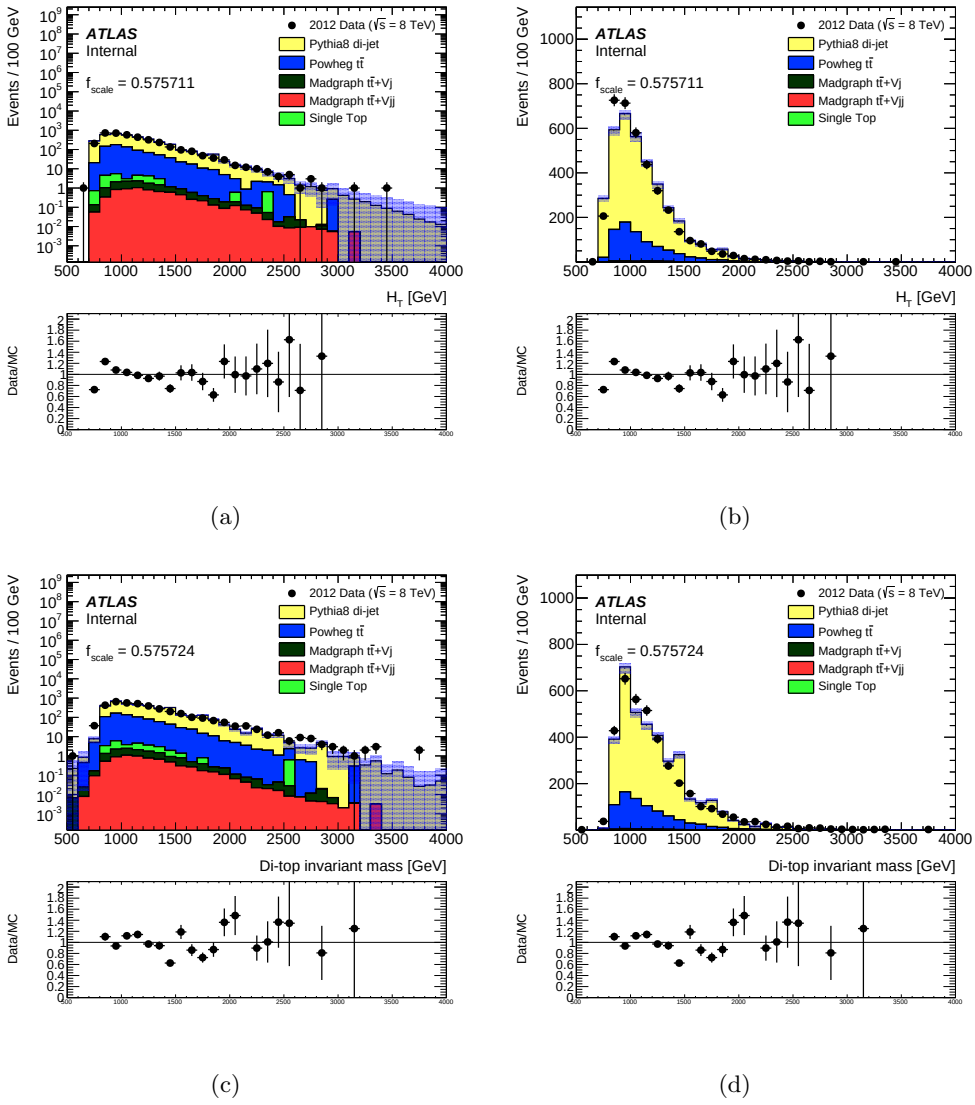

Figure 13.19: MC and data distributions of the H_{T} and di-top invariant mass in the 2T-NoIsoB control region in events with exactly one b-tagged jet. The Pythia8 QCD di-jet distributions are scaled to the difference between data and the Powheg $t\bar{t}$ MC (the scale factor is shown on the plot). Additional backgrounds are shown for comparison but not subtracted from the data.

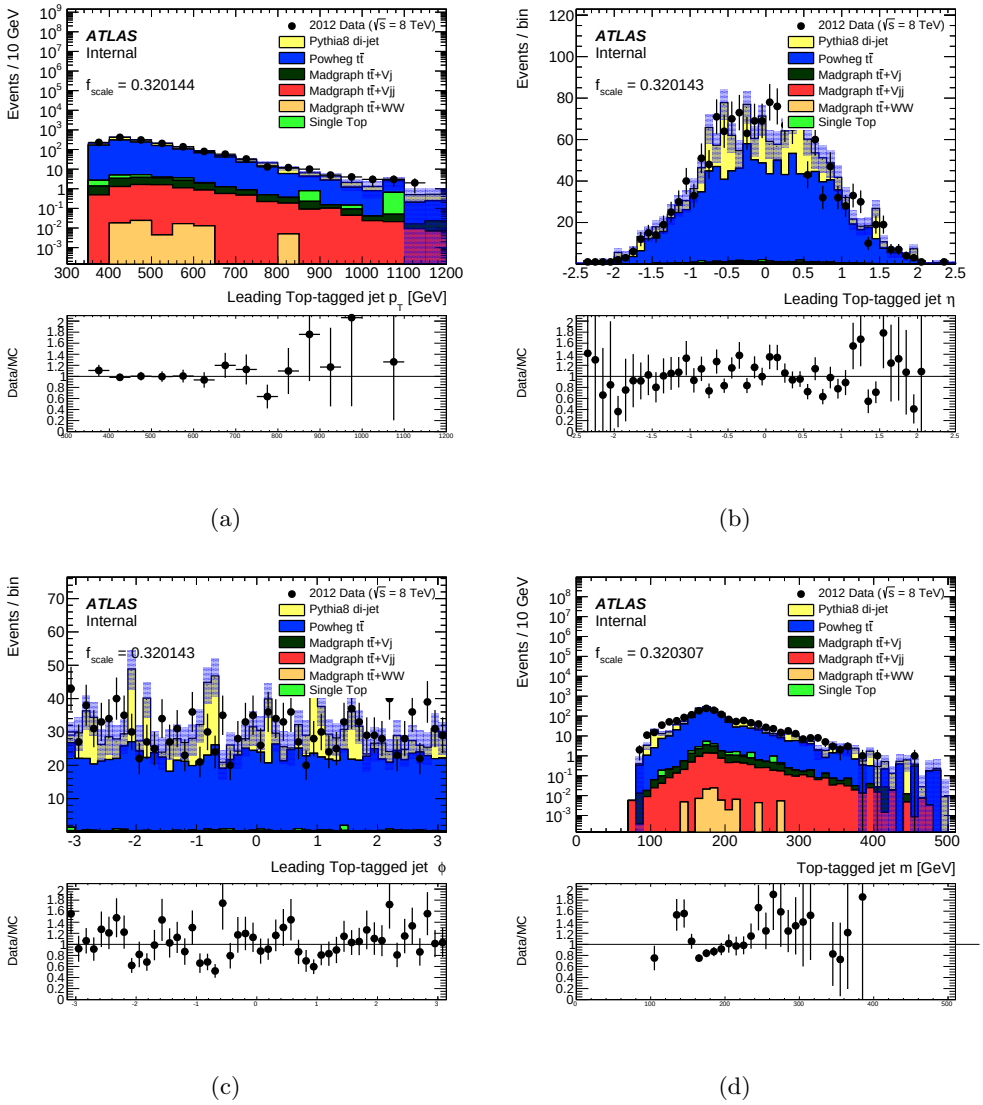

Figure 13.20: MC and data distributions of the leading top-tagged fat-jet p_{T}, η, ϕ, and mass in the 2T-NoIsoB control region in events with at least two b-tagged jets. The Pythia8 QCD di-jet distributions are scaled to the difference between data and the Powheg $t\bar{t}$ MC (the scale factor is shown on the plot). Additional backgrounds are shown for comparison but not subtracted from the data.

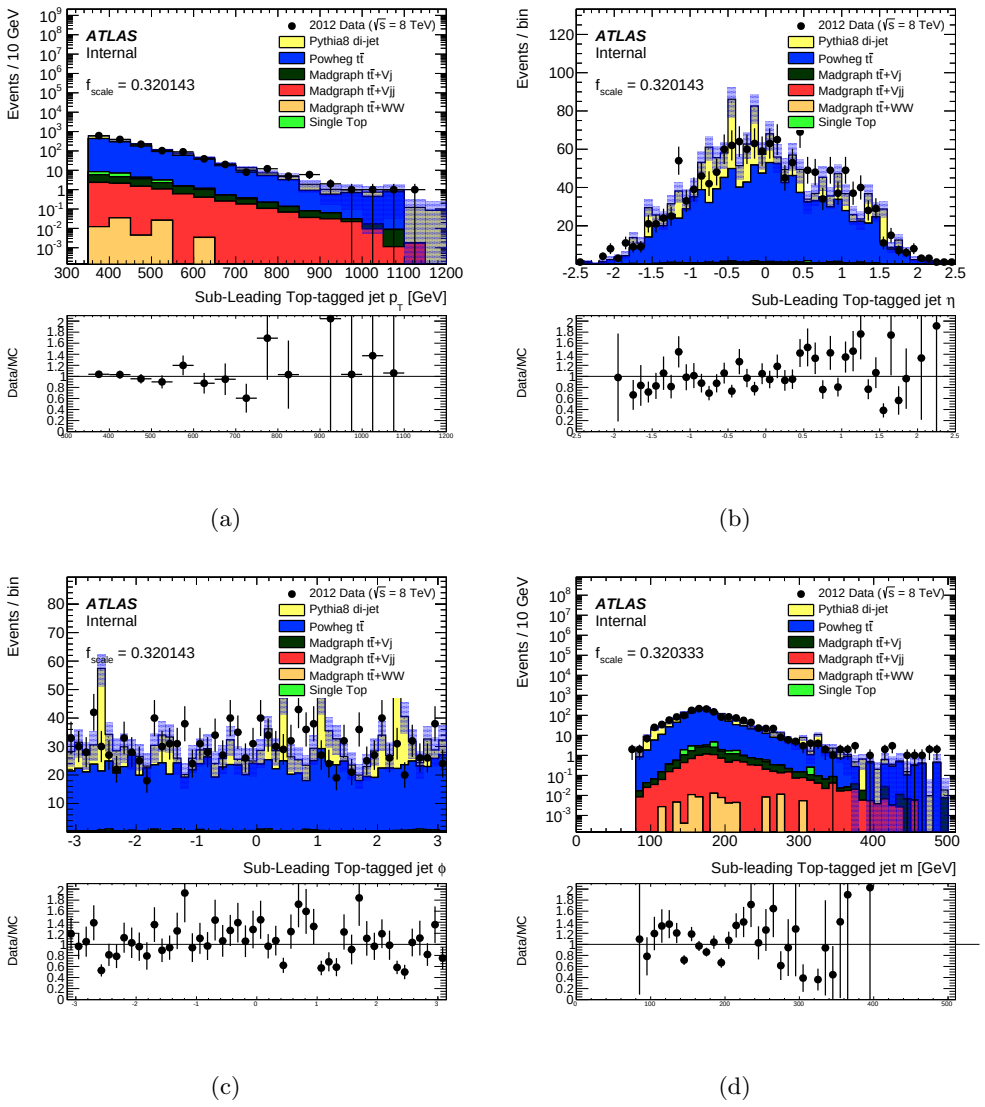

(a) (b)

(c) (d)

Figure 13.21: MC and data distributions of the sub-leading top-tagged fat-jet p_{T}, η, ϕ, and mass in the 2T-NoIsoB control region in events with at least two b-tagged jets. The Pythia8 QCD di-jet distributions are scaled to the difference between data and the Powheg $t\bar{t}$ MC (the scale factor is shown on the plot). Additional backgrounds are shown for comparison but not subtracted from the data.

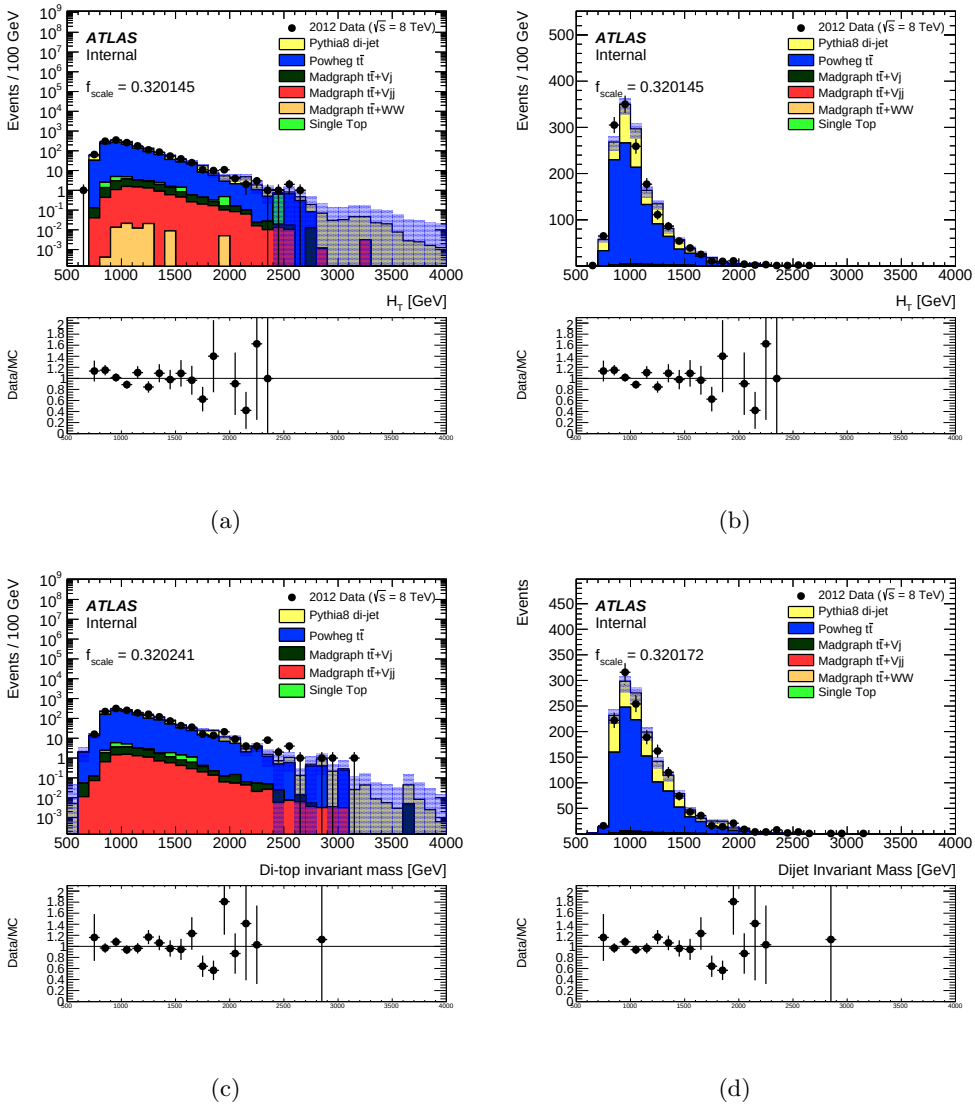

Figure 13.22: MC and data distributions of the H_{T} and di-top invariant mass in the 2T-NoIsoB control region in events with at least 2 b-tagged jets. The Pythia8 QCD di-jet distributions are scaled to the difference between data and the Powheg $t\bar{t}$ MC (the scale factor is shown on the plot). Additional backgrounds are shown for comparison but not subtracted from the data.

tagging decreases with higher H_{T}. One possible explanation for this result is that we are requiring that any b-tagged jet lie within the $\eta - \phi$ space of the top-tagged jets. As the p_{T} of these top-tagged jets increases (and thus increasing the H_{T} of the event), the p_{T} of their b-hadron decay products also increases, resulting in reduced tagging efficiency. This slight correlation results in an average shifting of events between regions A, B, C and D. That is, there would be more events in regions A and C than we expect and less events in regions B and D than we would expect (with a negative correlation).

More important is how we reconcile this with respect to the ABCD method. One way of dealing with this is to simply assign a systematic uncertainty to each region A, B and C based on $\rho_{N(b),H_{\mathrm{T}}}$. If we use the absolute value of the coefficient as un uncertainty on each region, the resulting relative uncertainty on the prediction in region D is $\sqrt{3 * |4.44|^2}\% = 7.7\%$.

	$\rho_{N(b),H_{\mathrm{T}}}$	Profile Fit Slope [GeV/b-jet]	Fit χ^2
Powheg $t\bar{t}$	-0.0872	-33.0 ± 8.18	0.060
Pythia8 di-jet	-0.00620	-2.14 ± 8.31	4.46
Data	-0.0444	-26.1 ± 6.08	4.00
Data-$t\bar{t}$	0.00754	-26.1 ± 6.08	4.00

Table 13.7: Correlation factor, profile fit slope and profile fit χ^2 between the H_{T} and the number of b-tagged jets in the 2T-NoIsoB control region for data, Powheg $t\bar{t}$ and Pythia8 di-jet.

The event yields for data, Powheg $t\bar{t}$ as well as our estimated multi-jet background are shown in Table **??** for the low H_{T} selection and in Table 13.9. The predicted number of events in the low H_{T} region is 13.85 , while we measured 14 events in the

	2T-NoIsoB Control and Signal Regions			
MC Sample	A	B	C	D
Data	25 ± 5	3681 ± 60.67	1513 ± 38.9	5 ± 2.236
Powheg $t\bar{t}$	6.029 ± 1.557	846.5 ± 16.44	1008 ± 16.42	2.278 ± 0.7185
Multi-jet	18.97 ± 6.557	2834 ± 77.12	505.4 ± 55.32	3.383 ± 1.23
Total	25 ± 5	3681 ± 60.67	1513 ± 38.9	5.661 ±1.424

Table 13.8: Data and backgrounds MC yields as well as the multi-jet prediction in the low H_{T} 2T-NoIsoB regions.

	2T-NoIsoB Control and Signal Regions			
MC Sample	A	B	C	D
Data	61 ± 7.81	3645 ± 60.37	1504 ± 38.78	14 ± 3.742
Powheg $t\bar{t}$	10.71 ± 1.932	841.8 ± 16.41	1003 ± 16.38	6.445 ± 1.288
Multi-jet	50.29 ± 9.742	2803 ± 76.78	500.6 ± 55.17	8.98 ± 2.017
Total	61 ± 7.81	3645 ± 60.37	1504 ± 38.78	15.43 ± 2.393

Table 13.9: Data and backgrounds MC yields as well as the multi-jet prediction in the high H_{T} 2T-NoIsoB regions.

data. In the high H_{T} region, the predicted number of background events is 5.297, while there were 5 events measured in data. For both selection regions, the predicted number of events matches the measured number within statistical uncertainty.

Given that there is a relatively small uncertainty with respect to using the ABCD method in this region, we will follow what we did in the 1T-TLFJ region and use the template method to predict some key kinematic distributions in events with at least two b-tagged jets. The H_{T} is shown in Fig. 13.23, di-top invariant mass in

Fig. 13.24, and the leading and sub-leading top-jet p_{T} in Fig. 13.25. There is excellent agreement between data and predicted background in this region.

The success of the ABCD+Template method in both the 1T+TLFJ as well as this 2T-NoIsoB control region is a good indication that it will be successful in the 2T-IsoB regions.

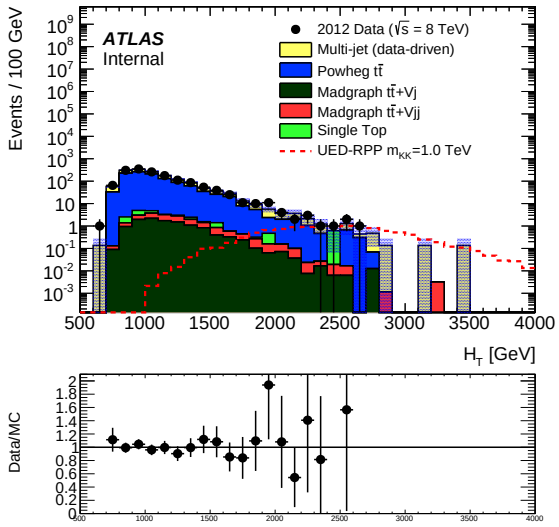

(a)

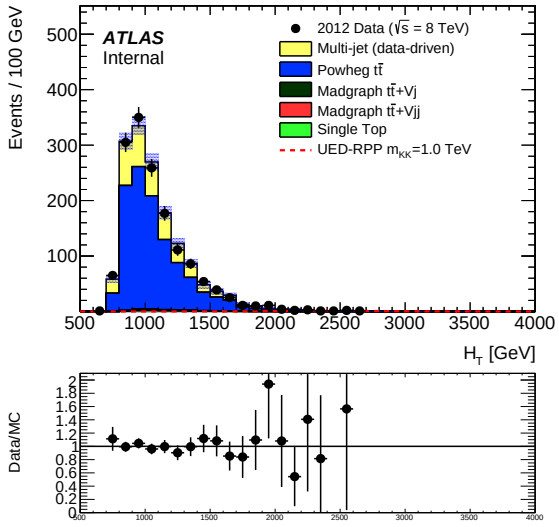

(b)

Figure 13.23: MC and data distributions of the H_{T} in the 2T-NoIsoB region. The multi-jet distribution is taken from events containing exactly one b-tagged jet and scaled to the predicted number of events with at least two b-tagged jets. Additional backgrounds are shown for comparison but not subtracted from the data. The 2UED-RPP $\mathrm{m}_{KK} = 1.0$ TeV signal distribution is also shown.

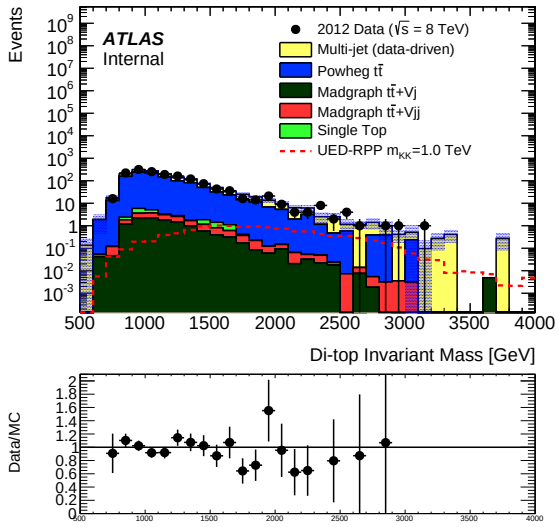

(a)

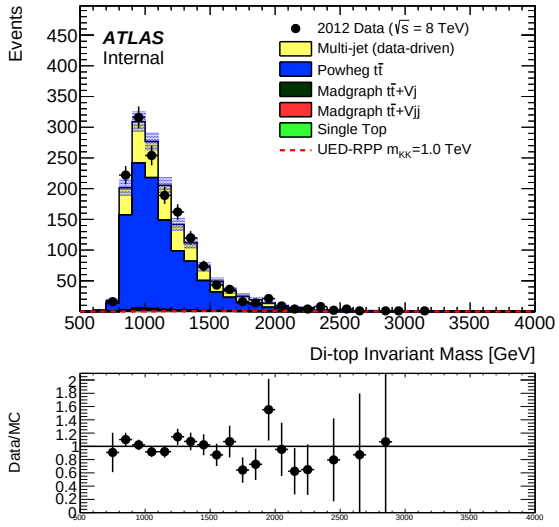

(b)

Figure 13.24: MC and data distributions of the di-top invariant mass in the 2T-NoIsoB region. The multi-jet distribution is taken from events containing exactly one b-tagged jet and scaled to the predicted number of events with at least two b-tagged jets. Additional backgrounds are shown for comparison but not subtracted from the data. The 2UED-RPP $m_{KK} = 1.0$ TeV signal distribution is also shown.

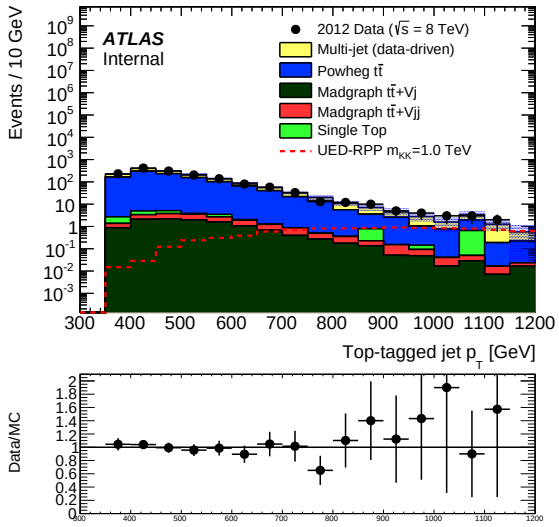

(a)

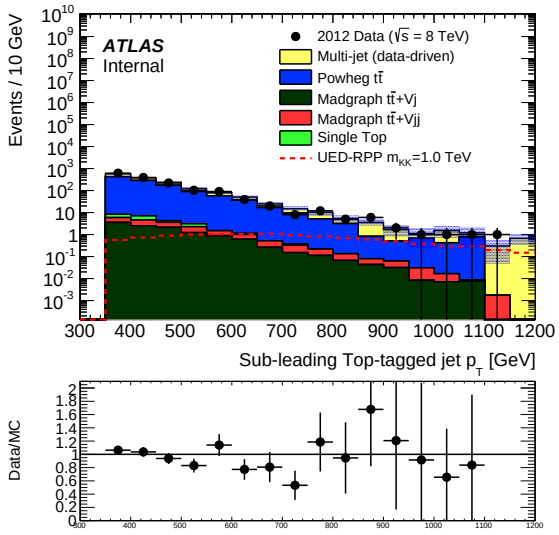

(b)

Figure 13.25: MC and data distributions of the leading and sub-leading top-tagged jet p_{T} in the 2T-NoIsoB region. The multi-jet distribution is taken from events containing exactly one b-tagged jet and scaled to the predicted number of events with at least two b-tagged jets. Additional backgrounds are shown for comparison but not subtracted from the data. The 2UED-RPP $\mathrm{m}_{KK} = 1.0$ TeV signal distribution is also shown.

Chapter 14

Systematic Uncertainties

14.1 Uncertainties on Monte Carlo samples

In this section we describe the systematic uncertainties associated with the $t\bar{t}$ background MC as well as our signal MC samples.

14.1.1 Object scales, substructure and resolution uncertainties

There are several sources of uncertainty associated with scale factors applied to jets used in this analysis as well as the uncertainties associated with our top-tagging variables. Additionally, we measure the jet energy resolution uncertainty . Those being,

- Jet Energy Scale (JES)

  The total JES uncertainty is obtained by independently varying the the JES of each jet up (down) by the relative JES uncertainty of each jet and comparing the nominal number of events where the jet-by-jet JES was varied up (down).

This uncertainty is asymmetric. The relative jet-by-jet uncertainty is obtained by using the `getRelUncertComponent(int compIndex, double pT, double eta)` function of the `JESUncertaintyProvider` class in the `JetUncertainties` software package. This tool returns the relative uncertainty of each JES nuisance parameters (there are 50, 47 obtained from in-situ analyses, 2 from eta inter calibration and one from the behavior of high p_{T} jets). These parameters are accessed independently and combined as the sum of squares for each of the up (down) variations.

- b-Jet Energy Scale (b-JES)

  Similar to how we obtain the JES uncertainty, the b-JES uncertainty is obtained by varying the 4-momentum of each b-tagged jet by the relative jet-by-jet BJES uncertainty up (down) and looking at the resulting number of events for each variation compared to the nominal selection. This nuisance parameter is accessed using the `getRelBJESUncert(double pT, double eta)` of the `MultijetJESUncertaintyProvider` class in the `JetUncertainties` software package.

- Flavor response and composition

  These uncertainties are also varied up (down) jet-by-jet for jets that are not b-tagged. The flavor response uncertainty is obtained using the `getRelFlavorResponseUncert(double pT, double eta)` function while the flavor composition uncertainty is obtained using the

`getRelFlavorCompUncert(double pT, double eta, bool isUp)` function, both of which are part of the `MultijetJESUncertaintyProvider` class in the `JetUncertainties` software package.

- Pile-up offset

  The pile-up offset uncertainty is composed of four components, namely the jet p_{T}, η, N_{PV} (the number of good primary vertices), μ (the number of estimated actual interactions) and ρ (a measure of the event's topology). These components are independently varied up and down by one sigma. The methods used to obtain these quantities are,

  - `getRelNPVOffsetTerm(double pT, double eta, int NPV)`
  - `getRelMuOffsetTerm(double pT, double eta, int mu)`
  - `getRelPileupPtTerm(double pT, double eta, int NPV, int mu)`
  - `getRelPileupRhoTopology(double pT, double eta)` .

- Jet Energy Resolution (JER)

  The JER uncertainty is obtained by smearing the 4-momentum of of each jet by a random amount based on a Gaussian distribution with a width based on the p_{T} and η of the jet. This is a symmetric uncertainty and therefore the up and down uncertainties are calculated from the percent difference between the number of events in the nominal analysis (no smearing) and those in the JER systematic run (with smearing).

- ISR/FSR

  Initial state radiation and final state radiation produce additional jets in the final state. This systematic can be calculated by calculating the difference between samples produced with more parton showering (MorePS) and less parton showering (LessPS) and comparing that number to the nominal sample yield. This systematic is available for the Powheg $t\bar{t}$ MC, however is not available for the signal samples.

- b-tagging scale factor (SF)

  The efficiency and inefficiency scale factor uncertainties are anti-correlated. Therefore, the b-SF uncertainty is evaluated by varying the b-SF up by 1 sigma and the inefficiency scale factor down by one sigma. Reversely, we vary the efficiency b-SF uncertainty down by 1 sigma and the inefficiency SF up by 1 sigma. This is repeated for both the c-SF and mistag-SF uncertainties.

- Jet substructure variables

  The uncertainties on the fat-jet substructure variables $\sqrt{d_{12}}$, τ_{31} and τ_{21} are evaluated by varying each quantity independently up and down by 1 sigma and looking at the resulting number of events.

14.1.2 Luminosity and production cross sections

The uncertainty on the integrated luminosity is $\pm 2.8\%$. It is derived, following the same methodology as that detailed in Ref. [70], from a preliminary calibration of the

luminosity scale derived from beam-separation scans (Van der Meer scans) performed in November 2012. This uncertainty applies to both Monte Carlo and data.

The $t\bar{t}$ production cross-section uncertainty at NNLO+NNLL is 5.26/-5.75%. The NLO cross-section uncertainty for the Sgluon samples that account for actorization/renomalization scales effects is 30%. The LO cross-section uncertainty for the 2UED-RPP samples was calculated to be close to 50%. There currently are no available uncertainties on the cross-sections of the Contact Interaction model nor the Standard Model 4-top MC.

14.1.3 Generator Uncertainties

We are not able to compute the uncertainty associated with $t\bar{t}$ MC generation in our signal region due to the lack of statistics from the MC@NLO sample (currently the only other full-simulation sample containing the fully hadronic final state).

14.1.4 ABCD Method Uncertainty

Since the ABCD method is calculated from the subtraction of $t\bar{t}$ events from the data, the statistical as well as systematic uncertainties associated with both the $t\bar{t}$ and data are propagated to the final prediction. Additionally, we add an uncertainty of 3.5% associated with the measured correlation in the 2T-IsoB regions B and C ($H_{\mathrm{T}} <$ 2.25 TeV).

	2UED-RPP m_{KK} [TeV]							
Systematic	0.6	0.8	1.0	1.05	1.10	1.15	1.20	1.25
JES	11.5/ − 9.93	8.47/ − 7.74	3.86/ − 4.25	3.43/ − 3.74	2.88/ − 2.93	2.27/ − 2.5	2/ − 2.11	1.64/ − 1.8
b-JES	2.11/ − 1.77	1.56/ − 1.64	0.641/ − 0.857	0.556/ − 0.741	0.448/ − 0.68	0.391/ − 0.59	0.326/ − 0.605	0.309/ − 0.547
Flavor	8.83/ − 8.48	6.06/ − 6.72	2.64/ − 3.46	2.17/ − 2.81	1.88/ − 2.29	1.44/ − 1.91	1.26/ − 1.54	0.949/ − 1.23
Offset	3.79/ − 2.92	2.84/ − 2.53	1.25/ − 1.25	1.16/ − 1.13	0.905/ − 0.959	0.806/ − 0.886	0.717/ − 0.718	0.7/ − 0.638
JER	0.117/ − 0.117	0.563/ − 0.563	0.41/ − 0.41	0.426/ − 0.426	0.434/ − 0.434	0.564/ − 0.564	0.621/ − 0.621	0.758/ − 0.758
FJ p_T	0.65/ − 0.654	0.679/ − 0.683	0.38/ − 0.388	0.443/ − 0.433	0.365/ − 0.46	0.314/ − 0.314	0.421/ − 0.388	0.26/ − 0.321
$\sqrt{d_{12}}$	1.67/ − 2.65	1.86/ − 2.87	2.34/ − 2.91	2.39/ − 2.9	2.49/ − 2.96	2.84/ − 2.71	2.51/ − 2.49	2.27/ − 2.68
τ_{32}	4.19/ − 5.28	3.44/ − 4.89	3.02/ − 3.71	2.96/ − 3.77	2.66/ − 3.86	2.98/ − 3.65	2.62/ − 3.45	2.6/ − 3.41
τ_{21}	4.83/ − 7	4.41/ − 6.33	4.94/ − 6.1	4.46/ − 5.76	4.22/ − 5.56	4.48/ − 5.57	4.22/ − 5.55	4.15/ − 5.21
b-SF	0.96/ − 0.614	0.417/ − 0.0608	0.742/ − 0.336	0.868/ − 0.436	0.881/ − 0.422	1.02/ − 0.554	1.29/ − 0.828	1.3/ − 0.825
c-SF	0.51/ − 0.511	0.552/ − 0.575	0.555/ − 0.571	0.468/ − 0.485	0.604/ − 0.621	0.577/ − 0.595	0.539/ − 0.554	0.411/ − 0.42
Mistag-SF	0.784/ − 0.776	0.817/ − 0.806	0.845/ − 0.838	0.835/ − 0.824	0.891/ − 0.881	0.823/ − 0.804	0.802/ − 0.796	0.958/ − 0.933
Luminosity	2.8/ − 2.8	2.8/ − 2.8	2.8/ − 2.8	2.8/ − 2.8	2.8/ − 2.8	2.8/ − 2.8	2.8/ − 2.8	2.8/ − 2.8
Total	16.8/ − 16.6	12.8/ − 14	8.52/ − 10	7.9/ − 9.42	7.35/ − 8.91	7.45/ − 8.5	6.94/ − 8.16	6.67/ − 7.85

Table 14.1: Table showing the relative systematic uncertainties associated with the various signal samples associated with the high-H_{T} two top-tag signal region.

14.1.5 2UED-RPP

The 2UED-RP samples are all simulated using the GEANT4 full-simulation, so there is no uncertainty associated with simulation. The systematic uncertainties associated with these samples are shown in Table 14.1 for the 2T low-H_{T} ,Table 14.2 for the high-H_{T} signal regions. The largest sources of uncertainties are the JES as well as the substructure variables. The JES uncertainty decreases with increasing KK mass, which makes sense as the average energy of the jets increases with KK mass (and the JES uncertainty decreases as p_{T} increases). As for the substructure variables, the uncertainties seem to remain relatively flat across the KK mass range. The largest source among these is those from the τ_{21} variable. The reason for this is not completely understood and require further study.

	2UED-RPP m_{KK} [TeV]							
Systematic	0.6	0.8	1.0	1.05	1.10	1.15	1.20	1.25
JES	9.84/ − 8.58	5.35/ − 5.54	2.11/ − 2.08	1.75/ − 1.81	1.34/ − 1.53	1.15/ − 1.27	0.855/ − 1.12	0.877/ − 0.969
b-JES	1.63/ − 1.91	0.892/ − 1.17	0.313/ − 0.548	0.297/ − 0.544	0.2/ − 0.451	0.168/ − 0.373	0.0943/ − 0.372	0.104/ − 0.376
Flavor	6.83/ − 7.38	3.69/ − 4.58	1.3/ − 1.56	0.992/ − 1.25	0.74/ − 0.976	0.617/ − 0.829	0.423/ − 0.656	0.359/ − 0.526
Offset	3.46/ − 3.08	1.73/ − 1.86	0.8/ − 0.722	0.699/ − 0.715	0.548/ − 0.529	0.5/ − 0.506	0.333/ − 0.431	0.466/ − 0.44
JER	0.168/ − 0.168	0.116/ − 0.116	0.665/ − 0.665	0.822/ − 0.822	0.834/ − 0.834	0.893/ − 0.893	1.01/ − 1.01	1/ − 1
FJ p_T	1.01/ − 1.07	0.915/ − 1.07	0.49/ − 0.617	0.515/ − 0.658	0.495/ − 0.615	0.411/ − 0.486	0.473/ − 0.488	0.293/ − 0.427
$\sqrt{d_{12}}$	2.44/ − 3.43	2.46/ − 3.4	2.51/ − 3.31	2.63/ − 3.17	2.81/ − 3.17	3.02/ − 2.9	2.67/ − 2.69	2.39/ − 2.83
τ_{32}	4.97/ − 6.37	3.8/ − 5.38	3.25/ − 4.1	3.11/ − 4.01	2.82/ − 4.06	3.07/ − 3.8	2.74/ − 3.74	2.69/ − 3.54
τ_{21}	6.21/ − 8.34	5.49/ − 7.49	5.51/ − 6.8	4.92/ − 6.41	4.75/ − 6.07	4.76/ − 6.1	4.54/ − 5.9	4.41/ − 5.55
b-SF	0.235/ − 0.108	0.117/ − 0.464	0.481/ − 0.0879	0.625/ − 0.209	0.697/ − 0.256	0.829/ − 0.372	1.13/ − 0.672	1.17/ − 0.697
c-SF	0.585/ − 0.588	0.501/ − 0.525	0.537/ − 0.549	0.471/ − 0.487	0.604/ − 0.618	0.583/ − 0.6	0.532/ − 0.547	0.414/ − 0.424
Mistag-SF	0.734/ − 0.726	0.705/ − 0.698	0.812/ − 0.803	0.793/ − 0.783	0.862/ − 0.852	0.834/ − 0.817	0.791/ − 0.786	0.929/ − 0.902
Luminosity	2.8/ − 2.8	2.8/ − 2.8	2.8/ − 2.8	2.8/ − 2.8	2.8/ − 2.8	2.8/ − 2.8	2.8/ − 2.8	2.8/ − 2.8
Total	15.4/ − 16.5	10.3/ − 12.8	7.99/ − 9.55	7.44/ − 9.09	7.17/ − 8.79	7.33/ − 8.53	6.89/ − 8.27	6.7/ − 7.97

Table 14.2: Table showing the relative systematic uncertainties associated with the various signal samples associated with the low-H_{T} two top-tag signal region.

14.1.6 Sgluon

The Sgluon samples are simulated using the ATLFast-2 fast-simulation. To assess the systematic uncertainty of this fact, a single sample corresponding to m_σ = 1.0 TeV was simulated using the GEANT4 full-simulation. An uncertainty of 10.9% was found to be the result of using ATLFast-2 vs. the full-simulation.

Tables 14.3 and 14.4 shows the estimated systematic uncertainties for the Sgluon samples for the 2T low- and high-H_{T} signal regions.

14.2 Contact Interactions

The systematic uncertainties associated with the contact interaction model are currently being evaluated.

	Sgluon m_σ [TeV]					
Systematic	0.4	0.5	0.6	0.8	1.00	1.25
JES	$7.18/-5.45$	$23.8/-17.6$	$11.9/-6.76$	$11/-9.48$	$7.74/-6.97$	$3.52/-4.3$
b-JES	$7.16/-0.208$	$1.46/-6.51$	$1.82/-3.31$	$2.36/-1.13$	$1.84/-1.46$	$0.71/-1.15$
Flavor	$7.16/-5.43$	$18.5/-8.7$	$10.6/-8.11$	$7.22/-7.63$	$5.08/-6.61$	$2.2/-3.43$
Offset	$7.24/-0.159$	$1.38/-6.16$	$2.27/-5.22$	$4.07/-2.4$	$2.95/-2.26$	$1.18/-1.31$
JER	$1.88/-1.88$	$7.88/-7.88$	$0.643/-0.643$	$1.84/-1.84$	$0.346/-0.346$	$0.104/-0.104$
FJ p_T	$0/-0$	$3.94/-0$	$2.01/-4.42$	$1.88/-2.4$	$1.2/-0.968$	$0.784/-0.789$
$\sqrt{d_{12}}$	$0/-0$	$0/-2.15$	$6.28/-4.23$	$3.44/-7.9$	$3.69/-3.72$	$4.04/-4.45$
τ_{32}	$8.45/-5.63$	$3.6/-10.5$	$5.9/-8.58$	$3.33/-5.65$	$3.02/-4.42$	$2.36/-3.3$
τ_{21}	$0/-10.6$	$5.29/-12.6$	$15.3/-16$	$9.75/-16$	$8.6/-10.9$	$8.42/-9.46$
b-SF	$0.89/-1.51$	$1.21/-1.48$	$4.14/-4.27$	$0.588/-0.92$	$1.45/-1.69$	$0.732/-1.06$
c-SF	$2.35/-2.49$	$2.58/-2.47$	$0.000539/-0.0364$	$0.784/-0.76$	$0.681/-0.716$	$0.663/-0.669$
Mistag-SF	$0.559/-0.562$	$2.39/-2.44$	$1.22/-1.11$	$1.09/-1.1$	$0.582/-0.598$	$0.641/-0.643$
Luminosity	$2.8/-2.8$	$2.8/-2.8$	$2.8/-2.8$	$2.8/-2.8$	$2.8/-2.8$	$2.8/-2.8$
Total	$17.2/-14.9$	$32.5/-28.7$	$24.5/-23.3$	$18.2/-22.9$	$14.4/-16.3$	$11/-12.8$

Table 14.3: Table showing the relative systematic uncertainties associated with the various signal samples associated with the high-H_{T} two top-tag signal region.

	Sgluon m_σ [TeV]					
Systematic	0.4	0.5	0.6	0.8	1.00	1.25
JES	$0.488/-0.0622$	$19.6/-1.01$	$13.5/-19.7$	$10/-13.9$	$10/-10.8$	$5.85/-5.78$
b-JES	$0/-0$	$0.961/-0$	$3.56/-2.73$	$3.17/-2.84$	$2.01/-1.72$	$1.18/-1.38$
Flavor	$0/-0.105$	$10.2/-0$	$10.3/-14.2$	$7.79/-11.6$	$7.45/-8.34$	$4.38/-4.48$
Offset	$0.548/-0.133$	$0.939/-0.922$	$3.48/-3.24$	$2.63/-3.52$	$3.04/-2.66$	$2.02/-1.65$
JER	$0/-0$	$10.2/-10.2$	$2.45/-2.45$	$1.1/-1.1$	$0.309/-0.309$	$0.758/-0.758$
FJ p_T	$0/-0$	$0/-0$	$0/-0$	$2.56/-0.683$	$0.771/-0.837$	$0.563/-0.521$
$\sqrt{d_{12}}$	$0/-0$	$0/-0$	$13.3/-3.41$	$3.63/-9.14$	$3.38/-4.2$	$3.67/-3.72$
τ_{32}	$44.3/-0$	$9.66/-0$	$3.62/-5.94$	$3.41/-4.91$	$2.83/-4.03$	$2.48/-3.07$
τ_{21}	$0/-0$	$0/-21.7$	$23.7/-22.6$	$10.7/-14.2$	$7.15/-10.5$	$8/-7.68$
b-SF	$9.52/-9.83$	$4.58/-4.18$	$0.0384/-0.621$	$0.357/-0.619$	$1.01/-1.28$	$0.417/-0.743$
c-SF	$1.52/-1.7$	$3.03/-2.67$	$0.869/-0.906$	$1.03/-1$	$0.508/-0.507$	$0.66/-0.663$
Mistag-SF	$0.741/-0.745$	$5.01/-5.1$	$0.194/-0.192$	$0.624/-0.602$	$0.419/-0.434$	$0.773/-0.77$
Luminosity	$2.8/-2.8$	$2.8/-2.8$	$2.8/-2.8$	$2.8/-2.8$	$2.8/-2.8$	$2.8/-2.8$
Total	$45.4/-10.4$	$27.3/-25.2$	$32.8/-34.4$	$18.3/-25.9$	$15.8/-18.7$	$12.3/-12.3$

Table 14.4: Table showing the relative systematic uncertainties associated with the various signal samples associated with the low-H_{T} two top-tag signal region.

14.3 Standard Model 4-top

The systematic uncertainties associated with the contact interaction model are currently being evaluated.

14.4 $t\bar{t}$

In this section we present the measured systematic uncertainties associated with the Powheg $t\bar{t}$ Monte Carlo sample as well as our interpretation of the results.

14.4.1 Two top NoIsoB Control Region

For both the low H_{T} and high H_{T} selections, we find that the largest uncertainties arise from the JES as well as the substructure variables, similar to those for the signal samples. However, the uncertainties are much larger, likely due to the on-average lower jet energies. These uncertainties re summarized in Tables 14.5 and 14.6. The very large uncertainties in regions A and D are due to the lack of statistics in the nominal as well as systematic samples. These could potentially be reduced by modeling the H_{T} distribution or increasing the number of generated events.

14.4.2 2T-IsoB Systematic Uncertainties

Similar to the region with no isolated b-tagged jets, the uncertainties in the 2T-IsoB regions are dominated by statistical fluctuations in regions A and D, and quite large uncertainties associated with the top-tagging variables. These uncertainties are shown

	Powheg $t\bar{t}$			
Systematic	A	B	C	D
JES	$18.7/-8.71$	$0.312/-0.133$	$0.185/-0.309$	$10.6/-17.2$
b-JES	$0/-0$	$0/-0.0644$	$0/-0.0137$	$0/-2.84$
Flavor	$11.7/-5.37$	$0.149/-0.0497$	$0.0287/-0.11$	$4.48/-17.5$
Offset	$5.9/-0.263$	$0.217/-0.108$	$0.0105/-0.0581$	$0.000274/-2.83$
JER	$4.86/-4.86$	$0.334/-0.334$	$0.0119/-0.0119$	$5.4/-5.4$
FJ p_T	$0/-0$	$8.14/-9.54$	$10.2/-11.2$	$0/-0$
$\sqrt{d_{12}}$	$9.96/-0$	$7.57/-8.65$	$6.24/-8.21$	$1.48/-0$
τ_{32}	$13.1/-2.74$	$3.64/-3.79$	$1.86/-3.11$	$4.21/-0$
τ_{21}	$14.2/-7.44$	$10.5/-13.1$	$9.38/-11.6$	$0/-6.62$
b-SF	$5.06/-4.8$	$4.07/-3.63$	$5.48/-5.36$	$6.68/-6.51$
c-SF	$1.1/-1.11$	$1.63/-1.64$	$1.52/-1.55$	$0.252/-0.241$
Mistag-SF	$1.51/-1.55$	$0.398/-0.4$	$0.651/-0.653$	$0.463/-0.488$
ISR/FSR	$9.931/-9.931$	$4.965/-4.965$	$1.673/-1.673$	$3.966/-3.966$
Luminosity	$2.8/-2.8$	$2.8/-2.8$	$2.8/-2.8$	$2.8/-2.8$
Total	$33.9/-18$	$17.3/-20$	$16.6/-19.5$	$15.8/-27.5$

Table 14.5: Table showing the relative systematic uncertainties for the Powheg $t\bar{t}$ MC for the low-H_{T} two top-tag region with no isolated b-tagged jets (NoIsoB).

	Powheg $t\bar{t}$			
Systematic	A	B	C	D
JES	$12.7/-5.53$	$0.164/-0.0617$	$0.133/-0.266$	$7.19/-30.2$
b-JES	$0/-0$	$0/-0.064$	$0/-0.0045$	$0/-0$
Flavor	$7.18/-5.07$	$0.0511/-0.0175$	$0.0163/-0.0437$	$7.23/-20.4$
Offset	$1.97/-5.55$	$0.155/-0.144$	$0.0104/-0.0398$	$0.00691/-0.00284$
JER	$0.13/-0.13$	$0.393/-0.393$	$0.0466/-0.0466$	$10.6/-10.6$
FJ p_T	$0/-0$	$8.1/-9.49$	$10.1/-11.1$	$0/-0$
$\sqrt{d_{12}}$	$5.21/-0$	$7.62/-8.6$	$6.22/-8.18$	$0/-0$
τ_{32}	$5.21/-0.123$	$3.74/-3.8$	$1.88/-3.09$	$0/-0$
τ_{21}	$1.58/-0$	$10.7/-13.2$	$9.34/-11.6$	$0/-2.51$
b-SF	$6.98/-6.88$	$4.06/-3.62$	$5.48/-5.36$	$7.42/-7.16$
c-SF	$1.36/-1.37$	$1.63/-1.64$	$1.52/-1.55$	$0.381/-0.387$
Mistag-SF	$3.15/-3.23$	$0.399/-0.401$	$0.654/-0.655$	$0.861/-0.866$
ISR/FSR	$43.40/-43.40$	$4.755/-4.755$	$1.570/-1.570$	$54.02/-54.02$
Luminosity	$2.8/-2.8$	$2.8/-2.8$	$2.8/-2.8$	$2.8/-2.8$
Total	$47.2/-45.1$	$17.4/-20$	$16.6/-19.4$	$56.6/-66.5$

Table 14.6: Table showing the relative systematic uncertainties for the Powheg $t\bar{t}$ MC for the high-H_{T} two top-tag region with no isolated b-tagged jets (NoIsoB).

	Powheg $t\bar{t}$			
Systematic	A	B	C	D
JES	$12.4/-0.0569$	$0.712/-0.319$	$0.408/-0.384$	$25.9/-28.4$
b-JES	$0/-0$	$0/-0.0271$	$0/-0.479$	$0/-4.44$
Flavor	$12.5/-0$	$0.503/-0.00396$	$0.597/-0.447$	$21.5/-16.8$
Offset	$0.0138/-0.0148$	$0.571/-0.901$	$0.928/-0.73$	$0.00367/-16$
JER	$0/-0$	$1.69/-1.69$	$2.72/-2.72$	$16.4/-16.4$
FJ p_T	$0/-0$	$14/-12.4$	$12.1/-11.6$	$0/-4.44$
$\sqrt{d_{12}}$	$11.6/-26.2$	$8.37/-12.3$	$9.51/-9.13$	$4.34/-14.9$
τ_{32}	$15.2/-4.75$	$6/-8.9$	$5.16/-6.09$	$2.03/-11.8$
τ_{21}	$1.78/-24.6$	$16.9/-14.7$	$13/-15.9$	$0/-20.8$
b-SF	$5.15/-4.84$	$5.03/-4.76$	$4.44/-4.4$	$1.7/-1.69$
c-SF	$0.323/-0.338$	$1.5/-1.52$	$1.75/-1.77$	$1.69/-1.74$
Mistag-SF	$1.92/-1.96$	$0.179/-0.172$	$1.74/-1.75$	$3.34/-3.4$
ISR/FSR	$8.61/-8.61$	$2.668/-2.668$	$3.182/-3.182$	$0/-0$
Luminosity	$2.8/-2.8$	$2.8/-2.8$	$2.8/-2.8$	$2.8/-2.8$
Total	$28.1/-37.7$	$25.2/-25.4$	$22/-23.7$	$38.1/-49.7$

Table 14.7: Table showing the relative systematic uncertainties for the Powheg $t\bar{t}$ MC for the low-H_{T} two top-tag signal region.

in Table 14.7 for the low-H_{T} selection and in Table 14.8 for the high-H_{T} selection.The JES uncertainty for both selections is quite small for regions B and C. Overall, we see between 22% and 49% relative uncertainty for the low-H_{T} selection while for the high-H_{T} selection we measure between 15% and 79% relative uncertainty across the regions.

	Powheg $t\bar{t}$			
Systematic	A	B	C	D
JES	$10.1/-28.3$	$1.02/-0.145$	$1.11/-1.03$	$0.00491/-14.2$
b-JES	$0/-0$	$0/-0.0265$	$0/-0.591$	$0/-0$
Flavor	$10.1/-28.4$	$0.163/-0.452$	$0/-0.0199$	$0/-0$
Offset	$0.0253/-0.0144$	$0.557/-0.881$	$0.91/-1.15$	$0.00524/-0.00542$
JER	$10.1/-10.1$	$1.81/-1.81$	$2.23/-2.23$	$0/-0$
FJ p_T	$0/-0$	$13.7/-12.1$	$11.8/-11.5$	$0/-0$
$\sqrt{d_{12}}$	$20.5/-28.5$	$8.3/-12.5$	$9.33/-9.28$	$14.2/-9.64$
τ_{32}	$28.3/-11.6$	$6.01/-8.7$	$5.12/-6.3$	$0/-0$
τ_{21}	$4.34/-60$	$16.5/-14.4$	$12.8/-15.9$	$0/-30.3$
b-SF	$3.24/-2.81$	$5.06/-4.8$	$4.37/-4.32$	$3.79/-3.94$
c-SF	$0.757/-0.757$	$1.46/-1.48$	$1.76/-1.78$	$0.723/-0.818$
Mistag-SF	$1.22/-1.23$	$0.0804/-0.071$	$1.81/-1.82$	$0.843/-0.85$
ISR/FSR	$0/-0$	$2.944/-2.944$	$3.122/-3.122$	$0/-0$
Luminosity	$2.8/-2.8$	$2.8/-2.8$	$2.8/-2.8$	$2.8/-2.8$
Total	$39.6/-79.2$	$24.8/-25.2$	$21.6/-23.7$	$15/-35.2$

Table 14.8: Table showing the relative systematic uncertainties for the Powheg $t\bar{t}$ MC for the high-H_{T} two top-tag signal region.

Chapter 15

Results

In this section we present the results of our search for new physics in the 2+ top-tagged plus 2+ b-tagged jet signal region.

15.1 Data and estimated backgrounds

The full cut-flow for our 2012 data, the estimated $t\bar{t}$ background, as well as several other background models are shown in Table 15.1. Currently the signal region event yields are blinded until we receive approval from the editorial board to un-blind. For readability, statistical uncertainties are not shown in the aforementioned table.

Our final results are shown in Table 15.2 for the low-H_{T} selection as well as in Table 15.3 for the high-H_{T} selection. The data in region D for both cases is still blinded, however we do show our estimated background prediction that includes the statistical uncertainties as well as the systematic uncertainties. The statistical uncertainties on the multi-jet contributions are calculated from the propagation of statistical

	Sample				
Cut	Data	$t\bar{t}$	Single-top	$t\bar{t}+Vj$	$t\bar{t}+Vjj$
Event Skim	6104619	41124.85	2943.987	319.5707	256.7871
LAr Error	6085832	41124.85	2943.987	319.5707	256.7871
Core Error	6085784	41124.85	2943.987	319.5707	256.7871
Tile Trip	6085781	41124.85	2943.987	319.5707	256.7871
Tile Error	6074140	41124.85	2943.987	319.5707	256.7871
Good Runs List	5805087	41124.85	2943.987	319.5707	256.7871
Good Vertex	5801485	41091.26	2943.061	319.276	256.5862
Jet Cleaning	5776208	40870.62	2901.225	318.8985	257.132
Trigger	5197899	40550.74	2876.04	317.9081	256.5117
PreTopTag	1894464	28092.21	1939.193	230.1038	188.2602
1T+1TLFJ	11102	2211.619	59.76654	25.48965	20.14909
1T+1TLFJ 1B	7452	770.9968	26.42545	8.172886	6.771538
1T+1TLFJ 2B+	3650	1440.625	33.34111	17.31674	13.37756
2T NoIsoB	5224	1862.398	22.21222	19.86304	15.40662
2T NoIsoB 1B	3706	852.5355	15.9802	9.261408	7.455895
2T NoIsoB 2B+	1518	1009.86	6.232028	10.60159	7.950711
2T IsoB $H_{\mathrm{T}} < 2.00$ TeV	941	249.8212	5.418155	5.1998	5.360563
2T IsoB 1B $H_{\mathrm{T}} < 2.00$ TeV	500	56.05457	2.645571	1.154403	1.22825
2T IsoB 2B+ $H_{\mathrm{T}} < 2.00$ TeV	441	193.7664	2.772584	4.045392	4.132307
2T IsoB $H_{\mathrm{T}} \geq 2.00$ TeV	blind	7.635658	0	0.2763907	0.2308186
2T IsoB 1B $H_{\mathrm{T}} \geq 2.00$ TeV	16	2.250062	0	0.07104645	0.09799822
2T IsoB 2B+ $H_{\mathrm{T}} \geq 2.00$ TeV	blind	5.385595	0	0.2053443	0.1328204
2T IsoB $H_{\mathrm{T}} < 2.25$ TeV	957	254.8824	5.418155	5.36011	5.487798
2T IsoB 1B $H_{\mathrm{T}} < 2.25$ TeV	509	57.38292	2.645571	1.198386	1.274255
2T IsoB 2B+ $H_{\mathrm{T}} < 2.25$ TeV	448	197.4994	2.772584	4.161722	4.213538
2T IsoB $H_{\mathrm{T}} \geq 2.25$ TeV	blind	2.574412	0	0.1160797	0.1035848
2T IsoB 1B $H_{\mathrm{T}} \geq 2.25$ TeV	7	0.9217157	0	0.02706328	0.0519934
2T IsoB 2B+ $H_{\mathrm{T}} \geq 2.25$ TeV	blind	1.652696	0	0.08901637	0.05159142

Table 15.1: Full cut flow for data, $t\bar{t}$, single-top as well as $t\bar{t}+V$ MC for the two-top-tag analysis.

	2T-IsoB Control and Signal Regions			
MC Sample	A	B	C	D
Data	16 ± 4	500 ± 22.36	441 ± 21	Blind
Powheg $t\bar{t}$	$2.25 \pm 0.7903^{+0.6323}_{-0.8483}$	$56.05 \pm 4.232^{+14.13}_{-14.24}$	$193.8 \pm 7.348^{+42.63}_{-45.92}$	$5.386 \pm 1.351^{+2.052}_{-2.677}$
Multi-jet	$13.75 \pm 4.79^{+0.6323}_{-0.8483}$	$443.9 \pm 26.59^{+14.13}_{-14.24}$	$247.2 \pm 28.35^{+42.63}_{-45.92}$	$7.657 \pm 2.846^{+3.345}_{-3.926}$
Total	16 ± 4	500 ± 22.36	441 ± 21	$13.04 \pm 3.15^{+3.925}_{-4.751}$

Table 15.2: Data and backgrounds MC yields as well as the multi-jet prediction in the low H_{T} 2T-IsoB regions.

	2T-IsoB Control and Signal Regions			
MC Sample	A	B	C	D
Data	7 ± 2.646	509 ± 22.56	448 ± 21.17	Blind
Powheg $t\bar{t}$	$0.9217 \pm 0.483^{+0.365}_{-0.73}$	$57.38 \pm 4.278^{+14.23}_{-14.46}$	$197.5 \pm 7.439^{+42.66}_{-46.81}$	$1.653 \pm 0.6906^{+0.2479}_{-0.5817}$
Multi-jet	$6.078 \pm 3.129^{+0.365}_{-0.73}$	$451.6 \pm 26.84^{+14.23}_{-14.46}$	$250.5 \pm 28.61^{+42.66}_{-46.81}$	$3.371 \pm 1.789^{+1.735}_{-2.914}$
Total	7 ± 2.646	509 ± 22.56	448 ± 21.17	$5.024 \pm 1.918^{+1.753}_{-2.971}$

Table 15.3: Data and backgrounds MC yields as well as the multi-jet prediction in the high H_{T} 2T-IsoB regions.

uncertainties from the data and $t\bar{t}$ MC. The same is true for the systematic uncertainties. We predict $13.04 \pm 3.15^{+3.925}_{-4.751}$ background events in the low-H_{T} region. The large systematic uncertainties come mainly from the large $t\bar{t}$ systematic uncertainties in regions A and D, where statistics are quite limited. For the high-H_{T} region, we predict $5.024 \pm 1.918^{+1.753}_{-2.971}$ background events. This result is for the most part dominated by statistical uncertainty, however due to the large statistical fluctuations in the systematic samples in regions A, we have a very large downward uncertainty prediction.

In the same way that we demonstrated the validity of the ABCD method in Section **??**, we can show predictions on the shapes of some key distributions using the

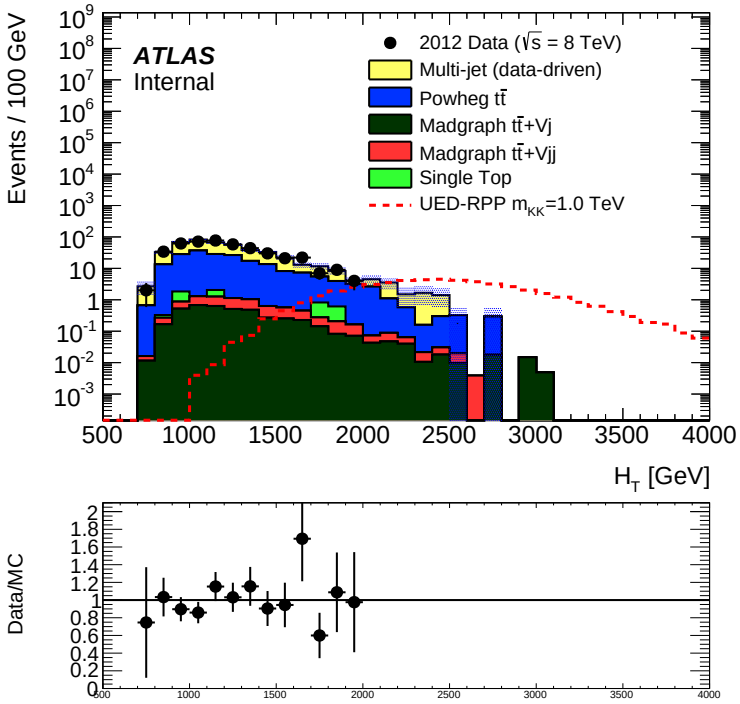

Figure 15.1: Measured H_{T} distribution in events with two or more b-tagged jets for the low H_{T} selection. The predicted H_{T} distribution predicted from the one b-tagged bin scaled to the predicted number of events in our signal region is also shown. We show our benchmark model MC distribution as well. Only statistical uncertainties are shown.

resulting background estimations given in Tables 15.2 and 15.3. Figures 15.1 and 15.2 show the predicted as well as measured (modulo the blinded region) H_{T} distributions for the low-H_{T} selection in standard and semi-log formats. Similarly, figures 15.3 and 15.4 show the H_{T} distributions for the high-H_{T} selection. In all of these plots, our benchmark 1 TeV 2UED-RPP mass point is shown. There is very good agreement across the entire range of the H_{T} to within statistical uncertainties. The systematic uncertainties are not shown in these distributions.

To show that our background estimation is also good for additional quantities,

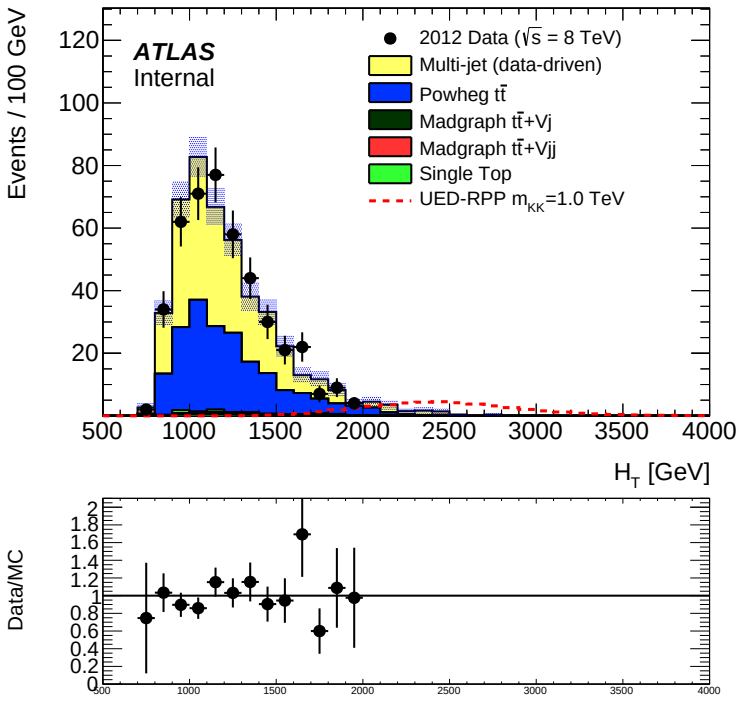

Figure 15.2: Measured H_{T} distribution in events with two or more b-tagged jets for the low H_{T} selection. The predicted H_{T} distribution predicted from the one b-tagged bin scaled to the predicted number of events in our signal region is also shown. We show our benchmark model MC distribution as well. Only statistical uncertainties are shown.

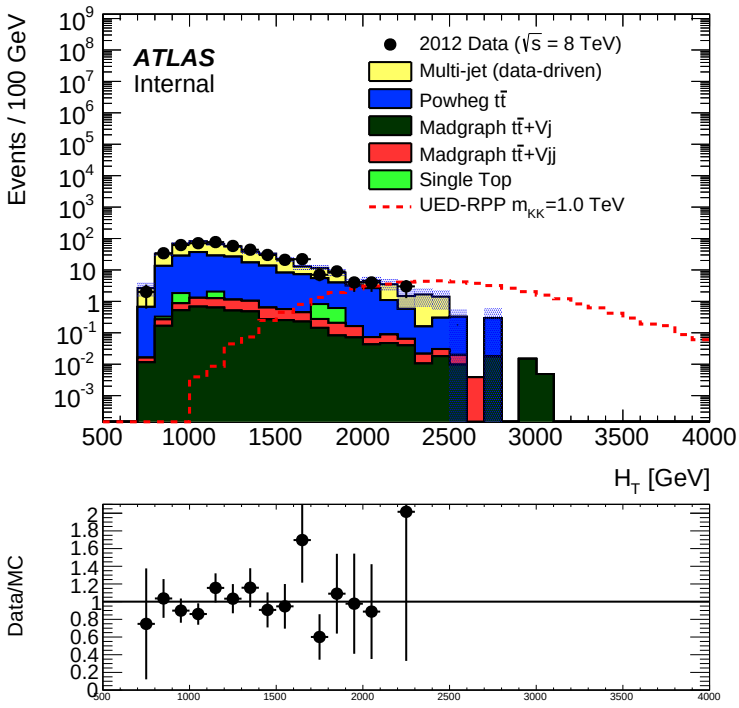

Figure 15.3: Measured H_{T} distribution in events with two or more b-tagged jets for the low H_{T} selection. The predicted H_{T} distribution predicted from the one b-tagged bin scaled to the predicted number of events in our signal region is also shown. We show our benchmark model MC distribution as well. Only statistical uncertainties are shown.

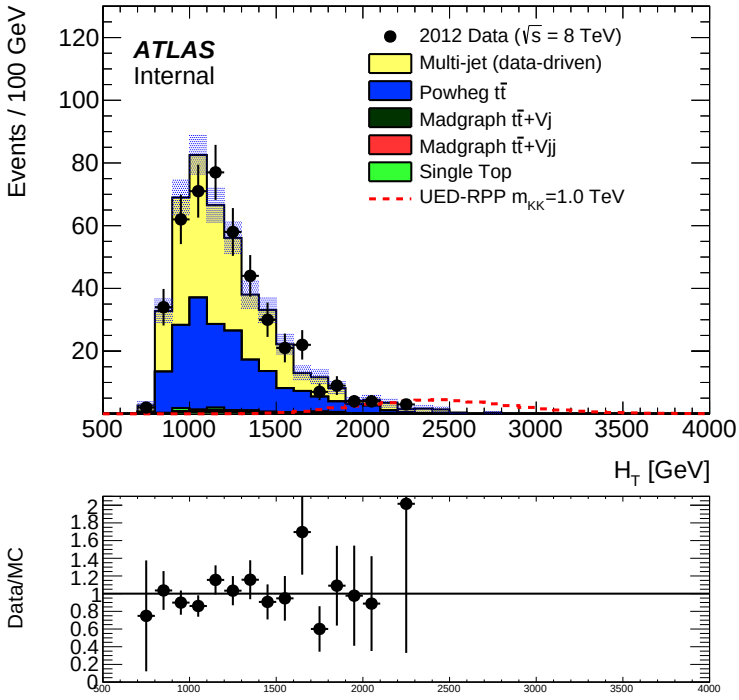

Figure 15.4: Measured H_{T} distribution in events with two or more b-tagged jets for the low H_{T} selection. The predicted H_{T} distribution predicted from the one b-tagged bin scaled to the predicted number of events in our signal region is also shown. We show our benchmark model MC distribution as well. Only statistical uncertainties are shown.

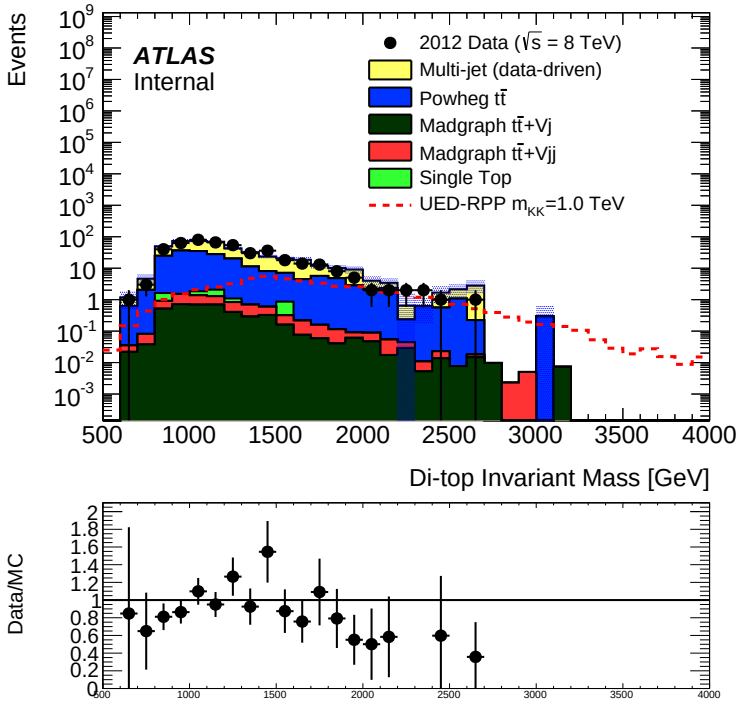

Figure 15.5: Measured di-top invariant mass distribution in events with two or more b-tagged jets for the low H_{T} selection. The predicted di-top invariant mass distribution predicted from the one b-tagged bin scaled to the predicted number of events in our signal region is also shown. We show our benchmark model MC distribution as well. Only statistical uncertainties are shown.

we show the di-top invariant mass distributions for the low-H_{T} selection in figures 15.5 and 15.6, while we show the same distributions for the highH_{T} selection in figures 15.7 and 15.8. There is very good agreement across the entire range of the invariant mass to within statistical uncertainties. The systematic uncertainties are not shown in these distributions.

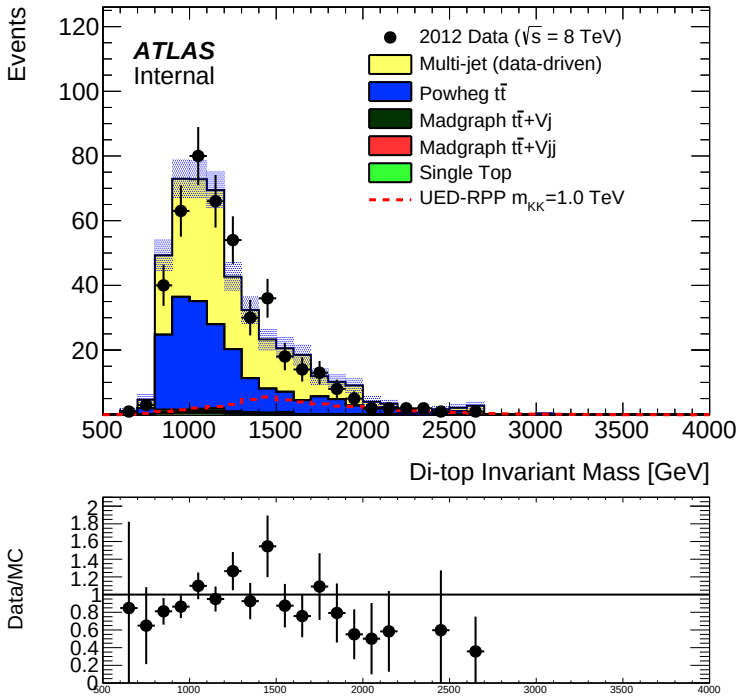

Figure 15.6: Measured di-top invariant mass distribution in events with two or more b-tagged jets for the low H_{T} selection. The predicted di-top invariant mass distribution predicted from the one b-tagged bin scaled to the predicted number of events in our signal region is also shown. We show our benchmark model MC distribution as well. Only statistical uncertainties are shown.

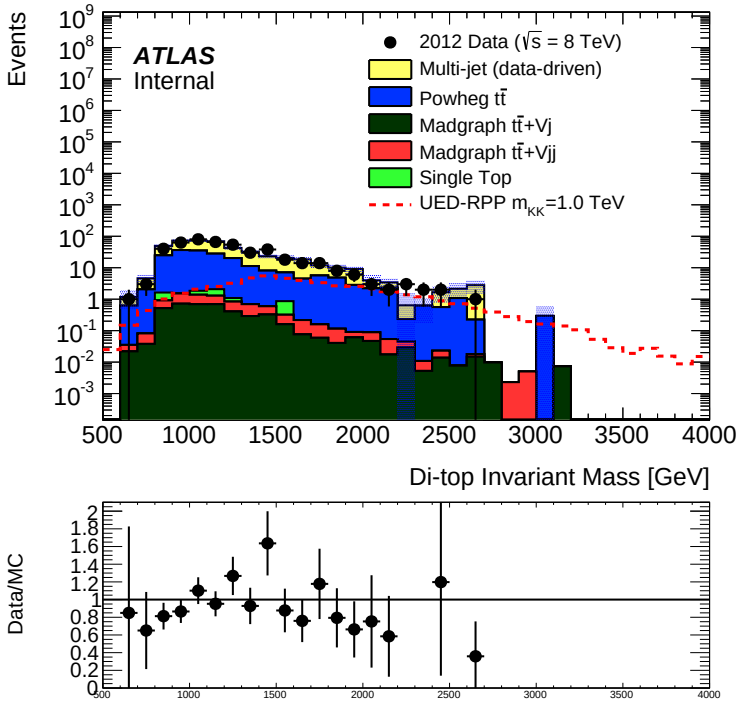

Figure 15.7: Measured di-top invariant mass distribution in events with two or more b-tagged jets for the low H_{T} selection. The predicted di-top invariant mass distribution predicted from the one b-tagged bin scaled to the predicted number of events in our signal region is also shown. We show our benchmark model MC distribution as well. Only statistical uncertainties are shown.

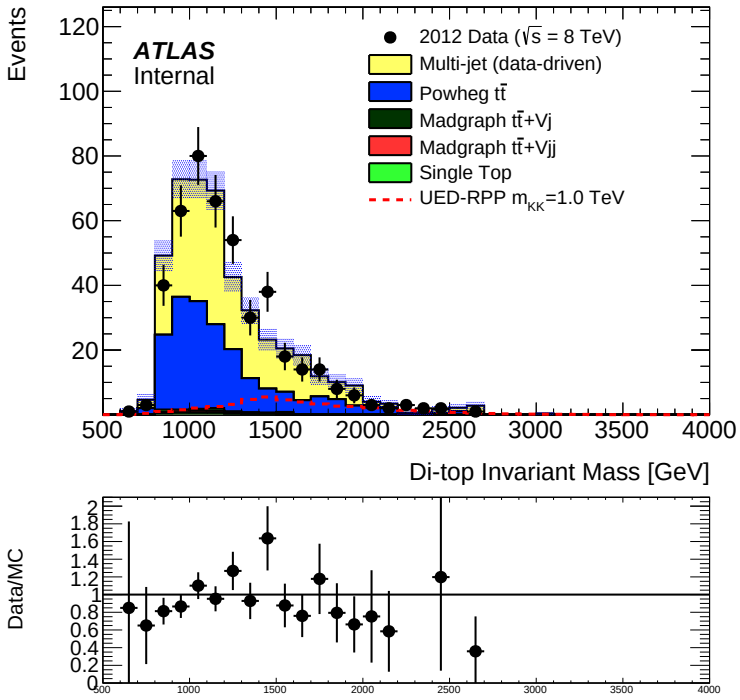

Figure 15.8: Measured di-top invariant mass distribution in events with two or more b-tagged jets for the low H_{T} selection. The predicted di-top invariant mass distribution predicted from the one b-tagged bin scaled to the predicted number of events in our signal region is also shown. We show our benchmark model MC distribution as well. Only statistical uncertainties are shown.

15.2 Signal Yields

Our signal yields are shown in Table 15.4 for the low-H_{T} selection and in Table 15.5 for the high-H_{T} selection. Given that we estimate $13.04 \pm 3.15^{+3.925}_{-4.751}$ background events for the low-H_{T} selection, we might expect to have sensitivity to the 2UED-RPP model somewhere in between 1.10 TeV and 1.15 TeV. For the high-H_{T} selection with $5.024 \pm 1.918^{+1.753}_{-2.971}$ estimated background events, we could potentially have even more reach up last 1.15 TeV. These are just estimates, however. Ws show true estimated sensitivities in the next section which takes into account statistical as well as systematic uncertainties. The Sgluon, contact interaction as well as Standard Model 4-top yields are also shown, however we do not estimate their sensitivity in this thesis.

	Region			
MC Sample	CR-2T-IsoB (A)	CR-2T-IsoB (B)	CR-2T-IsoB (C)	SR-2T-IsoB (D)
2UED-RPP				
m_{KK} = 0.60 TeV	107.2± 5.0439	203.29± 6.9359	2674.5± 21.245	1003± 13.194
m_{KK} = 0.80 TeV	36.141± 0.89519	15.903± 0.59101	187.98± 1.7047	308.39± 2.2006
m_{KK} = 1.00 TeV	7.052± 0.14444	0.80097± 0.048033	7.6161± 0.12558	49.134± 0.3242
m_{KK} = 1.05 TeV	4.513± 0.08688	0.3872± 0.025426	3.2498± 0.061809	29.511± 0.18954
m_{KK} = 1.10 TeV	2.9226± 0.053865	0.1664± 0.012524	1.4437± 0.03163	17.159± 0.11106
m_{KK} = 1.15 TeV	1.7641± 0.031424	0.077282± 0.0065721	0.64511± 0.015886	9.9387± 0.063677
m_{KK} = 1.20 TeV	1.05± 0.017922	0.033135± 0.0030947	0.28414± 0.0078302	5.6896± 0.035777
m_{KK} = 1.10 TeV	0.66789± 0.010991	0.016585± 0.0016745	0.12506± 0.0039333	3.1704± 0.020416
Sgluon				
m_{σ} = 0.4 TeV	0± 0	69.369± 19.353	980.15± 59.096	35.444± 11.965
m_{σ} = 0.5 TeV	4.9415± 2.3734	22.048± 4.7727	367.39± 17.41	22.667± 4.4019
m_{σ} = 0.6 TeV	0.81822± 0.49682	16.536± 2.242	201.88± 6.7532	15.741± 1.8612
m_{σ} = 0.8 TeV	1.1482± 0.19624	4.0939± 0.39403	60.56± 1.216	11.479± 0.53983
m_{σ} = 1.0 TeV	0.71198± 0.061167	0.70761± 0.059507	10.177± 0.18943	6.0965± 0.14816
m_{σ} = 1.25 TeV	0.19494± 0.01045	0.056219± 0.0054728	0.67352± 0.016201	1.654± 0.025465
Contact Interaction	1.5949± 0.11095	2.79± 0.14828	33.057± 0.43259	11.691± 0.26128
Standard Model 4-top	0.0093482± 0.001473	0.052948± 0.0035495	0.56627± 0.0098251	0.086057± 0.0038069

Table 15.4: Signal estimates for the 2T-IsoB channels in the low H_{T} region ($H_{\mathrm{T}} >$ 2.00 TeV in regions A and D, $H_{\mathrm{T}} \leq 2.00$ in regions B and C)

	Region			
MC Sample	CR-2T-IsoB (A)	CR-2T-IsoB (B)	CR-2T-IsoB (C)	SR-2T-IsoB (D)
2UED-RPP				
$m_{KK} = 0.60$ TeV	58.563± 3.7291	251.92± 7.7228	3208.4± 23.293	469.09± 9.1046
$m_{KK} = 0.80$ TeV	23.762± 0.72535	28.283± 0.79027	312.36± 2.1963	184.01± 1.7102
$m_{KK} = 1.00$ TeV	5.8609± 0.13171	1.992± 0.076319	17.002± 0.18804	39.748± 0.29243
$m_{KK} = 1.05$ TeV	3.9313± 0.081178	0.96896± 0.040059	7.9777± 0.097057	24.783± 0.17414
$m_{KK} = 1.10$ TeV	2.601± 0.05085	0.48802± 0.021738	3.6999± 0.050911	14.903± 0.10365
$m_{KK} = 1.15$ TeV	1.6224± 0.030164	0.219± 0.01099	1.718± 0.026041	8.8659± 0.060241
$m_{KK} = 1.20$ TeV	0.98301± 0.017363	0.1001± 0.0054118	0.77753± 0.012965	5.1962± 0.034252
$m_{KK} = 1.10$ TeV	0.63142± 0.010694	0.053058± 0.0030405	0.34081± 0.0065288	2.9546± 0.01974
Sgluon				
$m_{\sigma} = 0.4$ TeV	0± 0	69.369± 19.353	1008.8± 60.142	6.7658± 4.2903
$m_{\sigma} = 0.5$ TeV	2.5955± 1.8406	24.394± 5.0024	381.61± 17.686	8.4492± 3.1131
$m_{\sigma} = 0.6$ TeV	0.36843± 0.27937	16.986± 2.2793	211.82± 6.9067	5.7982± 1.1692
$m_{\sigma} = 0.8$ TeV	0.73326± 0.15942	4.5088± 0.41031	67.735± 1.2885	4.304± 0.33125
$m_{\sigma} = 1.0$ TeV	0.42899± 0.047704	0.9906± 0.070759	13.45± 0.21819	2.8235± 0.10113
$m_{\sigma} = 1.25$ TeV	0.14613± 0.0089756	0.10502± 0.0076548	1.2428± 0.022019	1.0847± 0.020643
Contact Interaction	1.0601± 0.089875	3.3247± 0.16193	38.712± 0.46861	6.0365± 0.18923
Standard Model 4-top	0.0036903± 0.00089901	0.058606± 0.0037363	0.61208± 0.010206	0.040251± 0.0026202

Table 15.5: Signal estimates for the 2T-IsoB channels in the high H_{T} region ($H_{\mathrm{T}} >$ 2.25 TeV in regions A and D, $H_{\mathrm{T}} \leq 2.25$ in regions B and C)

15.3 Estimated Sensitivities

15.3.1 Statistical treatment of results

In order to look for an excess of events in our signal regions, we effectively break down the analysis into two single-binned likelihood search, one for the low $H_{\rm T}$ region and one for the high$H_{\rm T}$ region. We employ a hybrid Bayesian-Frequentist approach that is based on Confidence Levels (CLs). The log-likelihood ratio (LLR) , as defined below, is used as our test statistic.

$$LLR = -2\ln\frac{\mathcal{L}(data|H_1)}{\mathcal{L}(data|H_0)}, \tag{15.1}$$

where H_1 denotes the signal plus background hypothesis while H_0 denotes the background only (null) hypothesis. Since we are only considering one channel and a single binned study, for a given hypothesis, the combined log-likelihood is highly simplified to,

$$-2\ n\ \ln\mu - \mu + \sum_{k=1}^{N_{par}} \theta_k^2, \tag{15.2}$$

where n is the number of events observed in data. μ is the given by $\alpha s(\theta) + b(\theta)$, where $s(\theta)$ is the expected number of signal events and $b(\theta)$ is the expected number of background events. α is a scaling parameter applied to the signal to test the sensitivity. Both the signal and background are function of nuisance parameters, θ. In the calculation of the LLR, the signal+background as well as the background only hypothesis are minimized separately over the nuisance parameters. This procedure extends what is commonly called the LEP technique [61]

Given the $LLRs$, two p-values are computed using pseudoexperiments, namely

those for the signal+background hypothesis as well as the background only hypothesis, are

$$1 - \mathrm{CL}_b = p(LLR \leq LLR_{obs}|H_0), \tag{15.3}$$

$$\mathrm{CL}_{s+b} = p(LLR \geq LLR_{obs}|H_1). \tag{15.4}$$

$$\tag{15.5}$$

We interpret the former p-value as the probability that a background fluctuation (modulo the presence of a signal), provides a LLR value that is as signal+plus+background like or more than that observed in the data. The latter is the probability of a downward fluctuation of of a s+b in the data. The quantity of interest, however, is $\mathrm{CL}_s = \mathrm{CL}_{s+b}/\mathrm{CL}_b$. If $\mathrm{CL}_s < 0.05$ for a particular choice of signal+background hypothesis H_1, then we can exclude that particular model at the 95% confidence level. The hypothesis H_1 is defined in terms of the m_{KK} where $R = \sigma(t\bar{t}t\bar{t})/\sigma^{th}(t\bar{t}t\bar{t})$. If $R^{exp}_{95\%} < 1$, that particular value of m_{KK} is expected to be excluded at 95% C.L.. Similarly, if $R^{ons}_{95\%} < 1$, then the particular value of m_{KK} is considered experimentally excluded at 95% C.L..

15.3.2 2UED-RPP

Using the statistical method described above, we can estimate the potential sensitivity to each signal point. Figure 15.9 shows the 95% CLs potential exclusion sensitivity without including any systematics. The low-H_{T} selection has the potential to exclude 2UED-RPP mass scales up to close to 1.13 TeV, while the high-H_{T} selection has the potential to exclude masses up to 1.16 TeV. Once we include systematics, the

expected potential for exclusion drops, but not significantly, to around 1.06 TeV for both the low- and high-H_{T} selections.

15.3.3 Sgluons

Estimated sensitivities to the Sgluon models are currently under investigation.

15.3.4 Contact Interaction and Standard Model Four-tops

Estimated sensitivities to the Contact Interaction and Standard Model 4-top models are currently under investigation.

15.4 Conclusions

In this thesis, we presented a novel, substructure based technique for tagging boosted top-quarks. Using these methods, we completed a search for physics beyond the Standard Model in the four-top quark final state. While we have no un-blinded the data in our signal region yet, we have presented estimated backgrounds for two selection regions including both statistical as well as systematic uncertainties on those estimates. Using these, as well as estimated signal yields for various models, we predict that in the absence of any excess or deficit of events in the measured data, we should be able to exclude the 2UED-RPP model up to $\mathrm{m_{KK}} = 1.06$ TeV if we include all of the systematic uncertainties and $\mathrm{m_{KK}} = 1.16$ TeV if we do not take into account those same uncertainties. These both are significant improvements on the current exclusion limit of 900 GeV.

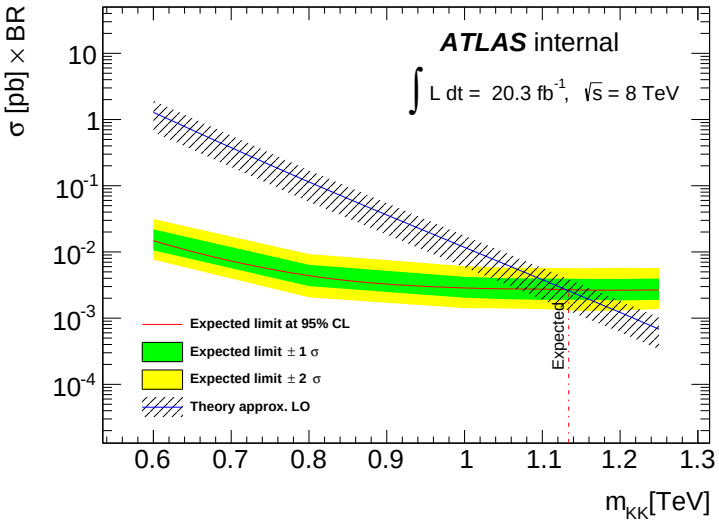

(a)

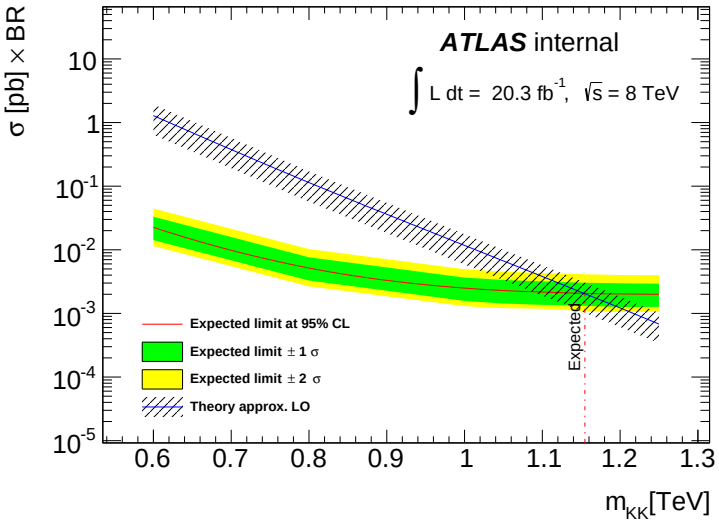

(b)

Figure 15.9: Expected exclusion of the 2UED-RPP model at 95% C.L. without systematic uncertainties. We expect the high H_{T} selection to perform better than the low H_{T}, giving an expected exclusion of close to 1.16 TeV, significantly better than the current limit of 900 GeV.

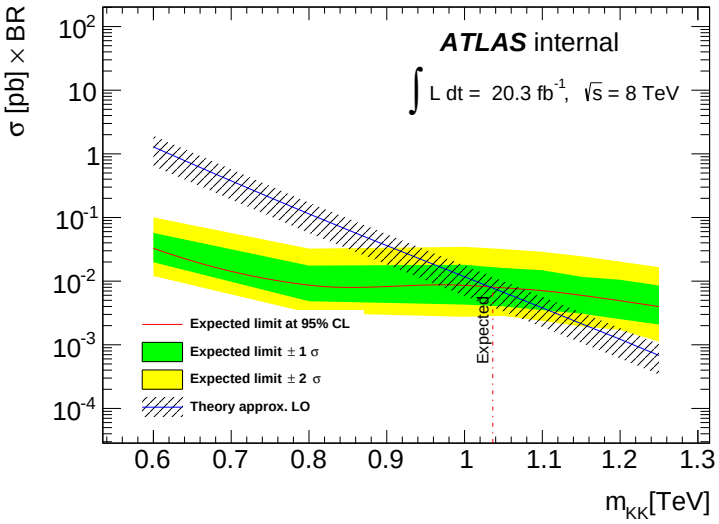

(a)

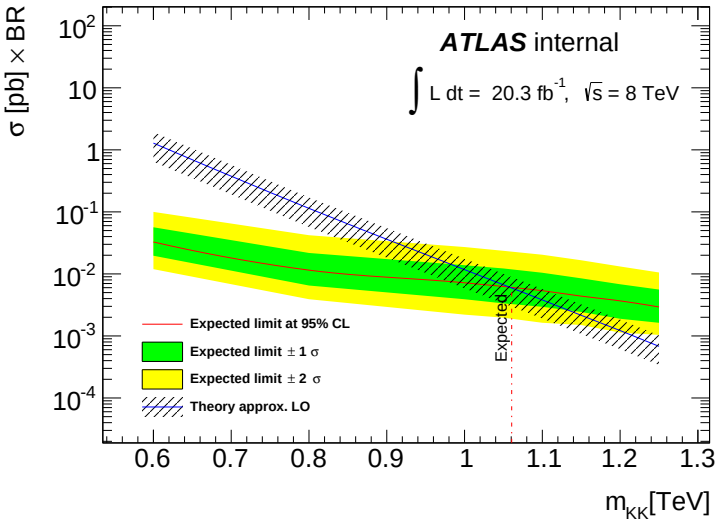

(b)

Figure 15.10: Expected exclusion of the 2UED-RPP model at 95% C.L. including systematic uncertainties. We expect the high H_{T} selection to perform better than the low H_{T}, giving an expected exclusion of greater than 1.06 TeV, significantly better than the current limit of 900 GeV.

Bibliography

[1] Search for anomalous production of events with same-sign dileptons and b jets in 14.3 fb^{-1} of pp collisions at $\sqrt{s} = 8$ tev with the atlas detector. Technical Report ATLAS-CONF-2013-051, CERN, Geneva, May 2013.

[2] Summary of ATLAS Pythia 8 tunes. Technical Report ATL-PHYS-PUB-2012-003, 2012.

[3] Jet energy scale and its systematic uncertainty in proton-proton collisions at sqrt(s)=7 TeV in ATLAS 2010 data. Technical Report ATLAS-CONF-2011-032, 2011.

[4] Commissioning of the ATLAS high-performance b-tagging algorithms in the 7 TeV collision data. Technical Report ATLAS-CONF-2011-102, 2011.

[5] Selection of jets produced in proton-proton collisions with the ATLAS detector using 2011 data. Technical Report ATLAS-CONF-2012-020, 2012.

[6] Studies of the impact and mitigation of pile-up on large-R and groomed jets in ATLAS at $\sqrt{s} = 7$ TeV. Technical Report ATLAS-CONF-2012-066, 2012.

[7] Performance of large-R jets and jet substructure reconstruction with the ATLAS detector. Technical Report ATLAS-CONF-2012-065, 2012.

[8] Pile-up corrections for jets from proton-proton collisions at $\sqrt{s} = 7$TeV in ATLAS in 2011. Technical Report ATLAS-CONF-2012-064, 2012.

[9] Georges Aad et al. Observation of a new particle in the search for the Standard Model Higgs boson with the ATLAS detector at the LHC. *Phys.Lett.*, B716:1–29, 2012.

[10] Georges Aad et al. Jet energy measurement with the ATLAS detector in proton-proton collisions at $\sqrt{s} = 7$ TeV. *Eur.Phys.J.*, C73:2304, 2013.

[11] Georges Aad et al. Performance of jet substructure techniques for large-R jets in proton-proton collisions at $\sqrt{s} = 7$ TeV using the ATLAS detector. 2013.

[12] T. Aaltonen et al. Direct Top-Quark Width Measurement CDF. *Phys.Rev.Lett.*, 105:232003, 2010.

[13] S. Abachi et al. Search for high mass top quark production in p anti-p collisions at s**(1/2) = 1.8-TeV. *Phys. Rev. Lett.*, 74:2422–2426, 1995.

[14] E. Abat et al. The ATLAS Transition Radiation Tracker (TRT) proportional drift tube: Design and performance. *JINST*, 3:P02013, 2008.

[15] F. Abe et al. Observation of top quark production in anti-p p collisions. *Phys. Rev. Lett.*, 74:2626–2631, 1995.

[16] S. Agostinelli et al. GEANT4: A Simulation toolkit. *Nucl.Instrum.Meth.*, A506:250–303, 2003.

[17] Johan Alwall, Pierre Artoisenet, Simon de Visscher, Claude Duhr, Rikkert Frederix, et al. New Developments in MadGraph/MadEvent. *AIP Conf.Proc.*, 1078:84–89, 2009. 6 pages, 3 figures. Plenary talk given at SUSY08, Seoul, South Korea, June 2008. To appear in the proceedings.

[18] Johan Alwall, A. Ballestrero, P. Bartalini, S. Belov, E. Boos, et al. A Standard format for Les Houches event files. *Comput.Phys.Commun.*, 176:300–304, 2007.

[19] Johan Alwall, Pavel Demin, Simon de Visscher, Rikkert Frederix, Michel Herquet, et al. MadGraph/MadEvent v4: The New Web Generation. *JHEP*, 0709:028, 2007.

[20] Johan Alwall, Michel Herquet, Fabio Maltoni, Olivier Mattelaer, and Tim Stelzer. MadGraph 5 : Going Beyond. *JHEP*, 1106:128, 2011.

[21] P. Amaral et al. Hadronic shower development in iron scintillator tile calorimetry. *Nucl.Instrum.Meth.*, A443:51–70, 2000.

[22] Thomas Appelquist, Hsin-Chia Cheng, and Bogdan A. Dobrescu. Bounds on universal extra dimensions. *Phys. Rev.*, D64:035002, 2001.

[23] Thomas Appelquist, Bogdan A. Dobrescu, Eduardo Ponton, and Ho-Ung Yee. Proton stability in six dimensions. *Phys. Rev. Lett.*, 87:181802, 2001.

[24] Thomas Appelquist, Bogdan A. Dobrescu, Eduardo Ponton, and Ho-Ung Yee. Neutrinos vis-a-vis the six-dimensional standard model. *Phys. Rev.*, D65:105019, 2002.

[25] E. Bergeaas, C. Issever, K. Jon-And, B.T. King, K. Lohwasser, et al. Local Hadronic Calibration of Single Pion Data from the Combined ATLAS Testbeam of 2004. Technical Report ATL-CAL-PUB-2007-001, 2007.

[26] J. Beringer et al. Review of Particle Physics (RPP). *Phys.Rev.*, D86:010001, 2012.

[27] Zvi Bern, Kemal Ozeren, Lance J. Dixon, Stefan Hoeche, Fernando Febres Cordero, et al. High multiplicity processes at NLO with BlackHat and Sherpa. *PoS*, LL2012:018, 2012.

[28] Gianfranco Bertone, Dan Hooper, and Joseph Silk. Particle dark matter: Evidence, candidates and constraints. *Phys.Rept.*, 405:279–390, 2005.

[29] G. Bevilacqua and M. Worek. Constraining BSM Physics at the LHC: Four top final states with NLO accuracy in perturbative QCD. *JHEP*, 1207:111, 2012.

[30] Daniel Boline. Measurement of the W Boson Mass and Width at the D0 Experiment. 2011. 8 pages, Proceedings of the DPF-2011 Conference, Providence, RI, August 8-13, 2011.

[31] Oleg Brandt. Measurements of the Properties of the Top Quark. 2011. Proceedings for Moriond QCD 2011 conference, 4 pages, 5 fig.

[32] Gustavo Burdman, Bogdan A. Dobrescu, and Eduardo Ponton. Resonances from two universal extra dimensions. *Phys. Rev.*, D74:075008, 2006.

[33] Gustavo Burdman, Bogdan A. Dobrescu, and Eduardo Ponton. Six-dimensional gauge theory on the chiral square. *JHEP*, 02:033, 2006.

[34] J.M. Butterworth, B.E. Cox, and Jeffrey R. Forshaw. WW scattering at the CERN LHC. *Phys.Rev.*, D65:096014, 2002.

[35] Giacomo Cacciapaglia, Roberto Chierici, Aldo Deandrea, Luca Panizzi, Stephane Perries, et al. Four tops on the real projective plane at LHC. *JHEP*, 1110:042, 2011.

[36] Giacomo Cacciapaglia, Aldo Deandrea, and Jeremie Llodra-Perez. A Dark Matter candidate from Lorentz Invariance in 6D. *JHEP*, 1003:083, 2010.

[37] Hsin-Chia Cheng, Jonathan L. Feng, and Konstantin T. Matchev. Kaluza-Klein dark matter. *Phys.Rev.Lett.*, 89:211301, 2002.

[38] Hsin-Chia Cheng, Konstantin T. Matchev, and Martin Schmaltz. Bosonic supersymmetry? Getting fooled at the CERN LHC. *Phys. Rev.*, D66:056006, 2002.

[39] The ATLAS collaboration. Performance of boosted top quark identification in 2012 ATLAS data. Technical Report ATLAS-CONF-2013-084, 2013.

[40] The ATLAS collaboration. Pile-up subtraction and suppression for jets in ATLAS. Technical Report ATLAS-CONF-2013-083, 2013.

[41] Glen Cowan, Kyle Cranmer, Eilam Gross, and Ofer Vitells. Asymptotic formulae for likelihood-based tests of new physics. *Eur.Phys.J.*, C71:1554, 2011.

[42] AseshKrishna Datta, Kyoungchul Kong, and Konstantin T. Matchev. Minimal Universal Extra Dimensions in CalcHEP/CompHEP. *New J. Phys.*, 12:075017, 2010.

[43] Priscila de Aquino, William Link, Fabio Maltoni, Olivier Mattelaer, and Tim Stelzer. ALOHA: Automatic Libraries Of Helicity Amplitudes for Feynman diagram computations. 2011.

[44] Celine Degrande, Claude Duhr, Benjamin Fuks, David Grellscheid, Olivier Mattelaer, et al. UFO - The Universal FeynRules Output. 2011.

[45] Celine Degrande, Jean-Marc Gerard, Christophe Grojean, Fabio Maltoni, and Geraldine Servant. Non-resonant New Physics in Top Pair Production at Hadron Colliders. *JHEP*, 1103:125, 2011.

[46] Bogdan A. Dobrescu, Dan Hooper, Kyoungchul Kong, and Rakhi Mahbubani. Spinless photon dark matter from two universal extra dimensions. *JCAP*, 0710:012, 2007.

[47] Bogdan A. Dobrescu, Kyoungchul Kong, and Rakhi Mahbubani. Leptons and photons at the LHC: Cascades through spinless adjoints. *JHEP*, 07:006, 2007.

[48] Bogdan A. Dobrescu, Kyoungchul Kong, and Rakhi Mahbubani. Massive color-octet bosons and pairs of resonances at hadron colliders. *Phys. Lett.*, B670:119–123, 2008.

[49] Bogdan A. Dobrescu and Eduardo Ponton. Chiral compactification on a square. *JHEP*, 03:071, 2004.

[50] Bogdan A. Dobrescu and Erich Poppitz. Number of fermion generations derived from anomaly cancellation. *Phys. Rev. Lett.*, 87:031801, 2001.

[51] Hideto Dohi and Kin-ya Oda. Universal Extra Dimensions on Real Projective Plane. *Phys. Lett.*, B692:114–120, 2010.

[52] R. Keith Ellis, W. James Stirling, and B. R. Webber. *QCD and Collider Physics*, volume 8. Cambridge University Press, 1996.

[53] Stefano Frixione, Fabian Stoeckli, Paolo Torrielli, Bryan R. Webber, and Chris D. White. The MCaNLO 4.0 Event Generator. 2010.

[54] Kirtiman Ghosh and Anindya Datta. Phenomenology of spinless adjoints in two Universal Extra Dimensions. *Nucl. Phys.*, B800:109–126, 2008.

[55] Stefan Gieseke, Christian Rohr, and Andrzej Siodmok. Colour reconnections in Herwig++. *Eur.Phys.J.*, C72:2225, 2012.

[56] T. Gleisberg, Stefan. Hoeche, F. Krauss, M. Schonherr, S. Schumann, et al. Event generation with SHERPA 1.1. *JHEP*, 0902:007, 2009.

[57] D. Griffiths. *Introduction to Elementary Particles*. John Wiley & Sons, New York, USA, 1987.

[58] J.L. Holzbauer and for the ATLAS Collaboration. Measurement of Single-top Quark Production with the ATLAS Detector. 2011.

[59] Dan Hooper and Stefano Profumo. Dark matter and collider phenomenology of universal extra dimensions. *Phys.Rept.*, 453:29–115, 2007.

[60] Jyoti Joshi and Suman Beri. Observation of single top quark production at D0 using Bayesian neural networks. *Conf.Proc.*, C0908171:431–433, 2009.

[61] Thomas Junk. Confidence level computation for combining searches with small statistics. *Nucl.Instrum.Meth.*, A434:435–443, 1999.

[62] Borut Paul Kersevan and Elzbieta Richter-Was. The Monte Carlo event generator AcerMC versions 2.0 to 3.8 with interfaces to PYTHIA 6.4, HERWIG 6.5 and ARIADNE 4.1. *Comput.Phys.Commun.*, 184:919–985, 2013.

[63] Wolfgang Kilian, Thorsten Ohl, and Jurgen Reuter. WHIZARD: Simulating Multi-Particle Processes at LHC and ILC. *Eur.Phys.J.*, C71:1742, 2011.

[64] Makoto Kobayashi and Toshihide Maskawa. CP Violation in the Renormalizable Theory of Weak Interaction. *Prog. Theor. Phys.*, 49:652–657, 1973.

[65] Graham D. Kribs, Erich Poppitz, and Neal Weiner. Flavor in supersymmetry with an extended R-symmetry. *Phys.Rev.*, D78:055010, 2008.

[66] David Krohn, Jesse Thaler, and Lian-Tao Wang. Jet Trimming. *JHEP*, 1002:084, 2010.

[67] Hung-Liang Lai, Marco Guzzi, Joey Huston, Zhao Li, Pavel M. Nadolsky, et al. New parton distributions for collider physics. *Phys.Rev.*, D82:074024, 2010.

[68] J. Lueck. Observation of single top-quark production with the CDF II experiment. *Il Nuovo Cimento*, 2010.

[69] Wolfgang Lukas. Fast Simulation for ATLAS: Atlfast-II and ISF. *J.Phys.Conf.Ser.*, 396:022031, 2012.

[70] The Luminosity Group. Preliminary Luminosity Determination in pp Collisions at sqrt(s) = 8 TeV using the ATLAS Detector in 2012. Technical Report ATL-COM-LUM-2012-013, CERN, Geneva, Nov 2012.

[71] C. Macesanu, C. D. McMullen, and S. Nandi. Collider implications of universal extra dimensions. *Phys. Rev.*, D66:015009, 2002.

[72] Cosmin Macesanu. The phenomenology of universal extra dimensions at hadron colliders. *Int. J. Mod. Phys.*, A21:2259–2296, 2006.

[73] Fabio Maltoni and Tim Stelzer. MadEvent: Automatic event generation with MadGraph. *JHEP*, 0302:027, 2003.

[74] Aneesh V. Manohar and Mark B. Wise. Flavor changing neutral currents, an extended scalar sector, and the Higgs production rate at the LHC. *Phys. Rev.*, D74:035009, 2006.

[75] Patrick Meade and Matthew Reece. BRIDGE: Branching ratio inquiry / decay generated events. 2007.

[76] Anibal D. Medina and Eduardo Ponton. Warped Universal Extra Dimensions. *JHEP*, 06:009, 2011.

[77] Mauro Moretti, Thorsten Ohl, and Jurgen Reuter. O'Mega: An Optimizing matrix element generator. 2001.

[78] K. Nakamura et al. Review of particle physics. *J. Phys.*, G37:075021, 2010, and 2011 partial update for the 2012 edition.

[79] Carlo Oleari. The POWHEG-BOX. *Nucl.Phys.Proc.Suppl.*, 205-206:36–41, 2010.

[80] Tilman Plehn and Tim M.P. Tait. Seeking Sgluons. *J.Phys.*, G36:075001, 2009.

[81] Eduardo Ponton and Erich Poppitz. Casimir energy and radius stabilization in five and six dimensional orbifolds. *JHEP*, 06:019, 2001.

[82] Eduardo Ponton and Lin Wang. Radiative effects on the chiral square. *JHEP*, 11:018, 2006.

[83] A. Pukhov. CalcHEP 2.3: MSSM, structure functions, event generation, batchs, and generation of matrix elements for other packages. 2004.

[84] J. Pumplin, D.R. Stump, J. Huston, H.L. Lai, Pavel M. Nadolsky, et al. New generation of parton distributions with uncertainties from global QCD analysis. *JHEP*, 0207:012, 2002.

[85] Elzbieta Richter-Was, D. Froidevaux, and Luc Poggioli. ATLFAST 2.0 a fast simulation package for ATLAS. Technical Report ATL-PHYS-98-131, 1998.

[86] Geraldine Servant and Timothy M.P. Tait. Is the lightest Kaluza-Klein particle a viable dark matter candidate? *Nucl.Phys.*, B650:391–419, 2003.

[87] Mikhail Shaposhnikov. Neutrino physics within and beyond the three flavour oscillation. *J.Phys.Conf.Ser.*, 408:012015, 2013.

[88] Torbjorn Sjostrand, Stephen Mrenna, and Peter Z. Skands. PYTHIA 6.4 Physics and Manual. *JHEP*, 0605:026, 2006.

[89] Torbjorn Sjostrand, Stephen Mrenna, and Peter Z. Skands. A Brief Introduction to PYTHIA 8.1. *Comput.Phys.Commun.*, 178:852–867, 2008.

[90] Peter Zeiler Skands. Tuning Monte Carlo Generators: The Perugia Tunes. *Phys.Rev.*, D82:074018, 2010.

[91] Jennifer M. Smillie and Bryan R. Webber. Distinguishing Spins in Supersymmetric and Universal Extra Dimension Models at the Large Hadron Collider. *JHEP*, 10:069, 2005.

[92] Jesse Thaler and Ken Van Tilburg. Identifying Boosted Objects with N-subjettiness. *JHEP*, 1103:015, 2011.

Appendices

Appendix A

Details of the 2UED Chiral Square model

The information in this chapter was used in the development of the FeynRules implementation of the 2UED Chiral Square new physics model. The model is available upon request from the author Peter Manning at pmmannin@syr.edu.

A.1 Kaluza-Klein Field Expansions

The six-dimensional fields can be decomposed into a sum of products of KK fields that are a function x^μ and KK functions that are a function of x^4 and x^5.

A.1.1 Gauge fields

Both Abelian and non-Abelian gauge fields, as given in [33], decompose as

$$A_\mu(x^\nu, x^4, x^5) = \frac{1}{\pi R}\left[A_\mu^{(0,0)}(x^\nu) + \sum_{j\geq 1}\sum_{k\geq 0} f_0^{(j,k)}(x^4, x^5) A_\mu^{(j,k)}(x^\nu)\right] \tag{A.1}$$

where f_n are defined as

$$\begin{aligned} f_{0,2}^{(j,k)}(x^4, x^5) &= \frac{1}{1+\delta_{j,0}}\left[\cos\left(\frac{jx^4 + kx^5}{R}\right) \pm \cos\left(\frac{kx^4 - jx^5}{R}\right)\right], \\ f_{1,3}^{(j,k)}(x^4, x^5) &= i\sin\left(\frac{jx^4 + kx^5}{R}\right) \mp \sin\left(\frac{kx^4 - jx^5}{R}\right). \end{aligned} \tag{A.2}$$

There are two additional gauge field expansions to consider, A_4 and A_5, the components of the gauge fields in the extra dimensions. For convenience, these fields can be re-written as $A_\pm = A_4 \pm \imath A_5$. Their decompositions are

$$\begin{aligned} A_+(x^\nu, x^4, x^5) &= -\frac{1}{\pi R}\left[\sum_{j\geq 1}\sum_{k\geq 0} f_3^{(j,k)}(x^4, x^5) A_+^{(j,k)}(x^\nu)\right], \\ A_-(x^\nu, x^4, x^5) &= \frac{1}{\pi R}\left[\sum_{j\geq 1}\sum_{k\geq 0} f_1^{(j,k)}(x^4, x^5) A_-^{(j,k)}(x^\nu)\right]. \end{aligned} \tag{A.3}$$

While these re-definitions of the extra dimensional gauge components are convenient, we need to make one further definition in terms of the physical scalar fields, A_H and A_G, as

$$A_\pm^{(j,k)} = r_{j,\pm k}\left(A_H^{(j,k)} \mp i A_G^{(j,k)}\right), \tag{A.4}$$

where

$$r_{j,\pm k} = \frac{j \pm ik}{\sqrt{j^2 + k^2}}. \tag{A.5}$$

Since there needs to be a direct relation between the physical scalar fields and the bare extra dimensional gauge fields A_4 and A_5 (for insertion into the later described Lagrangian), we also show explicitly,

$$\begin{aligned} A_4^{(j,k)} =& \frac{1}{2}(A_+^{(j,k)} + A_-^{(j,k)}), \\ A_5^{(j,k)} =& -\frac{i}{2}(A_+^{(j,k)} - A_-^{(j,k)}). \end{aligned} \tag{A.6}$$

A.1.2 Scalar fields

As derived in [33], the scalar field decomposition are given as,

$$\Phi(x^\nu, x^4, x^5) = \frac{1}{\pi R}\left[\Phi^{(0,0)}(x^\nu) + \sum_{j\geq 1}\sum_{k\geq 0} f_0^{(j,k)}(x^4, x^5)\Phi^{(j,k)}(x^\nu)\right]. \tag{A.7}$$

This scalar expansion becomes important when describing the Higgs interaction in the next section.

A.1.3 Fermion fields

For our choice of 6D chiralities, $\mathcal{Q}_+, \mathcal{U}_-, \mathcal{D}_-, \mathcal{L}_+, \mathcal{E}_-, \mathcal{N}_-$ [50], and the requirement that a 6D fermion Ψ_+ or Ψ_- in this set each contain only one zero-mode fermion,

the most general decomposition of the fermion fields are [49] [33],

$$\Psi_{+L} = \frac{1}{\pi R}\left[\Psi_{+L}^{(0,0)}(x^\nu) + \sum_{j\geq 1}\sum_{k\geq 0} f_0^{(j,k)}(x^4,x^5)\Psi_{+L}^{(j,k)}(x^\nu)\right]\otimes\begin{pmatrix}1\\ \\ 0\end{pmatrix},$$

$$\Psi_{+R} = -\frac{i}{\pi R}\sum_{j\geq 1}\sum_{k\geq 0} r_{j,k} f_3^{(j,k)}(x^4,x^5)\Psi_{+R}^{(j,k)}(x^\nu)\otimes\begin{pmatrix}0\\ \\ 1\end{pmatrix}, \tag{A.8}$$

and

$$\Psi_{-L} = -\frac{i}{\pi R}\sum_{j\geq 1}\sum_{k\geq 0} r_{j,k} f_3^{(j,k)}(x^4,x^5)\Psi_{-L}^{(j,k)}(x^\nu)\otimes\begin{pmatrix}0\\ \\ 1\end{pmatrix},$$

$$\Psi_{-R} = \frac{1}{\pi R}\left[\Psi_{-R}^{(0,0)}(x^\nu) + \sum_{j\geq 1}\sum_{k\geq 0} f_0^{(j,k)}(x^4,x^5)\Psi_{-R}^{(j,k)}(x^\nu)\right]\otimes\begin{pmatrix}1\\ \\ 0\end{pmatrix}, \tag{A.9}$$

where $\Psi_{\pm L,R} \equiv P_{L,R}P_{\pm}\Psi$ with $P_{L,R}$ the 4D projection operator and $P_{\pm}$ the 6D projection operator that will be defined more explicitly in the next section. With these KK field decompositions we are now in a position to describe the U1, SU2, SU3, and fermion interactions.

A.2 2UED Lagrangian

The total 6D action can be expressed as the sum of five physically distinct pieces,

$$\begin{aligned} S = \int d^4x \int_0^{\pi R} dx^4 \int_0^{\pi R} dx^5 \{ & \mathcal{L}_{Gauge} + \mathcal{L}_{Fermions} + \delta(x_4)\delta(\pi R - x_5)\mathcal{L}_{Violating,1} \\ & + [\delta(x_4)\delta(x_5) + \delta(\pi R - x_4)\delta(\pi R - x_5)]\mathcal{L}_{Violating,2} \\ & + \mathcal{L}_{Higgs} + \mathcal{L}_{Yukawa}\}), \end{aligned} \tag{A.10}$$

where $\mathcal{L}_{Gauge}$ contains all U1, SU2 and SU3 terms, $\mathcal{L}_{Fermions}$ describes the KK number preserving interactions of the 6D fermions, $\mathcal{L}_{Violating,1,2}$ include the KK number violating operators and $\mathcal{L}_{Higgs} + \mathcal{L}_{Yukawa}$ include the 6D Higgs and Yukawa terms. While the gauge, fermion and KK number violating terms will be described here, the Yukawa will not. See [33] for a complete description of the Yukawa terms.

A.2.1 $\mathcal{L}_{Gauge}$

The gauge term can be broken down into three groups corresponding to U1, SU2 and SU3, as done in [33]

$$\begin{aligned} \mathcal{L}_{U1} = & -\frac{1}{4}B_{\mu\nu}B^{\mu\nu} - \frac{1}{2\xi}(\partial_\mu B_\mu)^2 + \frac{1}{2}[(\partial_4 B_\mu)^2 + (\partial_5 B_\mu)^2] \\ & + \frac{1}{2}[(\partial_\mu B_4)^2 + (\partial_\mu B_5)^2 - \xi(\partial_4 B_4 + \partial_5 B_5)^2 - (\partial_4 B_5 - \partial_5 B_4)^2] \\ & + \partial_4[B_4 \partial_\mu B^\mu] + \partial_5[B_5 \partial_\mu B^\mu], \end{aligned} \tag{A.11}$$

where $B_{\mu\nu}$ is the standard field strength tensor in four dimensions, ξ is the gauge fixing parameter, B_μ, B_4 and B_5 are as defined in [33] [49] [82]. The SU2 Lagrangian can be

written as,

$$\mathcal{L}_{SU2} = -\frac{1}{4}(W^i_{\mu\nu}W^{i\mu\nu} - 2W^i_{+\mu}W^{i\mu}_{-}) + \frac{1}{8}(W^i_{+-})^2 + \mathcal{L}_{SU2,ghosts}, \tag{A.12}$$

and similarly the SU3 term as,

$$\mathcal{L}_{SU3} = -\frac{1}{4}(G^a_{\mu\nu}G^{a\mu\nu} - 2G^a_{+\mu}G^{a\mu}_{-}) + \frac{1}{8}(G^a_{+-})^2 + \mathcal{L}_{SU3,ghosts}, \tag{A.13}$$

where the field strengths are defined in general for a non-Abelian gauge field A^a_μ with 6D gauge couplings $g_6 = \pi R g_4$ by,

$$\begin{aligned} F^a_{\mu\nu} &= \partial_\mu A^a_\nu - \partial_\nu A^a_\mu + g_6 f^{abc} A^b_\mu A^c_\nu, \\ F^a_{\pm\mu} &= \partial_\pm A^a_\mu - \partial_\mu A^a_\pm + g_6 f^{abc} A^b_\pm A^c_\mu, \\ F^a_{+-} &= \partial_+ A^a_- - \partial_- A^a_+ + g_6 f^{abc} A^b_+ A^c_-. \end{aligned} \tag{A.14}$$

The ghost terms for the non-Abelian gauge field strengths are examined in detail in [33] but not considered in this thesis.

A.2.2 $\mathcal{L}_{Fermions}$

In its most general, six dimensional form, the fermion kinetic term of the total 6D Lagrangian is,

$$i\overline{\Psi}_\pm \Gamma^\alpha D_\alpha \Psi_\pm \tag{A.15}$$

where $\alpha = 0, 1, ..., 5$ and D_α is the 6D covariant derivative and the fields are as defined in eq (A.8) and eq (A.9) and in general on page 179. In this very concise form, eq (A.15) is not very useful, especially if we hope to understand the model in terms of four

dimensional components. Writing eq (A.15) in terms of eq (A.8) and eq (A.9), as well as defining,

$$\Gamma^{\mu} = \gamma^{\mu} \otimes \sigma^{0} = \begin{pmatrix} \gamma^{\mu} & 0 \\ 0 & \gamma^{\mu} \end{pmatrix} \tag{A.16}$$

and,

$$\Gamma^{\pm} = \frac{1}{2}\left(\Gamma^{4} \pm i\Gamma^{5}\right) \tag{A.17}$$

where, utilizing the familiar Dirac γ matrices as well as the σ Pauli matrices,

$$\Gamma^{4,5} = i\gamma^{5} \otimes \sigma^{1,2} = i \begin{pmatrix} 0 & \gamma^{5}, -i\gamma^{5} \\ \gamma^{5}, i\gamma^{5} & 0 \end{pmatrix} \tag{A.18}$$

the result is,

$$i(\overline{\Psi}_{\pm L}\Gamma^{\mu}D_{\mu}\Psi_{\pm L} + \overline{\Psi}_{\pm R}\Gamma^{\mu}D_{\mu}\Psi_{\pm R} + \overline{\Psi}_{\pm L}\Gamma^{\pm}D_{\mp}\Psi_{\pm R} + \overline{\Psi}_{\pm R}\Gamma^{\mp}D_{\pm}\Psi_{\pm L}). \tag{A.19}$$

It may seem strange that we need these $8x8$ matrices in the Lagrangian, but they are necessary in the dimensional reduction from 6D to 4D. More specifically, since the fermion fields are the result of a direct product with a two dimensional vector, it is necessary for the dimension of the anti-commuting matrices to be twice that of the standard dimension four Dirac matrices. We can take this one step further by explicitly substituting $\Psi_{\pm L,R} \equiv P_{L,R}P_{\pm}\Psi$ into eq (A.19) and multiplying the matrices

in eqs (A.16) and (A.18) using the projection identities,

$$P_{\pm} = \frac{1}{2}\left(1 \mp \gamma^5 \otimes \begin{pmatrix} 1 & 0 \\ 0 & -1 \end{pmatrix}\right). \tag{A.20}$$

The resulting Lagrangian is,

$$i(\overline{\Psi}_{\pm L} D_\mu P_L \Psi_{\pm L} + \overline{\Psi}_{\pm R} D_\mu P_R \Psi_{\pm R} - i\overline{\Psi}_{\pm L} D_{\mp} P_R \Psi_{\pm R} + i\overline{\Psi}_{\pm R} D_{\pm} P_L \Psi_{\pm L}), \tag{A.21}$$

where D_μ is the normal covariant derivative, $\partial_\mu - ig_6 A_\mu$ for the case of Abelian gauge fields and $\partial_\mu - ig_6 A^a_\mu T_a$ for the case of non-Abelian gauge fields, $D_\pm = D_4 - iD_5 = (\partial_4 - ig_6 A_4) - i(\partial_5 - ig_6 A_5)$, and $P_{L,R} = 1/2(1 \mp \gamma^5)$.

A.2.3 $\mathcal{L}_{Higgs}$

The Higgs interaction is a direct copy from the standard model, including the kinetic terms, the gauge interactions and the quartic Higgs potential, except that the SM 4D field is replaced by the 6D Higgs field Φ [33] which is a $SU(2)$ doublet. The Higgs Lagrangian introduces spontaneous symmetry breaking by the 6D VEV $v_6 = v_4/L$:

$$\mathcal{L}_\Phi = |D_\alpha \Phi|^2 - \frac{\lambda_6}{2}\left(\Phi^\dagger \Phi - \frac{1}{2} v_6^2\right)^2, \tag{A.22}$$

where 6D gauge and quartic couplings are related to the 4D ones by $g_6 = g_4 L$ and $\lambda_6 = \lambda_4 L^2$ and Φ are the scalar KK-terms described in eq (A.7). After KK-decomposition and intergration over the two extra dimensions, we obtain not only the SM Higgs interaction and its KK excitations, but interactions of types H-H-A_H-A_H and H-A_H-A_H (after spontaneous symmetry breaking) as well.

The KK Higgs (i,j) mode acquires the following mass

$$M_h^{(j,k)} = \sqrt{M_{j,k}^2 + \lambda_4 v_4^2}\ , \tag{A.23}$$

A.2.4 $\mathcal{L}_{Violating}$

The KK-number (N_{KK}) violating interactions arise from operators localized on one of the three conical singularities of the chiral square topology. As described in the section on KK-Parity, N_{KK} violating interactions mostly involve single $(1,1)$ mode fields and two Standard Model fields (there are a few 4-particle interactions resulting from 5-dimensional operators). All of the equations referenced in this section are given in [32] and [54] but reiterated here for a quick central reference. The operator describing the interactions between two standard model quarks and a level $(1,1)$ KK-gluon is ,

$$g_s C_{1,1}^{qG} (\overline{q}\gamma^\mu T^a q) G_\mu^{(1,1)a}\ , \tag{A.24}$$

where

$$C_{1,1}^{qG} = \xi_{q_{L,R}}^G \frac{g_s^2 N_c}{16\pi^2} ln\left(\frac{M_s^2}{M_{(1,1)}^2}\right), \tag{A.25}$$

$$\xi_{q_L}^G = 1 - \frac{1}{2g_s^2}\left(\frac{1}{3}\lambda_{q_L}^2 + \frac{3}{2}g_2^2 + \frac{1}{18}g_1^2\right), \tag{A.26}$$

$$\xi_{q_R}^G = 1 - \frac{1}{g_s^2}\left(\frac{1}{3}\lambda_{q_R}^2 + \frac{y_{q_R}^2}{4}g_1^2\right). \tag{A.27}$$

It should be noticed that eq (A.24) is actually a sum of the L and R handed contributions.

In the EW sector, Standard Model fermions interact with level $(1,1)$ EW vector

fields via several similar operators. Interactions with the physical $W_\mu^{(1,1)i}$ fields are:

$$g_2 C_{1,1}^{fW} (\overline{f_L} \gamma^\mu T_2^i f_L) W_\mu^{(1,1)i} \ , \tag{A.28}$$

where T_2^i are the $SU(2)_W$ generators and,

$$C_{1,1}^{qW} = \xi_q^W \frac{g_s^2 N_c}{16\pi^2} ln \left(\frac{M_s^2}{M_{(1,1)}^2} \right), \tag{A.29}$$

$$C_{1,1}^{lW} = 2 g_2^2 \xi_l^W \frac{1}{16\pi^2} ln \left(\frac{M_s^2}{M_{(1,1)}^2} \right), \tag{A.30}$$

where ξ_q^W and ξ_l^W are the coefficients corresponding to left-handed fermion doublets. These are given by,

$$\xi_q^W = -\frac{4}{3} - \frac{\lambda_q^2}{6 g_s^2} + \frac{1}{36 g_s^2} \left(11 g_2^2 - g_1^2 \right), \tag{A.31}$$

$$\xi_l^W = \frac{11}{24} - \frac{3 g_1^2}{8 g_2^2}. \tag{A.32}$$

Similarly, interactions of Standard Model fermions with the $B_\mu^{(1,1)}$ fields are:

$$g_1 \frac{y_f}{2} C_{1,1}^{fB} (\overline{f} \gamma^\mu f) B_\mu^{(1,1)} \ , \tag{A.33}$$

where,

$$C_{1,1}^{q_{L,R}B} = \xi_{q_{L,R}}^B \frac{g_s^2 N_c}{16\pi^2} ln \left(\frac{M_s^2}{M_{(1,1)}^2} \right), \tag{A.34}$$

$$C_{1,1}^{lB} = 2 g_2^2 \xi_l^B \frac{1}{16\pi^2} ln \left(\frac{M_s^2}{M_{(1,1)}^2} \right), \tag{A.35}$$

$$C_{1,1}^{eB} = g_1^2 \xi_e^B \frac{1}{16\pi^2} ln \left(\frac{M_s^2}{M_{(1,1)}^2} \right), \tag{A.36}$$

where $\xi_{q_L}^B$ and ξ_l^B are the coefficients corresponding to left-handed fermion doublets,

while $\xi^B_{q_R}$ and ξ^B_e correspond to the right handed singlet fields. These are given by,

$$\xi^B_{q_L} = -\frac{4}{3} - \frac{1}{2g_s^2}\left(\frac{1}{3}\lambda^2_{q_L} + \frac{3}{2}g_2^2 + \frac{83}{18}g_1^2\right), \tag{A.37}$$

$$\xi^B_{q_R} = -\frac{4}{3} - \frac{1}{g_s^2}\left[\frac{1}{3}\lambda^2_{q_R} + \left(\frac{41}{18} + \frac{y^2_{q_R}}{4}\right)g_1^2\right], \tag{A.38}$$

$$\xi^B_l = -\frac{9}{8} - \frac{91g_1^2}{24g_2^2}, \tag{A.39}$$

$$\xi^B_e = -\frac{59}{6}. \tag{A.40}$$

The level $(1,1)$ scalar adjoints, $G_H^{(1,1)a}, W_H^{(1,1)i} and B_H^{(1,1)}$, interact with two Standard Model quarks via the following set of operators:

$$g_s\frac{\tilde{C}^{q_{L,R}}_{1,1}}{M_{(1,1)}}(\overline{q}\gamma^\mu T^a q)D_\mu G_H^{(1,1)a}, \tag{A.41}$$

$$g_2\frac{\tilde{C}^{q_L}_{1,1}}{M_{(1,1)}}(\overline{q}\gamma^\mu T_2^i q)D_\mu W_H^{(1,1)i}, \tag{A.42}$$

$$g_1\frac{y_{q_{L,R}}}{2}\frac{\tilde{C}^{q_{L,R}}_{1,1}}{M_{(1,1)}}(\overline{q}\gamma^\mu q)D_\mu B_H^{(1,1)}. \tag{A.43}$$

where D_μ is the covarient derivative $\partial_\mu - ig_sT^aG^a_\mu$ (for the colored interaction, for example) with T^a being the respective group generator for SU(3), SU(2) and U(1).

$$\tilde{C}^{q_{L,R}}_{1,1} = \tilde{\xi}_{q_{L,R}}\frac{g_s^2N_c}{16\pi^2}ln\left(\frac{M_s^2}{M^2_{(1,1)}}\right), \tag{A.44}$$

$$\tilde{\xi}_{q_L} = \frac{4}{3} + \frac{1}{4g_s^2}\left(3g_2^2 + g_1^2y^2_{q_L}\right), \tag{A.45}$$

$$\tilde{\xi}_{q_R} = \frac{4}{3} + \frac{1}{4g_s^2}g_1^2y^2_{q_R}. \tag{A.46}$$

Finally, the level $(1,1)$ scalar adjoints interact with two Standard Model leptons via the

following set of operators:

$$g_2 \frac{\tilde{C}^{l_L}_{1,1}}{M_{(1,1)}} (\bar{l}\gamma^\mu T_2^i l) D_\mu W_H^{(1,1)i}, \tag{A.47}$$

$$g_1 \frac{y_{l_{L,R}}}{2} \frac{\tilde{C}^{l_{L,R}}_{1,1}}{M_{(1,1)}} (\bar{l}\gamma^\mu l) D_\mu B_H^{(1,1)}. \tag{A.48}$$

where,

$$\tilde{C}^{l_{L,R}}_{1,1} = \tilde{\xi}_{l_{L,R}} \frac{g_s^2 N_c}{16\pi^2} ln\left(\frac{M_s^2}{M^2_{(1,1)}}\right), \tag{A.49}$$

$$\tilde{\xi}_{l_L} = \frac{1}{4g_s^2}\left(3g_2^2 + g_1^2 y^2_{l_L}\right), \tag{A.50}$$

$$\tilde{\xi}_{l_R} = \frac{1}{4g_s^2} g_1^2 y^2_{l_R}. \tag{A.51}$$

A.3 Derivation of the $G_H^{(1,1)}$ width

The Feynman rule for the $G_H^{(1,1)} q\bar{q}$ vertex is,

$$-i\frac{g_s}{M_{11}} \bar{u}(p_1) \not{p} (C_R P_R + C_L P_L) v(p_2) \tag{A.52}$$

where $C_{R,L}$ are dimensionless constants, $P_{R,L}$ are the left and right handed projection operators, and M_{11} is the $(1,1)$ Kaluza-Klein mass.

A.3.1 Matrix element

In order to calculate the width, we need to first calculate the matrix element squared for this interaction. Since the vertex caries a color factor, we need to average over the initial colors and sum over the final ones.

$$\frac{1}{8}\sum_{a,i,j} T^a_{ij} T^a_{ji} = \frac{1}{8} Tr\left[T^a T_a\right] = \frac{1}{8}\cdot 8 \cdot \frac{1}{2} = \frac{1}{2} \tag{A.53}$$

Therefore, the matrix element squared is,

$$\frac{1}{2}\sum_{spins}|M_{fi}|^2 = \frac{1}{2}\left(\frac{g_s}{M_{11}}\right)^2 \sum_{spins} Tr\left(\left[\bar{u}(p_1)\not{p}(C_RP_R + C_LP_L)v(p_2)\right]\cdot\right.$$

$$\left.\left[\bar{v}(p_2)(C_RP_L + C_LP_R)\not{p}u(p_1)\right]\right)$$

$$= \frac{1}{2}\left(\frac{g_s}{M_{11}}\right)^2 \sum_{spins} Tr\left(\left[u(p_1)\bar{u}(p_1)\not{p}(C_RP_R + C_LP_L)\right]\cdot\right.$$

$$\left.\left[v(p_2)\bar{v}(p_2)(C_RP_L + C_LP_R)\not{p}\right]\right)$$

$$= \frac{1}{2}\left(\frac{g_s}{M_{11}}\right)^2 Tr\left[(\not{p}_1 + m_1)\not{p}(C_RP_L + C_LP_R)(\not{p}_2 - m_2)\ (C_RP_L + C_LP_R)\not{p}\right]. \quad \text{(A.54)}$$

Now, let us define,

$$P_{RL} = C_RP_R + C_LP_L \quad \text{(A.55)}$$

$$P_{LR} = C_RP_L + C_LP_R \quad \text{(A.56)}$$

to make the expressions simpler once expanded. The result being,

$$\frac{1}{2}\left(\frac{g_s}{M_{11}}\right)^2 Tr\left[\not{p}_1\not{p}P_{RL}\not{p}_2P_{LR}\not{p} - m_2\not{p}_1\not{p}P_{RL}P_{LR}\not{p} + m_1\not{p}P_{RL}\not{p}_2P_{LR}\not{p} - m_1m_2\not{p}P_{RL}P_{LR}\not{p}\right] \quad \text{(A.57)}$$

The trace of the second and third terms in the above expression can be shown to be equivalently zero since they contain an odd number of gamma matrices, regardless of the right or left handed projection operators. The $\not{p}$ in the 4th term can be commuted to the right due to trace rules (e.g. $Tr[AB] = Tr[BA]$). Since it can be shown that $\gamma^\mu P_R = P_L\gamma^\mu$, the first P_{RL} in the first term can be commuted to the right, changing it to P_{LR}. The resulting expression is,

$$\frac{1}{2}\left(\frac{g_s}{M_{11}}\right)^2 Tr\left[\not{p}_1\not{p}\not{p}_2P_{LR}^2\not{p} - m_1m_2\not{p}\not{p}P_{RL}P_{LR}\right] \quad \text{(A.58)}$$

Looking now at $P_{LR}P_{RL}$ and P_{LR}^2, remembering that $P_R P_L = P_L P_R = 0$

$$P_{LR}P_{RL} = C_R C_L (P_L^2 + P_R^2) = C_R C_L (P_L + P_R) = C_R C_L \tag{A.59}$$

$$P_{LR}^2 = C_L^2 P_R^2 + C_R^2 P_L^2 = C_L^2 P_R + C_R^2 P_L \tag{A.60}$$

Substituting these into eq. A.58 and noticing that the γ_5 parts of the second part won't contribute to the trace,

$$\frac{1}{2}\sum_{spins}|M_{fi}|^2 = \frac{1}{2}\left(\frac{g_s}{M_{11}}\right)^2 Tr\left[(C_R^2/2 + C_L^2/2)\not{p}_1\not{p}\not{p}_2\not{p} - m_1 m_2 C_R C_L \not{p}\not{p}\right] \tag{A.61}$$

Using the standard trace rules, this becomes,

$$\frac{1}{2}\left(\frac{g_s}{M_{11}}\right)^2 \left[4(C_R^2/2 + C_L^2/2)\left((p_1\cdot p)(p_2\cdot p) - (p_1\cdot p_2)(p\cdot p) + (p_1\cdot p)(p_2\cdot p)\right) - 4m_1 m_2 M_{G_H^{11}}^2 C_R C_L\right] \tag{A.62}$$

With $m_1 = m_2 = m_q$ as well as the following kinematic quantities,

$$p\cdot p = M_{G_H^{11}}^2 \tag{A.63}$$

$$p_1\cdot p = p_2\cdot p = \frac{M_{G_H^{11}}^2}{2} \tag{A.64}$$

$$p_1\cdot p_2 = \frac{M_{G_H^{11}}^2}{2} - m_q^2, \tag{A.65}$$

eq. A.62 reduces, after some simple algebra, to,

$$\frac{1}{2}\sum_{spins}|M_{fi}|^2 = \left(\frac{g_s}{M_{11}}\right)^2 M_{G_H^{11}}^2 m_q^2 (C_L - C_R)^2 . \tag{A.66}$$

A.3.2 G_H^{11} Width

Using the following equation [reference] to calculate the width, or rate of a decay for a particle of mass M at rest (in our case, the G_H^{11}),

$$\Gamma = \left(\frac{1}{2M}\right)\left(\frac{1}{4\pi}\right)^2 \frac{p_q}{M} \int \frac{1}{2} \sum_{spins} |M_{fi}|^2 \, d\Omega, \tag{A.67}$$

where p_q is the magnitude of the momentum vector of one of the decayed quarks and M is the mass of the G_H^{11}, we find that,

$$\begin{aligned}
\Gamma(G_H^{11} \to q\bar{q}) =& \left(\frac{g_s}{M_{11}}\right)^2 \left(\frac{1}{2M_{G_H^{11}}}\right)\left(\frac{1}{4\pi}\right)^2 M_{G_H^{11}}^2 m_q^2 \left(C_L - C_R\right)^2 \frac{\sqrt{M_{G_H^{11}}^2/4 - m_q^2}}{M_{G_H^{11}}} \int d\Omega \\
=& \frac{1}{2}\left(\frac{g_s}{M_{11}}\right)^2 \left(\frac{1}{4\pi}\right)^2 m_q^2 M_{G_H^{11}} \left(C_L - C_R\right)^2 \sqrt{\frac{1}{4} - \frac{m_q^2}{M_{G_H^{11}}^2}} \int d\Omega \\
=& \frac{1}{2}\left(\frac{g_s}{M_{11}}\right)^2 \left(\frac{1}{4\pi}\right) m_q^2 M_{G_H^{11}} \left(C_L - C_R\right)^2 \sqrt{\frac{1}{4} - \frac{m_q^2}{M_{G_H^{11}}^2}}
\end{aligned} \tag{A.68}$$

Now, we can put in the constants as defined in [reference]. Defining,

$$C_R = \xi_{q_R} C_{11} \tag{A.69}$$

$$C_L = \xi_{q_L} C_{11} \tag{A.70}$$

where,

$$\xi_{q_L} = \frac{4}{3} + \frac{1}{4g_s^2}\left(3g_2^2 + g_1^2 y_{q_L}^2\right), \tag{A.71}$$

$$\xi_{q_R} = \frac{4}{3} + \frac{1}{4g_s^2} g_1^2 y_{q_R}^2. \tag{A.72}$$

$$C_{11} = \frac{N_c g_s^2}{16\pi^2} Log\left(\frac{M_s^2}{M_{11}^2}\right). \tag{A.73}$$

The width is,

$$\Gamma(G_H^{11} \to q\bar{q}) = \frac{1}{2}\left(\frac{g_s}{M_{11}}\right)^2 \left(\frac{1}{4\pi}\right) m_q^2 M_{G_H^{11}} C_{11}^2 \left(\xi_{q_L} - \xi_{q_R}\right)^2 \sqrt{\frac{1}{4} - \frac{m_q^2}{M_{G_H^{11}}^2}}. \qquad \text{(A.74)}$$

It should be relatively clear from this result that the width is highly dependent on the quark mass, indicating that the G_H^{11} decays primarily to top quark pairs. In fact, the branching fraction to $t\bar{t}$ is more than 99% and increases as $1/R$ increases.